DELFT UNIVERSITY OF TECHNOLOGY

MASTER THESIS

Uncertainty and propagation analysis on DIMITRI

Author:
Srosh SHOAIE

Student id:
4177436

University supervisor:
Daphne STAM

ESA/ESTEC supervisor:
Marc BOUVET

A thesis research
for a Master of Science degree

Spaceflight Track - Space Exploration Profile
-
Aerospace Engineering Master

August 10, 2017

"There is no elevator to success, you have to take the stairs . . . "

Unknown

" . . . unless you're a space engineer, in which case you take the rocket and would reach far higher than ever possible with stairs"

A dreamer

Acknowledgements

First and foremost I want to thank Marc Bouvet, my company supervisor, whose patience and guidance has helped me throughout my internship and the writing of this thesis. In addition, I want to thank Daphne Stam for guiding me through my thesis and asking me many questions, which forced me to critically review all assumptions and explanations that I had regarding this subject.

I also want to thank the following friends and family for their feedback; Abbas, Tom, Stephan, Farhad and Erfan. In particular I want to thank Vandana for her assistance in generating the results published in this thesis.

For the template of this thesis I want to thank Sunil Patel, you have made it very easy for me to get started (S. Patel, 2016).

Contents

To the beneficial advancement of all inhabitants of planet Earth.

In particular, as a fellow scientist, I wish to partake in accepting the responsibility that Richard P. Feynman so correctly stated in 1955;

"It is our responsibility as scientists, knowing the great progress and great value of a satisfactory philosophy of ignorance, the great progress that is the fruit of freedom of thought, to proclaim the value of this freedom, to teach how doubt is not to be feared but welcomed and discussed, and to demand this freedom as our duty to all coming generations."∼ The value of science

Summary

Within the remote sensing community, radiometric inter-comparison between optical instruments is desired to obtain long-term trends that surpass the operational lifetime of satellite missions. The Database for Imaging Multi-spectral Instruments and Tools for Radiometric Inter-comparison (DIMITRI) is a tool that has been developed for this very purpose. One of the inter-comparison methodologies that is implemented in this tool is the Rayleigh calibration methodology, through which it is possible to perform in-flight vicarious calibration for optical instruments. The Rayleigh calibration methodology uses Rayleigh scattering over *a priori* determined oceanic locations that have been identified to have suitable and stable radiometric characteristics. The Rayleigh calibration methodology is able to generate a simulated top-of-atmosphere reflectance. DIMITRI includes a database of top-of-atmosphere reflectance observations and the ratio of this quantity to the simulated top-of-atmosphere reflectance is defined to be a calibration coefficient, through which the performance of the operational satellite can be monitored.

The objective of this thesis was to initially break up the total uncertainty associated with the calibration coefficient, caused by uncertainties associated with the input variables, and to classify it as a combined factor of random and systematic uncertainty components. However, throughout this thesis, it became clear that not only is this classification ambiguous and sometimes misleading, but it required much more research and time than initially expected. This research contains a full description of the reflectance model that is incorporated in the Rayleigh calibration methodology, outlining all steps, assumptions and methods used to obtain the input variables and the calibration coefficient with a particular certainty. It turns out that the uncertainties associated with the input variables are both random and systematic in nature, and these propagate through the Rayleigh calibration methodology to influence the quality of the calibration coefficient. The propagation of uncertainties have been analyzed using a simulation-based Monte Carlo method and a power-series based Taylor expansion method. The Taylor-series method would provide results within one evaluation, as compared with the Monte Carlo simulations which requires a large output sample, and thus a Taylor-series method was preferred. However, due to the mathematical complexity of the reflectance model it became clear that simplifications are required before such an analysis could be performed.

Using a data analysis to validate the simplified version of the reflectance model through a Monte Carlo simulation, it was shown that the calibration coefficients obtained from the simplified version agree to within a 5% of those obtained with the unmodified version. Another aspect of the simplified model that is verified is the uncertainty component associated with the calibration coefficient. With respect to the unmodified model, these uncertainty components are only allowed to deviate 1%. Using a fourth-order Taylor-series expansion method uncertainties associated with the input variables have been propagated through the reflectance model. However, the severe nonlinearity of the underlying model, even after being simplified, prevents obtaining sufficiently accurate uncertainty components. An alternative approach, however, has proven to be successful. It appears that the calibration coefficients exhibit a semi-linear dependence on the input variables. By assuming the output distribution is uniform, the uncertainty components have been propagated as if the reflectance

model is linear and the results are satisfactory.

So far, this research has achieved to establish the sensitivity of the Rayleigh calibration methodology with respect to its input variables. It has also described the acquisition and measuring / modelling procedures of the input variables and the calibration coefficient. Unfortunately, this research did not achieve a classification of uncertainties, or, a quantification for that matter. Future research could use this study to quantify uncertainties for those sources that have been identified. They can be combined to obtain a total uncertainty component associated with the calibration coefficients that can be attributed to uncertainties in the input variables and or the measurement / modelling procedures in the Rayleigh calibration methodology.

Introduction

Within the Earth observation / remote sensing community it is desired to observe long-term trends of Earth processes. The operational lifetime of a satellite is often too short and thus successive missions are developed and operated to ensure continuity of monitoring capabilities. To this end, data obtained from different missions must be compared to establish trends of these processes.

Within this thesis an uncertainty and propagation analysis is performed on one such tool that provides a platform for the radiometric inter-comparison of satellite observations. This tool is called DIMITRI and is developed under supervision of Marc Bouvet (ESA/ESTEC). The output of this inter-comparison is accompanied with an associated uncertainty that is described by Hagolle et al. (1999). Taking into account the influence of Ozone, wind speed, surface pressure, aerosols and phytoplankton, a maximum uncertainty of 4% is quantified. In 2015 I had the privilege to work on the augmentation of DIMITRI with OLCI and SLSTR observations during an internship. At the time, Marc indicated that he was interested in updating the output to not only include the uncertainty, but to also differentiate between random and systematic uncertainties. With this in mind, uncertainty and propagation analysis have been performed on one of the inter-comparison methodologies that is implemented in DIMITRI.

In chapter 1 the context of this a thesis is outlined, explaining why this research is of interest. Then, in order to investigate the distinction between systematic and random uncertainties, the physical principles on which the radiometric inter-comparison tool are based are thoroughly addressed in chapter 2. It should be noted that in order to identify (the systematic) uncertainties in a measurement or modelling process, all assumptions and simplifications in these processes must be tracked and their impact on the results quantified. This requires a tedious but necessary study of the available literature in order to identify potential sources of uncertainties. The tool itself is shortly introduced as well in chapter 3. The basics of uncertainty theory are described in chapter 4 after which an uncertainty analysis and propagation analysis are performed in chapter 5 to increase the level of insight in the uncertainties associated with the generated results and also to better research DIMITRI.

Any findings that are presented here can be used for future versions of DIMITRI and possibly, to update the tool to dispense more information regarding the accuracy of the inter-comparison output and regarding the propagation of uncertainties.

Chapter 1

Research context

In this chapter an attempt is made to define the context in which this thesis is conducted. *Why* such a thesis is even interesting and to *whom* it is interesting is outlined in section 1.1 and section 1.2. Then, the *how* is addressed briefly in section 1.3 and section 1.4, bringing the reader closer to the purpose of this thesis which is addressed in section 1.5.

1.1 Earth observation

In the field of Earth observation, the scientific community monitors natural processes that occur on planet Earth. We as inhabitants of this planet are highly dependent on these processes because they influence the weather (e.g. rainfall or temperature), the climate (e.g. sea surface height or sea surface temperatures), our agriculture (e.g. crops or fresh water) and our safety (e.g. floods or droughts). There is no doubt about the relevance of monitoring these processes in relation to our continued stay on planet Earth.

In order to monitor natural processes scientists use instruments that gather information from four areas; from space which surrounds the planet, the Earth's atmosphere, its surface (both on land and water) and finally from beneath the surface. Scientists and engineers have worked together over the years to place instruments in these places. Note that space is particularly interesting because of its unique vantage point. Information can be gathered from the direct vicinity of the instrument or it can be gathered remotely. In the former case we speak of *in-situ* instruments and some examples are a thermometer, pressure gauges or hygrometer. These measure the temperature, pressure and humidity in the environment 'close' to the instrument. In the latter case we speak of *remote sensing* instruments, such as a radiometer, and these measure, e.g. the Sun's intensity or reflected/emitted radiation from the Earth's atmosphere or surface.

1.2 Calibration

An important question that comes to mind is how the scientific community knows that a particular instrument operates correctly. This guarantee comes from *calibration*, which is the process of establishing to what extend the instrument measures what it is designed to measure. By using a 'known' source with known characteristics, and measuring that by an instrument, the characteristics of that particular instrument can be established and a measure of the performance is obtained. This act of *verification* of an instruments performance is indispensable to scientific research and forms the foundation upon which the scientific community bases conclusions and recommendations.

A noteworthy feature for remote sensing instruments in space is that there are more than one stages of calibration. Before the instrument is launched into space a pre-flight calibration is performed, where under simulated 'space-like' environmental conditions the instrument is

tested rigorously. However, the transportation from the test location to its operational environment in space is 'bumpy' to say the least. In addition, a launch and orbit ingestion procedure can alter the instrument in such a way that previous performance characterizations are no longer accurate. Hence, an *in-flight / on-board* calibration procedure is commenced during the commissioning phase of the satellite, which can last a few months. During this phase the instrument is prepared and tested within its operational environment. This allows the scientific community to conclusively characterize the instrument's performance after launch and ingestion, after outgassing of trapped air from within the instrument, and under the presence of cosmic radiation.

Another reason to maintain track of the performance is to identify degradation of the instrument. It comes as no surprise that the instrument performance is adversely affected in the hazardous space environment and thus, to be able to rely on the information provided by an instrument, in-flight calibration is crucial.

So how is in-flight calibration established? In case of a radiometer, *black-body* targets can be used which the instrument will look at to give an estimate on their emitted black body temperature. In case of a spectrometer, highly reflective surfaces such as spectralon *diffuse panels* are used to simulate the reflectance of light. These on board calibration equipment have known characteristics and are used to track how well the instruments operate. However, the remote sensing instrument is not the only equipment that is subject to degradation, the in-flight calibration equipment is too. Therefore, there is an additional type of calibration which is referred to as *vicarious calibration*. Here artificial/natural sites on Earth with stable and well known radiometric characteristics can be used for the purpose of in-flight calibration of instruments and also, their in-flight calibration equipment. In some cases vicarious calibration substitutes in-flight calibration equipment entirely when it is determined that such equipment cannot provide the necessary levels of accuracy. This was the case for the POLDER instrument on board NASDA's ADEOS polar orbiting satellite. Implementation of in-flight calibration equipment can be expensive and difficult and all the effort otherwise required can be invested in the enhancement of calibration methods over natural sites. In other cases, such as with the OLCI sensor on board the Sentinel-3 satellite, vicarious calibration is complementary to the in-flight calibration equipment.

1.3 Atmospheric modelling

Inherent to the *monitoring* of natural processes on Earth is the fact that it is only possible to observe processes that are happening at the *moment* of observation. The scientific community is not only interested in monitoring these processes *ad hoc* but are also interested in being able to make predictions. This requires computer generated models where natural processes under observation are described analytically and/or numerically to simulate natural processes. An example are atmospheric models which simulate the propagation of light waves through the atmosphere and oceanic layer. Interestingly, once it has been established that such a model is accurate to within a certain degree, it becomes possible to use it for monitoring the performance of remote sensing instruments.

The propagation of light through a medium is described by *radiative transfer* equations, which can tell us how much light will be reflected back by the atmosphere/surface to be observed by the instrument on board the spacecraft.

So, how do we model the Earth's atmosphere? The atmosphere is a relatively thin layer that surrounds the entire planet and it contains molecules, ions and aerosols. Aerosols are particles that are much larger than molecules such as sea salt, soot, dust or sand. Out of all

the elements that are included in the atmosphere only a few are selected to make the atmospheric model manageable. For each element, the concentration per unit volume/column is given, along with its cross section and shape. Furthermore, information about its scattering, absorption and reflection properties must also be included. The atmosphere itself can be assumed to be a single flat layer, the so-called *plane-parallel assumption*, or to be a sphere around the Earth. Then, using all this information, radiative transfer equations can simulate how light waves propagate through the atmosphere.

1.4 DIMITRI

Within the remote sensing scientific community, a need for sensor inter-comparison has led to the development of the Database for Imaging Multi-spectral Instruments and Tools for Radiometric Inter-comparison (DIMITRI). Within this tool a database of reflectances is available that has been gathered by various instruments that operate in the optical wavebands. Sensor inter-comparison is useful because long-term trends can be monitored that outlast the natural lifetime of a single spacecraft. In addition, the collective set of sensor data can be used as a reference against which new observations are compared.

One performance monitoring capability that this tool has is called the *Rayleigh calibration methodology*, which uses Rayleigh scattering over the open ocean for the purpose of absolute vicarious calibration of remote sensing observations. The Rayleigh calibration methodology includes a *reflectance model* which simulates a value for the reflectance at the top of the atmosphere. This requires information regarding the actual viewing conditions and also information regarding the meteorological conditions. Now we have a simulated reflectance, but how does this help us to monitor the performance of the sensor? To clarify, the simulated reflectance takes the viewing condition of the spacecraft, meteorological conditions and the date of operation into account. For those same conditions actual *observed* reflectances are available. Then, the Rayleigh calibration methodology reads the observed reflectances and computes a coefficient as the ratio of the observed to simulated reflectance. This coefficient is referred to as the *calibration coefficient* and allows the remote sensing community to monitor the performance degradation and to compare its performance to its predecessor(s). Such as comparing the performance of OLCI and SLSTR on board the recently launched Sentinel-3A satellite with their predecessors MERIS and AATSR on board ENVISAT.

1.5 Objective

All the aforementioned was presented to explain and justify this thesis research. The objective, briefly mentioned in the introduction, is to analyze how uncertainties associated with the input variables propagate through the Rayleigh calibration methodologies, and what their influence will be on the resulting calibration coefficient. Particularly interesting is researching how a distinction can be made between two types of uncertainties; *Type A* and *Type B*, often referred to as *random* and *systematic*.

Chapter 2

Reflectance model

In this chapter the reflectance model that is incorporated in the Rayleigh calibration methodology is thoroughly described. However, before diving into the physics of the reflectance model, the principle on which the Rayleigh calibration methodology is based, called the two-band method, is addressed in section 2.1 to give the reader a clear handle on why the fundamentals of wave propagation through the atmosphere (section 2.2) and the ocean (section 2.3) are explained.

2.1 The *two-band* method

In the introduction it was explained that DIMITRI is a tool which can be used to monitor the performance of optical instruments that operate on satellites. DIMITRI is equipped with a Rayleigh Calibration Methodology (RCM), which is an algorithm that observes Rayleigh scattering over the open ocean for the purpose of vicarious calibration. The reason why Rayleigh scattering is used is because, under certain conditions, it amounts to approximately 90% of the observed signal (Fougnie et al., 2002) and becomes very predictable (VERMOTE et al., 1992). The conditions are that the ocean surface is carefully selected based on radiometric stability, where low chlorophyll concentrations are present, low wind speeds and with little to no presence of clouds or large aerosol loading.

DIMITRI contains a database of radiometric data which are the observed top-of-atmosphere reflectance provided by several optical instruments. These are denoted by ρ_{obs}^{TOA}. The database also includes geometrical and meteorological data corresponding with the sensor observation conditions. Under the same viewing and atmospheric conditions, the RCM is able to simulate top-of-atmosphere reflectances and these are denoted by ρ_{sim}^{TOA}. The resulting simulated reflectances are viewed as a reference for ρ_{obs}^{TOA} because ρ_{sim}^{TOA} are verified and validated against in-situ data. In DIMITRI, a ratio of ρ_{obs}^{TOA} to ρ_{sim}^{TOA} is calculated and this is called the calibration coefficient, C, which is the parameter that can be 'tracked' throughout the sensor's lifetime to monitor its performance.

So how are ρ_{sim}^{TOA} simulated in the RCM? ρ_{sim}^{TOA} consists of several other types of reflectances; which are reflectance due to Rayleigh scattering (ρ_R), reflectance due to aerosol scattering (ρ_a), water-leaving reflectance (ρ_w), reflectance due to Sunglint (fresnel reflection on the water surface) (ρ_g) and reflectance due to foam on the water surface (ρ_f). All necessary terms will be explained in due time but for the moment the focus lies on addressing the two-band method. To that end, VERMOTE et al. (1992) explain that estimates for ρ_a, ρ_g and ρ_f from the near-infrared (NIR) bands are easier to attain than from shorter λ. At longer λ the contribution of Rayleigh scattering to the ρ^{TOA} signal decreases. In fact, the RCM is only valid for $\lambda < 700\,nm$ because the Rayleigh scattering becomes otherwise too small (Barker et al., 2014). VERMOTE et al., 1992 have determined that for $\lambda = 0.78 - 0.89\,nm$, ρ_R is several orders of magnitude smaller than at $\lambda = 0.43 - 0.47\,nm$. Then, the signal that is obtained at longer λ is mostly due to ρ_a and partly due to ρ_f. ρ_w is negligible and ρ_g as well, except for a particular *Sunglint* angle. However, the angle under which Sunglint is observed is determined and reflectance values for this angle are not included, allowing ρ_g to be ignored.

It was mentioned that for long λ ρ_R decreases. This does not imply that ρ_a and ρ_f can be determined more accurately for very long λ. The purpose of retrieving information of ρ_a and ρ_f from long λ is to eventually extrapolate information to short λ. In order to avoid extrapolation errors, it is better to use a NIR band that is as close as possible to the visible bands. VERMOTE et al., 1992 performed this procedure for the VEGETATION instrument and the waveband that was most suitable for this role was at $\lambda = 865\,nm$, even though a band existed at $\lambda = 1580 - 1750\,nm$. Out of ρ_a and ρ_f, the former is approximately 33% - 800% larger, depending on the Sun zenith angle θ_s and the viewing zenith angle θ_v (see Figure 2.1[1]), which means that ρ_f can be ignored. This means that the reflectance that is observed at $\lambda = 865\,nm$ can be viewed as ρ_a^{865} and this can be propagated to short (visible) bands. The usage of the NIR band for extraction of the aerosol content constitutes the name *two-band* method.

At this point the appropriate amount of introduction is given and we can continue with addressing the definition and physical principles on which the reflectance model is based. Mathematically, the model is defined as follows (Barker et al., 2014);

$$\rho_{sim}^{TOA} = t_{gas}\ (\rho_{path} + t_d\, t_u\, \rho_w + T_d\, T_u\, \rho_g) \tag{2.1}$$

TABLE 2.1: *Reflectance model for the Rayleigh calibration methodology in DIMITRI - variable definition*

Variable	Definition
ρ_{sim}^{TOA}	The simulated top-of-atmosphere reflectance.
t_{gas}	Transmittance, both up and down, due to H_2O, O_2 and O_3 absorption.
ρ_{path}	Atmospheric path reflectance due to molecules, aerosols, and multiple interactions between these.
t_d & t_u	Total transmittance (direct and diffuse) due to molecules and aerosols, both down and up.
ρ_w	Water-leaving reflectance.
T_d & T_u	Transmittance (direct) both down and up.
ρ_g	Sunglint reflectance at sea level.

The variables (see Table 2.1) can be divided in two sections, where the first one addresses wave propagation through the atmosphere and the second addresses wave propagation through the ocean.

2.2 Atmospheric wave propagation

In order to thoroughly understand the reflectance model very basic physical concepts are addressed in subsection 2.3.1. Afterwards, aerosol models are introduced in subsection 2.2.2. These are models that attempt to resemble the scattering of light in the atmosphere for a given molecular and aerosol constituents. Finally, two physical quantities remain to be explained and these are ρ_{path} and the t, and they are discussed in subsection 2.2.3 and subsection 2.2.4 respectively.

[1]Note that this drawing is made using the online drawing tool available on https://www.draw.io/

FIGURE 2.1: *Arbitrary viewing geometry with the Sun zenith angle (sza), θ_s, the viewing zenith angle (vza), θ_v and finally the relative azimuth angle (raa), $\Delta\phi$.*

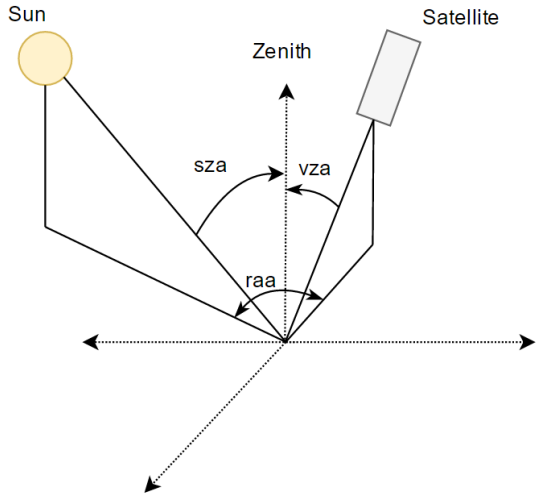

FIGURE 2.2: *Energy transition levels of a Hydrogen atom and the process of absorption and emission between these levels.*

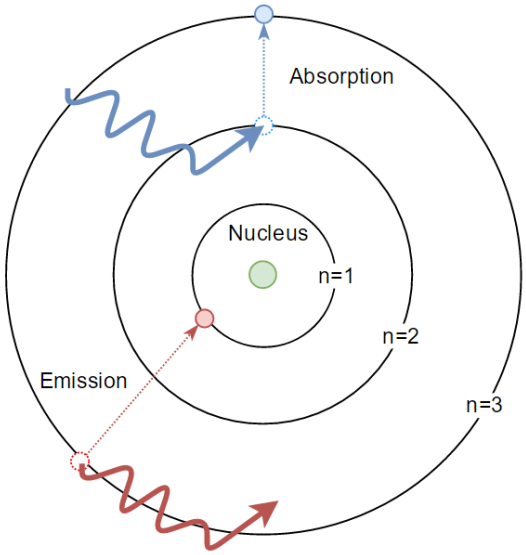

2.2.1 Fundamentals

Two forms of radiative transfer can be explained by the energy levels of electrons in an atom[2]. Electrons have a unique set of energy *levels* or *states* that they can be in, depending on the atom. These levels, for the sake of illustration, correspond with concentric circles with a different radii about the nucleus (see Figure 2.2). The lowest energy level lies the closest to the nucleus and is referred to as the *ground level* (indicated by $n = 1$). The further the level is removed from the nucleus the higher the energy level is and the maximum energy level is the level at which the electron completely escapes its bonds with the nucleus and the atom becomes *ionized*.

If illuminated by a photon that has an energy that corresponds with the gap between any of these energy states, an electron can jump from its ground state to the next energy state, or any other of its higher states, depending on the photon energy. This jump up is called *excitation* of the electron and this increase of energy through illumination is called *absorption*. If a photon has a slightly different energy level than the gap between the energy states, the electron completely ignores this photon. It must receive the exact amount of (usually expressed in) electron Volts to jump from one state to a higher state.

Reversely, an electron can jump down from its higher energy levels to any intermediate or ground state by emitting energy in the form of a photon with a particular wavelength. This jump down is called *de-excitation* and this decrease of energy is called *emission*.

In radiative transfer there is another important property referred to as *extinction*. This does not only refer to the phenomena that the intensity of light is reduced in the direction of propagation due to absorption, but it also accounts for the reduction in the intensity of light that is redirected in another direction than the direction of propagation, which is referred to as *scattering*. In the field of oceanography, absorption and scattering are also referred to as *Inherent Optical Properties* (IOPs) of particles.

[2]Illustration inspired by this video: https://www.youtube.com/watch?v=h3E9jNDnrDo

TABLE 2.2: *Radiometric quantities and units (Kamp, 2007)*

Quantity [symbol]	Units
Radiant energy $[Q]$	$[J]$
Radiant power or flux $[\Phi]$	$[W]$
Irradiance $[E]$	$[Wm^{-2}]$
Spectral irradiance $[E_\lambda]$	$[Wm^{-2}nm^{-1}]$
Intensity $[I]$	$[Wsr^{-1}]$
Spectral intensity $[I_\lambda]$	$[Wsr^{-1}nm^{-1}]$
Radiance $[L]$	$[Wm^{-2}sr^{-1}]$
Spectral radiance $[L_\lambda]$	$[Wm^{-2}sr^{-1}nm^{-1}]$

TABLE 2.3: *Solar spectrum and respective ranges of λ acquired from Bruno and Svoronos (2005). All λ are given in nm.*

Ultra-Violet (UV):	$10 < \lambda < 300$
Far Ultra-Violet	$10 < \lambda < 200$
Near Ultra-Violet	$185 < \lambda < 380$
Visible (VIS):	$380 < \lambda < 750$
Violet	$380 < \lambda < 450$
Blue	$450 < \lambda < 495$
Green	$495 < \lambda < 570$
Yellow	$570 < \lambda < 590$
Orange	$590 < \lambda < 620$
Red	$620 < \lambda < 750$
Near Infrared (NIR):	$750 < \lambda < 3000$

2.2.1.1 Radiative transfer

There are a few radiometric quantities that refer to the amount of energy that is transferred. First of all, there is the energy that is radiated by a source (such as the sun), referred to as *radiant energy*. The amount of radiant energy per unit of time is called the *radiant power*. The radiant energy and radiant power are expressed in respectively $[J]$ and $[W]$. Another quantity is called *irradiance*, which is the amount of power (or flux) per unit area ($\left[m^{-2}\right]$). If it is additionally expressed as a function of wavelength ($\left[nm^{-1}\right]$) it is referred to as *spectral* irradiance. In radiative transfer, however, another quantity is used; namely *intensity* (I), which is the amount of radiant power per unit of solid angle (i.e.; steradians ($\left[sr^{-1}\right]$)). Sometimes the intensity is also expressed as a function of wavelength, in which case it is referred to as *spectral* intensity. Another frequently used quantity is the *radiance*, which is defined as the amount of energy per unit area per unit solid angle. Similar to the intensity, radiance can also be expressed as a function of wavelength, in which it is referred to as *spectral* radiance[3]. The units corresponding with these quantities are given in Table 2.2.

Extinction is parameterized by an extinction coefficient, denoted by κ, and is dependent on the size-distribution, shape, optical properties of the particles and surrounding gas present in the line of propagation (Hansen and Travis, 1974). Recall that κ is quantified by the combined effect of absorption (denoted by α) and scattering. The scattering of light is parameterized by a scattering coefficient σ, which is a parameter that describes the likelihood of an effective area of a particle that causes light to be scattered by that particle. This is why this parameter is also referred to as the *scattering cross-section*. Note that this need not be the same as the actual cross-section of a particle, i.e. its *geometrical cross-section*. Finally, κ, for a particular wavelength, is expressed as;

$$\kappa = \alpha + \sigma \tag{2.2}$$

[3]Note that the spectral intensity (or spectral radiance) can also be expressed as a function of frequency, due to the relation between the frequency (ν) of an electromagnetic wave, λ and its velocity (c) in vacuum; $\lambda\nu = c$. In this case the quantities (see Table 2.2) are denoted as I_ν in $[Wsr^{-1}Hz^{-1}]$ and L_ν in $[Wm^{-2}sr^{-1}Hz^{-1}]$ (Lissauer and De Pater, 2013).

In radiative transfer, the change of I as it propagates through a medium (e.g.; the atmosphere) along the propagation path s, is due to the difference between emission (denoted by j) and κ, i.e.;

$$\frac{dI}{ds} = j - \kappa I \tag{2.3}$$

If a scenario is assumed in which there is no emission by the medium through which light propagates, i.e.; $j = 0$, the equation reduces to;

$$\frac{dI}{ds} = -\kappa I \quad \Rightarrow \quad I = I_0 e^{-\kappa s} \tag{2.4}$$

The exponent of Equation 2.4 is the *optical depth*, denoted by τ, and is defined by the integral of κ along the normal to the surface of the Earth (i.e. in the zenith direction, denoted by z);

$$\tau = \int_z \kappa(z) dz \quad \Rightarrow \quad \frac{d\tau}{dz} = \kappa \tag{2.5}$$

Note that the relation between z and s can be written as;

$$dz = \cos(\theta) ds \tag{2.6}$$

where θ is the zenith angle. An interesting expression occurs when the radiative transfer equation, including the emission factor, is expressed as function of τ. First Equation 2.6 is substituted in Equation 2.3;

$$\frac{dI}{dz/\cos(\theta)} = j - \kappa I \tag{2.7}$$

Upon substitution of τ this can be rewritten as follows;

$$\left(\frac{d\tau}{dz}\right)^{-1} \cdot \cos(\theta) \frac{dI}{dz} = (j - \kappa I) \cdot \kappa^{-1} \quad \Rightarrow \quad \cos(\theta) \frac{dI}{d\tau} = \frac{j}{\kappa} - I \tag{2.8}$$

Equation 2.8 is referred to as the **general equation of radiative transfer**. There is a simplification applied to this equation which assumes that light is propagated along the zenith, i.e.; $\theta = 0$ and thus $\cos(\theta) = 1$. Substitution in Equation 2.8 results in:

$$\frac{dI}{d\tau} = \frac{j}{\kappa} - I \tag{2.9}$$

The first right-hand term is defined as the *source function* $S = j/\kappa$. Incorporating these into the equation and solving the ODE yields;

$$\begin{aligned} &\frac{dI}{d\tau} = S - I \\ &\quad \Rightarrow I' e^{\tau} + I e^{\tau} = S e^{\tau} \quad \Rightarrow \quad \int_0^{\tau} \frac{d}{d\tau} \left[e^{\tau} I(\tau)\right] d\tau = \int_0^{\tau} S e^{\tau} d\tau \\ &\quad \Rightarrow e^{\tau} I(\tau) = I(0) + S(e^{\tau} - 1) \quad \Rightarrow \quad I(\tau) = S + e^{-\tau}(I(0) - S) \end{aligned} \tag{2.10}$$

This is the solution to Equation 2.3, in which $I(0) = I_0$ is the *background intensity*. τ is defined to be 0 at the top of the atmosphere and increases as light propagates through the atmosphere (Lissauer and De Pater, 2013).

The objective in applying the general equation of radiative transfer to a particular medium

is to calculate the intensity, irradiance or reflectance of light after it has passed through that medium. In order to apply the general equation of radiative transfer (Equation 2.3) to a particular medium, details of that medium must be provided. The particles in a medium, such as gases and aerosols within the Earth's atmosphere and their respective properties are examples of such details. After selecting which elements to include in a medium and after their optical properties have been defined, the propagation of light through that medium can be addressed by choosing one of the many *radiative transfer solvers* (Mayer, and Kylling, 2005) that are available.

2.2.1.2 Radiance versus reflectance

Throughout the year, as the Earth orbits about the Sun in an elliptical trajectory, the *extraterrestrial solar irradiance* $\mathcal{F}$ will vary with the Earth-Sun distance according to the following relation;

$$\mathcal{F} = \frac{\mathcal{L}_{\odot}}{4\pi r_{\odot}^2} \tag{2.11}$$

$\mathcal{L}_{\odot}$ is the *solar luminosity*, which is the radiant energy of the Sun per unit of time and amounts to $3.827 \times 10^{26} W$. $r_{\odot}$ is the *heliocentric* (i.e.; Earth-Sun) distance and is expressed in *astronomical units* (AU), where $1\ AU$ amounts to $1.496 \times 10^{11} m$. When $r_{\odot}$ is equal to 1, $\mathcal{F}$ is referred to as the *solar constant* (denoted by $\mathcal{F}_{\odot}$), which amounts to approximately $1366 W\ m^{-2}$ (Lissauer and De Pater, 2013).

From Equation 2.11 it is evident that $\mathcal{F}$ is a function of r and does not have a constant value. In order to avoid using a variable whose value changes throughout the year, the quantity *apparent reflectance* is introduced and is defined as follows:

$$\rho = \frac{\pi L\, r_{\odot}^2}{E'_{\odot} \cos\theta_s} \tag{2.12}$$

The apparent reflectance is the ratio of the radiance L to the solar irradiance $E_{\odot}$ and has a value between 0 and 1. In this equation any kind of radiance, L^{TOA} or L_w, can be converted to a reflectance. The solar irradiance, as can be seen in Figure 2.3, depends on λ but also on the distance between the Sun and the Earth. In RCM the spectral Solar irradiance (in units of $mW\ m^{-2}\ nm^{-1}$) is corrected for the distance between the Sun and Earth;

$$E'_{\odot} = E_{\odot}\left(1 + e\cos\left(2\pi\,\frac{day - 3}{diy}\right)\right) \tag{2.13}$$

where the variable diy stands for *days in year* and is the number of days in that calendar year, which can be 365 or 366 if it is a leap year. e is the Earth's orbital eccentricity and equals to 0.0167. The variable day is the number of days that has passed since 1 January of that calendar year.

2.2.1.3 Rayleigh scattering

Rayleigh scattering is caused by small particles suspended in the atmosphere, colouring the Earth's atmosphere a blue colour. This type of scattering has been described by Lord Rayleigh (Rayleigh, 1899) and a (very) simplified version of this scattering theory, including the Rayleigh scattering criteria and Rayleigh optical depth, will be discussed here. An underlying assumption of this theory is that the atmosphere contains isotropic and homogeneous spheres (McLinden, 1998).

FIGURE 2.3: *Solar spectrum as a function of λ, including a blackbody graph representing the radiation of the Sun, acquired from Lissauer and De Pater (2013).*

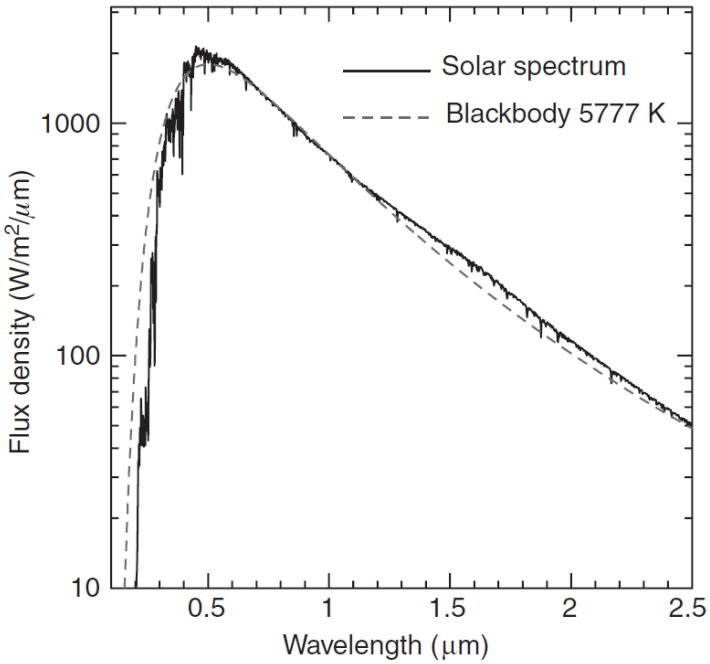

There are two conditions for Rayleigh scattering and they are related to the size parameter x and the complex index of refraction n_c. The size parameter is defined as

$$x = \frac{2\pi r}{\lambda} \tag{2.14}$$

in which r is the radius of the particle and λ the wavelength of radiation. One of the conditions for Rayleigh scattering is that the size parameter of the particle should be much smaller than λ, i.e.

$$x \ll \lambda \tag{2.15}$$

n_c is defined as;

$$n_c = n - i\kappa \tag{2.16}$$

where n is the index of refraction. n is the ratio of c, which is the velocity of light in vacuum, to the velocity of light in a particular medium, v (Kamp, 2007);

$$n = \frac{c}{v} \tag{2.17}$$

The complex term $i\kappa$ describes the absorption of light and n describes the refraction of light. The Second condition that must be met such that Rayleigh scattering occurs is that the size parameter must be much smaller than λ after light has passed through a particular medium, i.e.;

$$x \ll \frac{\lambda}{|n_c|} \tag{2.18}$$

The total optical depth, which is a kind of attenuation of intensity, consists of three contributions (Bodhaine et al., 1999);

- optical depth due to Rayleigh scattering (τ_R);
- optical depth due to aerosol scattering (τ_a); and
- optical depth due to gaseous absorption by e.g.; H_2O, O_3 and NO_2 (τ_g).

τ_R depends on the scattering cross section σ, the pressure P, Avogadro's number A[4], the mean molecular mass of the air m_a[5] and finally on the gravitational constant g;

$$\tau_R = \sigma \frac{PA}{m_a g} \tag{2.19}$$

σ is defined as (Bodhaine et al., 1999);

$$\sigma = \frac{24\pi^3 \left(n_s^2 - 1\right)^2}{\lambda^4 N^2 \left(n_s^2 + 2\right)^2} F_k \tag{2.20a}$$

$$F_K = \left(\frac{6 + 3\rho}{6 - 7\rho}\right) \tag{2.20b}$$

where N is the molecular density, n_s is n for *air* and F_K describes the effect of molecular anisotropy and is defined as the *depolarization term*[6] (also referred to as the *F(air)* or the *King factor*), where ρ is the *depolarization factor* (or *ratio*).

Rayleigh scattering is the most abundant type of scattering that occurs in the atmosphere. Looking at Equation 2.20a it can be seen that the amount of scattering is proportional to λ (when the dependence of δ and n on λ are ignored) as follows;

$$\sigma \propto \frac{1}{\lambda^4} \tag{2.22}$$

Looking at the spectrum of light, as provided by Bruno and Svoronos (2005) (Table 2.3) and using Equation 2.22, it can be stated that light with short λ scatters more than light with a

[4]The value of this parameter has been acquired from Lissauer and De Pater (2013) and has the value: $A = 6.022142 \times 10^{23} mole^{-1}$.

[5]Note that in Bodhaine et al. (1999) this parameter is referred to as molecular *weight*, which is in fact not a correct term since in physics weight is defined as the product of the mass and the gravitational constant, i.e.; $w = mg$.

[6]The origin of the depolarization term (Young, 1981), which is in fact a correction, has to do with the fact that anisotropic molecules scatter light more strongly compared to isotropic molecules for particular scattering angles. Initially it was Jean Cabannes who showed (in 1921) that the scattered intensity could be expressed in terms of ρ for randomly oriented molecules illuminated by unpolarized (i.e.; natural) light. For the same n, anisotropic molecules scattered more light than isotropic molecules and in the scenario of 90° scattering, a correction term was introduced and Cabannes quantified it to be

$$F_c = \left(\frac{6 + 6\rho}{6 - 7\rho}\right) \tag{2.21}$$

This strongly resembles F_K in Equation 2.20b but is referred to as the *Cabannes factor*. F_K was introduced because in 1923 Louis King discovered, contrary to Cabannes' assumption, that F_c was not applicable to the total scattering scenario due to the change in the angular distribution of the scattered light caused by the anisotropy. This underestimation of the total scattering by Cabannes was corrected for by King through the implementation of F_K as shown in Equation 2.20b.

long λ;

$$\begin{aligned} \sigma_{blue} &\propto \frac{1}{400^4} \approx 3.9e^{-11} \\ \sigma_{red} &\propto \frac{1}{620^4} \approx 6.8e^{-12} \end{aligned} \tag{2.23}$$

From the examples in Equation 2.23 it becomes clear that there is a $(3.9e^{-11}/6.8e^{-12} \approx) 6$ times higher likelihood that light with λ_{blue} scatters compared to light with λ_{red}, which is the reason why the atmosphere has a blue colour[7]. Along the same line of reasoning, it can be justified that the atmosphere should have a violet colour, because that has an even shorter λ. There are two reasons why this is not the case;

1. The sun emits less radiation at λ_{UV} than at λ_{VIS}. This becomes clear when looking at the graph of the blackbody radiation of the sun (see Figure 2.3). It can be seen that at $0.1\mu m$, which is more or less in the middle of λ_{UV} according to Table 2.3, the amount of radiation emitted by the sun is much less than at λ_{VIS}, or specifically, than λ_{blue}.

2. The human eyes are tuned to see blue, green and red colours more efficiently, i.e. human eyes are more sensitive to these colours and this sensitivity drops significantly for other λ (whyistheskyblue, 2013).

The two conditions for the occurrence of Rayleigh scattering (Equation 2.15 and Equation 2.18) are both met in case of molecules, which is why Rayleigh scattering is sometimes referred to as *molecular* scattering.

2.2.2 Aerosol models through MYSTIC simulations

In order to perform radiative transfer calculations of light propagation through the Earth's atmosphere a radiative transfer model can be used. These radiative transfer models, such as the software package called *libRadtran*, solve the equation of radiative transfer for a given distribution of optical properties. In DIMITRI a modified version of the libRadtran 3D Monte Carlo model, referred to as *MYSTIC*, is implemented and is used *"for the physically correct tracing of photons in cloudy atmospheres"* (Mayer, and Kylling, 2005). In MYSTIC the radiative transfer equation is 3 dimensional and the atmosphere is assumed to consists of parallel planes, referred to as the *plane-parallel* assumption. This assumption is generally valid for $\theta_s \leq 70°$. The relevant radiometric quantities that MYSTIC evaluates are the radiance L and the irradiance E.

The libRadtran package includes vertical profiles of many trace gases, e.g.; O_3, NO_2 or CO and many others[8]. In addition to the atmospheric composition, pressure and temperature profiles are also included. For a given altitude (i.e. level) these profiles provide information regarding the quantity in question. However, as opposed to this *level*-type definition of quantities, the radiative transfer solvers in libRadtran use a *layer*-type definition of such quantities. The quantities are then interpolated, either linearly or logarithmically, between two levels to give average layer properties for a given quantity.

[7] Interestingly, the oceans are blue not because of absorption or scattering at λ_{blue} but because of *vibrational transitions* that occurs between the Hydrogen and Oxygen bonds of the water molecules. In fact, the blue colour comes from selective absorption of red portions of λ_{VIS}, this absorption causes highly excited molecular vibrations and this causes the ocean to colour blue (M, 2008).

[8] For the complete list of the trace gases and their corresponding cross sections, see Table 2 in Mayer, and Kylling (2005).

DIMITRI has the capability to compare data that has been acquired by different satellites. The instruments on board these satellites vary in spatial resolution, radiometric precision, temporal coverage and spectral characteristics. In addition to these changes, given the fact that the measurements are made at different times and that the Earth, and its atmosphere, are highly dynamic, data will vary with sensor characteristics. A parameter that is used for data inter-comparison, is the relative spectral response of the instrument, which *"describes the quantum efficiency of a sensor at specific wavelengths over the range of a spectral band"* (Fleming, 2006). In order to make meaningful comparisons between instrument data, the effect of the relative spectral response of an instrument on broadband spectral measurements must be taken into account. The main issue is that the magnitude of the relative spectral response effect varies with spectral signatures of Earth observation features that are observed, for different instruments. This may result in inconsistencies of data and reduced accuracy and precision (Fleming, 2006).

Table 2.4 provides a list of different configurations which allows MYSTIC to simulate ρ_a. What is noticeable from Table 2.4 is that a selection of λ is made for which ρ_a is simulated. The instruments whose data are included in DIMITRI make observations on a particular λ. Each band has a *band width*, usually of a few nanometers, and each band has associated with it a relative spectral response. λ that are shown in Table 2.4 are chosen such that there are at least two λ that fall within the relative spectral response, for the purpose of data inter-comparison.

While the possibility in MYSTIC exists to use the vectorial mode[9] of the sea surface *bi-directional distribution reflectance function* (see Appendix B) that includes polarization, non-vectorial (*scalar*) equations originating from Cox and Munk (1954) are implemented. These equations describe the relationship between the distribution of the sea surface slope at different wind speeds in relation to the reflection and refraction from the sea surface[10]. The plane-parallel atmosphere assumption throughout the simulations is maintained whilst the possibility exists in MYSTIC to use a spherical shell atmosphere, in which the atmosphere is assumed to be a (homogeneous) spherical shell about the Earth (Spada, Krol, and Stammes, 2006). An advantage of the plane-parallel assumption is that the reflectance that is defined with respect to the irradiance directly above a specific point is equal to the irradiance at the sensor. For the spherical shell this would only be the case if sensor is directly above the viewing point ($\theta_v = 0°$). Another complication with the spherical shell atmosphere is that MYSTIC in libRadtran defines θ_s, θ_v and $\Delta\phi$ at the instrument and not at the surface (Hedley and Mazeran, 2013).

2.2.2.1 Maritime Clean aerosol model

The MC50 model is short for a Maritime Clean aerosol model and here the mass of the aerosols are given for a relative humidity of 50%. This aerosol model is implemented in DIMITRI and is described by Hess, Koepke, and Schult (1998).

The atmosphere is divided in 3 layers each of which contains a mixture of aerosols[11] (see Figure 2.4). The bottom layer is referred to as the *boundary layer* and extends from the sea

[9] The vectorial mode has been validated twice; against a MERIS atmospheric correction LUT and an independent model developed by the Finish meteorological institute, referred to as *Siro*.

[10] The method includes the translation of the statistics of the plane of the Sun's glitter pattern on the sea surface, to the statistics of the slope distribution.

[11] Note that the *mineral transported* layer, which extends from $2\,km - 3.5\,km$, has been ignored and not implemented in DIMITRI.

TABLE 2.4: *Parameters of the aerosol models (Barker et al., 2014). The angles are expressed in degrees and v_w is expressed in $m\,s^{-1}$.*

Parameters	n	Values
λ	386	$340 < \lambda < 1100\,nm\ -\ \delta\lambda = 4\,nm$ $1120 < \lambda < 5000\,nm\ -\ \delta\lambda = 20\,nm$
θ_s	9	0, 10.2229, 21.3480, 32.4790, 43.6114, 54.7444, 65.8776, 77.0110, 85
θ_v	9	0, 10.2229, 21.3480, 32.4790, 43.6114, 54.7444, 65.8776, 77.0110, 85
$\Delta\phi$	5	0, 45, 90, 135, 180
v_w	3	1.5, 5, 10
τ_a^{550}	7	0, 0.04, 0.06, 0.13, 0.53, 0.83

FIGURE 2.4: *The atmosphere with three distinct layers used for aerosol models.*

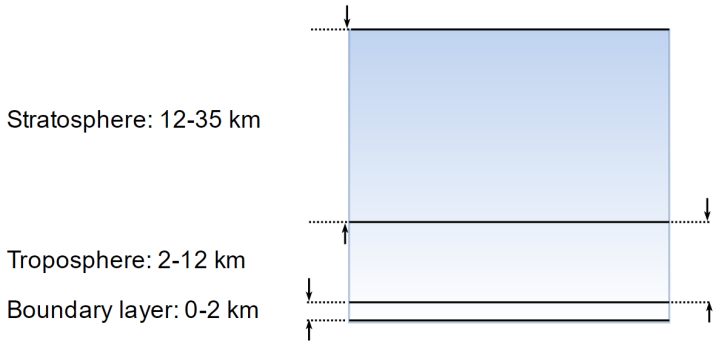

surface up to $2\,km$ and contains *water soluble* and *sea salt* aerosols[12]. The second layer is called the *free troposphere layer* and extends from $2\,km$ altitude up to the tropopause ($12\,km$). This layer contains water soluble and *insoluble*, *soot* and *sulphate droplets*. Out of these only water soluble aerosols reach the top layer of this boundary and have a density of 5 to 10 times higher than in the boundary layer (Barker et al., 2014). The third layer is referred to as the *free stratosphere layer* and is assumed to be between 12 and $35\,km$. The aerosol *Sulfate* (75% solution of Sulphuric acid in water: H_2SO_4) is used as the stratospheric background aerosol with a concentration of only 3 particles per cm^3. Sulfate is only to be considered for the calculation of τ and the results yield an optical depth of $\tau = 0.005$.

By default, the MC50 model has incorporated sea salt particles with an amount of 20 particles per m^3. Given that the concentration of particles is linked to the wind speed through an empirical relation developed by Koepke et al. (1997), the assumption of 20 particles per m^3 corresponds with a wind speed of 8.9 m/s. The sea salt particles make up for only 0.013% of all aerosols whereas the water soluble aerosol represents the large majority (98.7%). However soot, water insoluble and sulphate droplet aerosols are added in DIMITRI. The concentration of these aerosols could not be retrieved from the documentation that is available for the DIMITRI tool.

Each aerosol is described by a log-normal size distribution and refractive index. The properties of this distribution are the width of the distribution, the mode radius of the volume and

[12]Note that there are two modes in which sea salt is incorporated in order to account for the effect of wind speed on the increase of the number of particles and the different particle sizes. These two modes are called sea salt accumulated mode (SSAM) and sea salt coarse mode (SSCM).

number distribution and the upper and lower limits of the particle size. The radiative properties of aerosols are modelled with Mie theory. τ_a is the sum of the 3 aerosol(s) extinction coefficients that have been defined from altitude profiles for each of the 3 atmospheric layers in Figure 2.4[13].

2.2.2.2 MERIS atmospheric correction models

The MAR50 and the MAR99 are atmospheric correction models that incorporate 50% and 99% relative humidity, respectively. These have been developed for the MERIS instrument, which is the predecessor of the OLCI instrument and was on board the ENVISAT satellite. The term *atmospheric correction* means the identification of the ρ_w from ρ^{TOA}. This procedure determines ρ_a at λ^{865} and through spectral extrapolation the contribution of ρ_a to shorter λ is calculated. The accuracy of the atmospheric correction procedure thus depends heavily on the aerosol model and its capacity to quantify the wavelength dependency of the aerosol model and its ability to extrapolate between the NIR and blue wavelengths. For RCM, which uses Rayleigh scattering over the ocean, the *Maritime* aerosol model defined by Baker, Bourg, and Brockmann (2011) is included in DIMITRI.

MAR50 and MAR99 have been calculated using MYSTIC's Mie scattering tool (included in libRadtran) in its vectorial mode. This tool generates single scattering albedos and Mueller matrices[14] which are consequentially used as input by the libRadtran package. Additional input are the vertical profiles of aerosol components. The aerosol model is split in the same three layers as seen in Figure 2.4, with the difference that the stratosphere is defined up to 50 km. There are two components for the Maritime aerosol models with 50% and 99% relative humidity, the *rural aerosol mixtures* and *oceanic* components[15], which are both found in the boundary layer. The former is made up out of *water soluble* (70%) and *dust-like* aerosols (30%) and forms 99% of the particles in the Maritime model. The oceanic component consists out of the Sea-salt solution in water and forms only 1% of the Maritime model. The MAR50 has continental aerosols in the troposphere and H_2SO_4 in the stratosphere. The continental aerosols are water solubles, dust-like and soot components, which represent respectively 93.8998%, 0.0002% and 6.1% of the particles present. The atmosphere for the MAR50 and MAR99 consists of the following particles; molecules that cause Rayleigh scattering, aerosols that cause scattering and absorption, O3 and O2 & H_2O gases that result in absorption and finally clouds, which cause scattering and absorption.

2.2.3 Path reflectance

In subsection 2.2.2 it was explained which aerosol models are included in DIMITRI. The reason aerosol models are defined is to quantify ρ_a, which depends on τ_a^{865}. The procedure that is incorporated in the RCM to calculate τ_a^{865} requires knowledge of ρ_{path}, which is why this quantity is defined prior to the calculation of τ_a^{865}.

[13] Basic optical properties of aerosols are published in Koepke et al. (1997).

[14] These are matrices that can be used to *reproduce the effect of a given optical element when applied to a stokes vector.* The polarization state (e.g. linear, vertical or circular), for example, has a corresponding predetermined matrix structure that can be used. For more information, see http://scienceworld.wolfram.com/physics/MuellerMatrix.html.

[15] The parameters of the log-normal size distribution for the rural and oceanic aerosol components with 50% and 99% relative humidity, are given in Table 7-3 of Baker, Bourg, and Brockmann (2011). In addition, the aerosol optical properties for the Maritime model; single scattering albedo, scattering coefficient and extinction coefficient per MERIS sensor bands, are given in Table 10.2.

2.2.3.1 Theory

ρ_{path} includes all photons that have traveled through the atmosphere and have scattered more than 1 times, except for those that have traveled through the ocean. This is why in order to calculate this quantity, an atmospheric correction (AC) algorithm must be applied to 'filter' out L_w from L^{TOA}. Generally speaking, it is assumed that for AC algorithms ρ_R and ρ_a are separable. ρ_{path} is then quantified over a *black ocean* (meaning that $\rho_w = 0$) as the separable sum of the two components;

$$\rho_{path} = \rho_R + \rho_a \tag{2.24}$$

Equation 2.24 is valid only when *single scattering* is considered and can be viewed as an approximation of the *multiple scattering* case. However, in the NIR domain, approximately 30% of the scattered light is due to multiple scattering and thus AC algorithms that do not take multiple scattering into account fail to provide accurate solutions. Thus, the assumption that the two type of scattering can be separately quantified must be abandoned. Instead, Antoine and Morel (1999) have formulated the following *exact* definition for ρ_{path};

$$\rho_{path} = \rho'_R + \rho'_a + \rho_{R,a} \tag{2.25}$$

in which the components' definition is slightly changed. In Equation 2.24 ρ_R is defined in an aerosol-free atmosphere (referred to as *clear sky* or *clear atmosphere*) and ρ_a in a (hypothetical) molecular-free atmosphere (i.e.; only aerosols). In Equation 2.25 ρ'_R (or ρ'_a) quantify the reflectance due to solely Rayleigh (or aerosol) scattering, *but* in the presence of aerosols (or molecules). The last term in Equation 2.25 quantifies the reflectance as a consequence of successive multiple scattering by both molecules and aerosols. Antoine and Morel (1999) have expressed the increase in ρ_{path} as a consequence of adding aerosols to an aerosol-free atmosphere with the ratio;

$$\frac{\rho_{path}}{\rho_R} = \frac{\rho'_R + \rho'_a + \rho_{R,a}}{\rho_R} = f(\tau_a) \tag{2.26}$$

Because aerosols have an influence on multiple scattering, a relationship is defined between τ_a and the ratio ρ_{path}/ρ_R which can be used to solve τ_a^{865}. To explain this Figure 2.5 is taken from Antoine and Morel (1999).

Two ratios at two λ in the NIR are defined; $(\rho_{path}/\rho_R)_{\lambda=865}$ and $(\rho_{path}/\rho_R)_{\lambda=775}$[16]. In this procedure, these two ratios are considered to be the *true* ratios and will be used as a reference later on. Their values depend on the aerosol model that is chosen and this becomes clear when looking at the Marine aerosol model that has been plotted in Figure 2.5 for different values of relative humidity. Shettle and Fenn (1979) have explained that *"as the relative humidity increases, water vapor condenses out of the atmosphere onto the particulates suspended in the atmosphere. This condensed water increases the size of the aerosols and changes their composition and their effective refractive index. The resulting effect of the aerosols on the absorption and scattering of light will correspondingly be modified."* This effect is clearly illustrated in points 1 and 2 of Figure 2.5, where depending on the relative humidity, different τ_a values will be equal to the same $(\rho_{path}/\rho_R)_{\lambda=865}$ ratio. Through *spectral attenuation coefficients* of aerosols at $865\,nm$, the set of τ_a^{865} values are converted to a set of equivalent τ_a^{775} values (step 3). Using the same aerosol model with the same relative humidity settings, the set of τ_a^{775} values are matched with different $(\rho_{path}/\rho_R)_{\lambda=775}$ values (steps 4 and 5). When these are compared with the *true* $(\rho_{path}/\rho_R)_{\lambda=775}$ value, the two aerosol models that lie closest are selected to define a *mixing*

[16] In this calculation, ρ_{path} is the total reflectance because in the NIR it is assumed that there is no water-leaving reflectance. Furthermore, note that ρ_R is computed and is the Rayleigh reflectance in an aerosol-free atmosphere.

FIGURE 2.5: *A graphical representation of the two-band method (Antoine and Morel, 1999).*

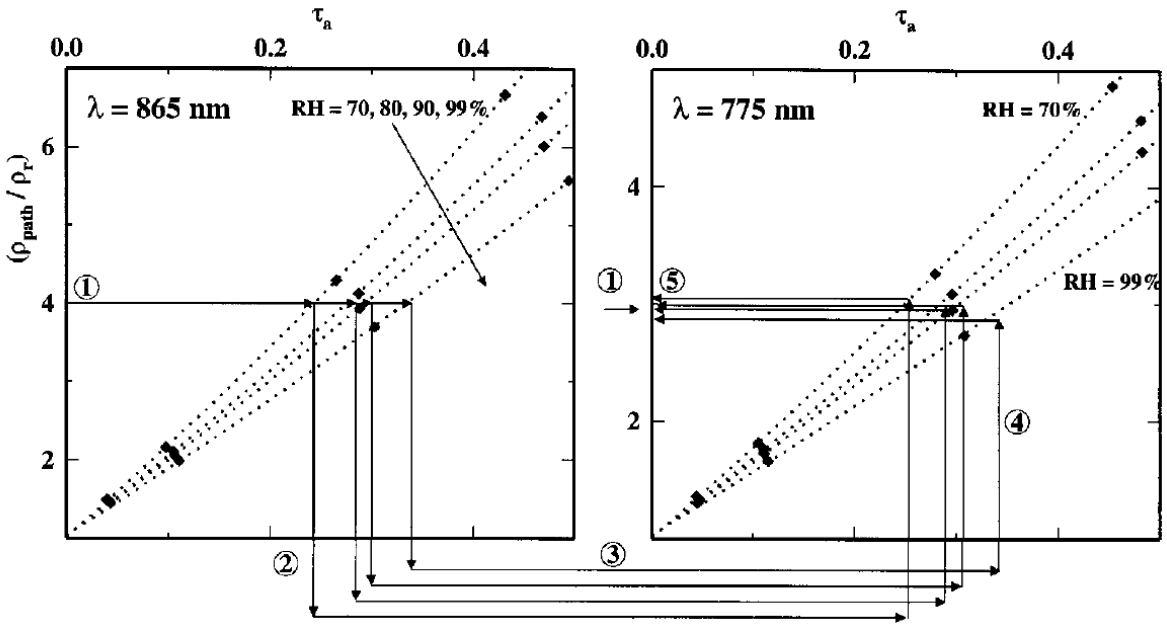

ratio, through which (ρ_{path}/ρ_R) in the visible domain can be determined from its values at λ =775 and 865 nm[17].

Antoine and Morel (1999) have included a correction term that accounts for computations of ρ_{path} with values for the pressure P that differ from the *standard* atmospheric pressure P_s, which is equal to $1023.25\,hPa$. This is necessary because ignoring variations can lead to significant errors in the AC procedure. In an atmosphere that contains molecules and aerosols this empirical correction term, resulting in ρ_{path} values to be achieved to within $\pm 0.5\%$, is defined as follows;

$$\rho_{path}^{P} = \rho_{path}^{P_s}\left(1 + \frac{P - P_s}{P_s}\eta\right) \tag{2.27}$$

where $(P - P_s)/P_s = \Delta P/P_s$ is the *pressure correction* term and η[18] is defined as;

$$\eta = \tau_R/\left(\tau_R + \tau_a\right). \tag{2.28}$$

2.2.3.2 Application to the Rayleigh Calibration methodology

In RCM, the ratio $(\rho_{path}/\rho_R)_{\lambda=865}$ is acquired through the evaluation of a quadratic polynomial, as a function of τ_a. For a given aerosol model (MC50, MAR50 or MAR99), viewing geometry $(\theta_s, \theta_v, \Delta\phi)$ and wind speed (v_w), a quadratic polynomial as a function of τ_a is fitted to values of $(\rho_{path}/\rho_R)_{\lambda=865}$. The only values that are stored in a Look-Up Table (LUT)[19] are the polynomial coefficients, which during the RCM are retrieved through linear interpolation as follows;

$$\frac{\rho_{path}}{\rho_R} = f\left(\lambda, \tau_a, v_w, \theta_s, \theta_v, \Delta\phi\right) = XC_0 + XC_1\tau_a + XC_2\tau_a^2 \tag{2.29}$$

[17]The remainder of the procedure will not be addressed. For more information please consult Antoine and Morel (1999).

[18]see page 48 of meris atbd 2.7 v5.1.

[19]These are tables that are used to store data in that can be loaded in DIMITRI when required by the RCM.

where XC_0, XC_1 and XC_2 are the coefficients of the polynomial fit corresponding to different aerosol models and the parameters shown in Equation 2.29 (Barker et al., 2014). Note that ρ_{path} can be acquired from Equation 2.29 by multiplying Equation 2.29 with ρ_R.

Now that the aerosol models are introduced, the AC procedure has been explained and ρ_{path} introduced, the retrieval of τ_a^{865}, as is implemented in the RCM, can be addressed. Beginning with ρ_{obs}^{TOA}, a correction for gaseous absorption is applied. This is achieved by determining the transmission, which is calculated for the geometry where the Sun is at the zenith (exactly above the point of observation) and the instrument has a nadir view (looking exactly down). These values are retrieved through linear interpolation as a function of λ. At this point ρ_{obs}^{TOA} data can be corrected for gaseous absorption in the following manner;

$$\rho_{obs_{O3}}^{TOA} = \rho_{obs}^{TOA} / t_{O_3} \tag{2.30}$$

where t_{O_3} represents the upward and downward gaseous transmission due to O_3. The procedure continues with the calculation of ρ_R, which is used in Equation 2.29 and is determined through linear interpolation of a LUT acquired through MYSTIC simulations. The interpolation is performed for particular values of λ, θ_s, θ_v, $\Delta\phi$ and v_w. Then, τ_R^{865} is calculated (Hansen and Travis, 1974) as follows[20];

$$\tau_R^{865} = 8.524e^{-3}\,\lambda^{-4} + 9.63e^{-5}\,\lambda^{-6} + 1.1e^{-6}\,\lambda^{-8} \tag{2.31}$$

The procedure to acquire ρ_a^{865} from the ratio $(\rho_{path}/\rho_R)_{\lambda=865}$ requires an iterative approach. An initial value of τ_a^{865} conform standard atmospheric conditions of 0.05 is used to correct ρ_{obs}^{TOA} for pressure variations as follows[21];

$$\rho_{obs_{O3_P}}^{TOA} = \rho_{obs_{O3}}^{TOA} \left(1 - \frac{\tau_R^{865}}{\tau_R^{865} + \tau_a^{865}} \left(\frac{P}{P_s - 1}\right)\right) \tag{2.32}$$

Then, ρ_{path}/ρ_R and all the other parameters shown in Equation 2.29 are used to retrieve the polynomial coefficients. Given that the ratio ρ_{path}/ρ_R is known *a priori*, an inversion of Equation 2.29 will be performed using positive values only to retrieve the polynomial coefficients in order to calculate the next estimate for τ_a^{865}. Within 3 iterations, the value for τ_a^{865} converges (Barker et al., 2014). Hagolle et al. (1999) emphasize that valid observations used for the estimation of the aerosols require a correction. Therefore, a threshold is applied for the purpose of selecting very clear atmospheres at $865\,nm$. This threshold is calculated by taking the product of the difference between ρ_R and the corrected observed ρ_{obs}^{TOA} and multiplying this with θ_s. The result of this product must be between 0 and 0.002. In addition, τ_a^{865} must also be larger than 0.

$$0 < \left(\rho_{obs_{O3_P}}^{TOA,\,865} - \rho_R^{865}\right)\theta_s < 0.002 \tag{2.33}$$

$$\tau_a^{865} > 0 \tag{2.34}$$

To recap, through the determination of the aerosol optical thickness in the NIR band it is possible to filter out the water-leaving reflectance from the top-of-atmosphere reflectance in the visible domain. This atmospheric correction procedure requires the propagation of the

[20] In the calculation of τ_R^{865} no pressure correction is applied (Hansen and Travis, 1974). In addition, the depolarization factor that is used here is $\delta = 0.029$ (Young, 1981).

[21] Note that in Barker et al. (2014) this step is noted different; ρ_{path} is replaced by ρ_{obs}^{TOA}. This is notation is valid because in the NIR domain, $\rho_w \approx 0$ and thus, in accordance with equation 6 of Antoine and Morel (1999) in which $\rho_{obs}^{TOA} = \rho_{path} + \rho_w$, ρ_{obs}^{TOA} reduces to ρ_{path}. However, this notation is not used here for purposes of clarity.

aerosol optical thickness from the NIR domain to the visible domain. Consequentially, the path reflectance in the visible domain can be acquired.

In DIMITRI a LUT is available that has 7 *reference* values for the aerosol optical thickness at a wavelength of 550 nm. The propagation from τ_a^{865} to τ_a^{λ}, is then simply acquired from linear interpolation of those values in the LUT for a particular aerosol model and λ. Note that the utilization of τ at 550 nm is due to its validity as a reference band in the remote sensing community[22].

2.2.4 Total transmittance

In order to perform the correction on ρ_{obs}^{TOA} for gaseous absorption, transmission factors available in DIMITRI are used (see Equation 2.30). These transmission factors are also used for the determination of the total downward and upward transmission. The procedure initiates by calculating the air mass M using the θ_s and θ_v in the following relationship;

$$M = \frac{1}{\cos\theta_s} + \frac{1}{\cos\theta_v} \tag{2.35}$$

The next step is to determine the optical thickness due to gaseous absorption, where O_3, O_2 and some trace gases are included. In DIMITRI, transmission factors, as a result of gaseous absorption are available in LUTs. Using the gaseous transmission values retrieved from these LUTs, the Ozone optical thickness denoted by τ_{O_3} is calculated using the following equation;

$$\tau_{O_3} = -0.5 \log \frac{t_{O_3}}{t_{O_x}} \tag{2.36}$$

where t_{O_x} represents the upward and downward gaseous transmission due to H_2O and O_2. After determination of the optical depth due to O_3 absorption in the NIR band, the amount of reflectance that is transferred through the atmosphere is calculated by applying Beer's law[23]:

$$t_{gas} = e^{-\tau_{O_3}\, O_3\, M} \tag{2.37}$$

O_3 concentration in the atmosphere is acquired from ECMWF, which provides the Total Columnar Ozone (TCO) database. The data file is expressed in the units $kg\,m^{-2}$ but is converted to Dobson Units (DU) in DIMITRI, which is a division by the constant: $2.1415 \times 10^{-5}\, kg\,m^{-2}$ [24].The total downward and upward transmittance, t_d and t_u respectively, are expressed as follows:

$$(t_{d,\,P}\, t_{u,\,P}) = (t_{d,\,P_s}\, t_{u,\,P_s})\, e^{-\frac{1}{2}\tau_R\, M\, (1+\Delta P/P_s)} \tag{2.38}$$

where $e^{-\frac{1}{2}\tau_R\, M}$ is the transmission due to Rayleigh scattering. The photons that are considered in MYSTIC's determination procedure for the transmission are those that have only been reflected from the Lambertian bottom boundary (i.e.; ρ_w in Equation 2.62d has a Lambertian BRDF[25]). This assumption introduces only minor errors and is valid for a diffuse reflectance up to 0.1. Note that t_d is a function of θ_s and t_u as a function of θ_v.

[22] It is also not an absorption band.

[23] According to Antoine et al. (2011) which address gaseous absorption for the MERIS instrument data, the altitude at which the Ozone layer is present results in a weakness of coupling between Rayleigh scattering and gaseous absorption. This means that the absorption and the scattering can be decoupled. Within this context, Equation 2.37 is valid.

[24] http://sacs.aeronomie.be/info/dobson.php

[25] For more information please go to Appendix B.

2.3 Wave propagation through water

The fundamentals of light propagation through the ocean, which will be addressed in subsection 2.3.1, are strongly related to Chlorophyll, as will become clear from the two following sections. This is why it is crucial that the measurement process of Chlorophyll is addressed in subsection 2.3.2. These two sections are the theoretical basis for the marine model in RCM (subsection 2.3.3).

2.3.1 Fundamentals

The scattering of light does not only occur in the atmosphere but it also occurs in water. Water contains small organic plants called *phytoplankton* (also referred to as *microalgae*) which are produced under the process of photosynthesis in the presence of released deep sea nutrients and sunlight. The concentration of these *inorganic* nutrients e.g.; nitrates, phosphates and sulfur, increases with depth (Herring, 1999). On the contrary, the amount of light reduces with increasing depth. Through various expeditions biologists and physicists came to the understanding that the Inherent Optical Properties (IOPs) depend on the concentration of phytoplankton present in oceanic water (Morel, 1988).

2.3.1.1 Water type classifications

Two classes of water have been distinguished which reflect the dependence of the IOPs on the content of the water;

Case-I Waters: Waters whose IOPs mainly depend on phytoplankton and detrital products (dead organic material)[26], either particulate (i.e. distinct) or dissolved.

Case-II Waters: Waters whose IOPs mainly depend on sediments and dissolved *yellow substance*, which are dissolved organic matter of terrestrial origin in some stage of decay (Barale and Schlittenhardt, 2012).

Morel (1988) explains that more than 98% of the oceans belong to the Case-I category. Morel (1988) furthermore indicates that often the only available index that can quantify the organic constituents of the Case-I waters is the Chlorophyll-a concentration (Chl-a)[27][28].

2.3.1.2 Diffuse attenuation coefficient for downwelling irradiance

As already mentioned, light attenuates as it propagates downwards through the water. The downwelling irradiance, E_d, can be measured with a spectroradiometer directly giving the energy of light (see Table 2.2). Another way E_d can be expressed is in terms of the amount of *Photosynthetically Available Radiation* (PAR) per unit of area per unit of time, denoted as PAR $m^{-2}\,s^{-1}$. PAR is the amount of photons that are available at a particular depth within the spectral range of $400 < \lambda < 700\,nm$. These photons are present in higher numbers closer to the surface and go all the way down until all light is completely attenuated. The layer that is formed from the surface to where the PAR is reduced to 1% of its surface value is called the *euphotic layer* and it is here that photosynthesis takes place. The in-situ measurements

[26] Detrital products are a by-product of phytoplankton.

[27] Chlorophyll are pigments that exist in the membrane of chloroplast with a green colour. The Chl-a is the principal photosynthetic pigment and it has a blue greenish colour in its pure state. (MajorDifferences.com, 2013)

[28] Another element is the pheophytin-a (Pheo-a) concentration, which is similar to Chl-a but it does not have a central Magnesium ion (Mg^{+2}). Together with the Chl-a the Pheo-a represent the pigment (i.e. colour) concentration present in the water. However, the main source for the pigment present in the water is due to Chl-a.

that have been made of the vertical distribution or profile of PAR have been used to calculate the *euphotic* or *photic depth* Z_e, which is the thickness of the euphotic layer. The *attenuation coefficient for downwelling irradiance*, denoted by K_d, is determined by measuring E_d at *null depth* (i.e.; just below the water surface, indicated by the $0-$); $E_{d,0-}$ and at a depth close to Z_e ($E_{d,Z}$) and it is expressed as;

$$K_d(\lambda) = \ln\left[E_{d,0-}(\lambda)/E_{d,Z}(\lambda)\right]/Z \tag{2.39}$$

E_d is obtained through in-situ measurements from the deck of a ship. Morel (1988) has estimated that the Chl-a in the euphotic layer varies between 3 to more than $300\,mg\,m^{-2}$. A mean pigment concentration variable has been defined as the sum of the Chl-a and the Pheo-a concentrations inside the euphotic layer, independent of the vertical PAR profile, and is designated $C\left[mg\,m^{-3}\right]$. However, Morel and Maritorena, 2001 have pointed out that the proportions in which Pheo-a was found in 1988 by Morel was often wrong. It is now acknowledged that the presence of Chlorophyll-b[29] led to an overestimate of Pheo-a (ambiguity was inherent to the fluorimetric measurement technique[30]). Morel and Maritorena (2001) state that Pheo-a exists in insignificant amounts compared to the Chl-a in the upper layers of the ocean and when small amounts were found, say $< 10\%$, it was included in the quantity Chl-a.

Another way in which K_d can be expressed is as follows;

$$K_d(\lambda) = K_w(\lambda) + K_{bio}(\lambda) \tag{2.40}$$

where K_{bio} is a term that represents the collective contributions of *biogenic components*, that are organic matter (e.g.; organic Carbon, Nitrates, Phosphates and other products of a biological origin (Emelyanov, 2001)). K_w is the *attenuation coefficient for pure water*, which is water that does not contain any suspended particles and thus their IOPs (i.e. scattering and absorption coefficients) are solely determined by molecules or ions. Pure waters are found in the open ocean and especially deep waters are those with high purity (Morel, 1974). K_w can be expressed as the summation of the absorption and Rayleigh scattering coefficients of optically pure water, a_w and b_w respectively (Emelyanov, 2001):

$$K_w^{fw}(\lambda) \geq a_w^{fw}(\lambda) + \frac{1}{2}\,b_w^{fw}(\lambda) \tag{2.41}$$

The inequality sign in Equation 2.41 can be set to an equality sign when it is assumed that the absorption of *freshwater* (fw), e.g.; Crater Lake (in Oregon, USA) where Equation 2.41 is based on, is similar to that of *saltwater* (sw)[31].

$$K_w^{sw}(\lambda) = a_w^{sw}(\lambda) + \frac{1}{2}b_w^{sw}(\lambda) \tag{2.42}$$

a_w and b_w are obtained from previous scientific papers where maximum[32] a_w values have been determined by Pope and Fry, 1997 and b_w values have been acquired from Morel (1974).

Interestingly, Equation 2.42 underestimates K_w and it represents the lowest experimental value that can be expected to be encountered in natural freshwater, based on laboratory measurements of the IOPs (Emelyanov, 2001). Morel and Maritorena (2001) argue that the

[29] Chl-b is the supplementary photosynthetic pigment and has an olive green colour in its pure state. (MajorDifferences.com, 2013).

[30] A technique with which the fluorescence is obtained.

[31] The 'sw' that is indicated in Equation 2.42 will hereafter be dropped for simplicity.

[32] The absorption coefficient for pure water has been selected where it has a maximum value, which occurs at $\lambda = 442\,nm$ (Morel and Maritorena, 2001).

final result does not depend heavily on the adopted K_w and that Equation 2.42 results in a deterioration of the goodness of the fit in the statistical relationship[33], especially when the water has low Chl-a values (called *oligotrophic* waters with Chl-a$< 0.3\,mg\,m^{-3}$) where K_{bio} approaches zero and thus K_d approaches K_w. Given that K_d is derived from E_d measurements and that K_w is approximated by a_w and b_w, K_{bio} is acquired from $K_d - K_w$ as a function of Chl-a (either acquired by measurements from filtered samples or values derived from continuous calibrated fluorescence profiles (Morel, 1988)). A linear regression is performed on the following log-transformed quantities:

$$\begin{aligned} y &= log[K_d(\lambda) - K_w(\lambda)] \\ y &= log[\textit{Chl-a}] \end{aligned} \tag{2.43}$$

This allows for K_{bio} to be expressed as[34]

$$K_{bio}(\lambda) = \chi(\lambda)\,\textit{Chl-a}^{e(\lambda)} \tag{2.44}$$

where χ and e are regression coefficients. This equation *estimates* K_{bio} as a function of Chl-a, for every λ. Substituting Equation 2.42 and Equation 2.44 in Equation 2.40 yields the following expression for K_d;

$$K_d(\lambda) = a_w(\lambda) + \frac{1}{2}b_w(\lambda) + \chi(\lambda)\,\textit{Chl-a}^{e(\lambda)} \tag{2.45}$$

To reiterate, K_d requires two quantities; the previously calculated $E_{d,z}$ and the downwelling irradiance at null-depth (i.e.; just beneath the water surface); $E_{d,0^-}$. $E_{d,0^-}$ is derived from measurements made *above* the surface and for every λ a transmittance factor (accounting for reflection losses at water-air interface[35]) is applied to convert the above-surface value to a beneath-surface value. The two quantities are processed to retrieve K_d. As a consequence of the use of the two types of measurement devices, E_d, and thus also its derivative K_d, are only valid for the range: $E_d, K_d < 600\,nm$[36].

2.3.1.3 Water reflectance mode

The reflectance, denoted here by R, is also referred to as the *irradiance reflectance* or *irradiance ratio* and is the ratio between the upwelling and downwelling irradiance; E_u and E_d respectively, at null depth;

$$R(\lambda) = E_{u,0^-}(\lambda)\,/E_{d,0^-}(\lambda) \tag{2.46}$$

R, in addition to being modelled is also measured at null-depth, denoted by R_0, for a range between 350 - 700 nm . $E_{u,0^-}$ is measured at a depth of $\sim 1-2\,m$. Similarly to $E_{d,0^-}$, E_d is calculated above water and is converted (by applying the transmittance factor) to just below the sea surface, yielding $E_{d,0^-}$. Both the irradiances are normalized using the incident solar flux.

[33] Within the spectral range of the PAR ($400 < \lambda < 700\,nm$) Morel (1988) performed a statistical analysis on the log transformed data at $5\,nm$ steps. This yields a significant linear relationship for the log-log plot of $K - K_w$ (see figure 7a of Morel (1988) through regression) as a function of the the mean pigment concentration C.

[34] The regression coefficients values (χ and e) in Equation 2.44 are tabulated with $5\,nm$ increments in table 2 of Morel and Maritorena (2001).

[35] This transmittance factor is applied for measurements for which the $\theta_s < 45°$ and is 0.965 (Morel and Maritorena, 2001).

[36] At shallow depths, downward irradiance values are characteristically noisy. The LICOR sensor and the custom built radiometer were only able to provide noise-free data at depths of $25-30\,m$ and $15-20\,m$ respectively. Due to this limitation, $E_d(\lambda)$ for $\lambda > 590-600\,nm$ could not be obtained. For more information please refer to Morel and Maritorena (2001).

Depending on the illumination conditions of the incident light, according to computations performed by Gordon et al. (1988), it was found that for $\theta_s \geq 20°$, R can be directly related to the absorption and *backscattering coefficient*, denoted by b_b, of the water. R is then expressed as[37];

$$R(\lambda) = f\left(\frac{b_b(\lambda)}{a(\lambda) + b_b(\lambda)}\right), \quad \text{if } b_b(\lambda) \ll a(\lambda), \text{ then } R(\lambda) = f\left(\frac{b_b(\lambda)}{a(\lambda)}\right) \tag{2.47}$$

f[38] is a function of the illumination conditions at the surface[39] and on the IOPs of the water[40] and therefore also on Chl-a and λ but its value has been fixed at 0.33[41] (Morel and Maritorena, 2001). R is then acquired by iteratively updating a and substituting the result in Equation 2.47 as follows:

$$a_i(\lambda) = K_d(\lambda)\, u_i \tag{2.48a}$$

$$R_i(\lambda) = f\,\frac{b_b(\lambda)}{K_d(\lambda)\, u_i} \tag{2.48b}$$

$$u_{i+1} = \mu_d\,\frac{1 - R_i(\lambda)}{1 + (\mu_d/\mu_u)\, R_i(\lambda)} \tag{2.48c}$$

$$R_{i+1}(\lambda) = f\,\frac{b_b(\lambda)}{K_d(\lambda)\, u_{i+1}} \tag{2.48d}$$

μ_u and μ_d are the average cosine values of the zenith and nadir angle for all upward and downward traveling photons (Kirk, 2011). Morel (1988) has pointed out that for a surface layer μ_d mainly depends on the solar elevation for which an average value of 0.9[42] is adopted. However, Morel and Maritorena (2001) introduce an alternative value for μ_d which takes into account the variations of μ_d with λ and also with Chl-a[43]. Morel (1988) also mentions that μ_u is approximately constant and is close to 0.4. Equation 2.48[44] has an implicit assumption that the reflection is independent of the depth, i.e. $d\rho/dZ \approx 0$. The iteration starts off by setting $u_i = 0.75$ and within 3 loops the iteration will converge. The first step of the iteration requires a value for K_d and this can be found in Figure 2.6.

[37] R_0 has been previously determined by Gordon and McCluney (1975), Prieur (1976), and Morel and Prieur (1977) where it is assumed that $b_b \ll a$. Morel and Maritorena (2001) state that this is usually true for Case-1 waters.

[38] f is a factor that combines the volume scattering function of the water and the above-water and in-water radiance distribution.

[39] described in Kirk (1984) and Gordon (1989).

[40] described in Morel and Gentili (1991).

[41] Morel and Gentili (1996) have a slightly different definition, wherein f varies from 0.324 for $\theta_s = 0°$ to 0.369 for a uniform sky. They state that f varies with water optical properties such as the single scattering albedo and with the illumiation conditions through θ_s. It also depends on the ratio of water molecular backscattering to the total (molecules plus particles) backscattering coefficients, denoted as $\eta_b(\lambda)$. v_w and τ_a also influence this parameter. For more information on the relationship of f on these parameters please refer to Morel and Gentili (1996).

[42] Kirk (1984) has quantified this value to be equal to 0.856: *"An average downward cosine of 0.856 for incident photons just after penetrating the surface would also be obtained with a direct solar beam at $\theta_s = 43.6°$"*. It is furthermore stated that μ_d decreases if photons travel through more oblique angles as opposed to angles closer to the outward normal. This results in a higher absorption / scattering probability. Under the assumption of a constant absorption, an ever increasing scattering results in the radiance field to approach the isotropic distribution. Under these circumstances, μ_d is equal to 0.5.

[43] These μ_d values are calculated for $\theta_s = 30°$ and can be found in Table 3 of Morel and Maritorena (2001).

[44] Note that this equation is a simplified version of Gershun's exact relation for the *divergence law for irradiance*.

FIGURE 2.6: *K_d values as a function of Chl-a, to be used in Equation 2.48. The dashed lines correspond with an old regression analysis performed by Morel (1988) and the straight lines correspond with a new analysis performed by Morel and Maritorena (2001).*

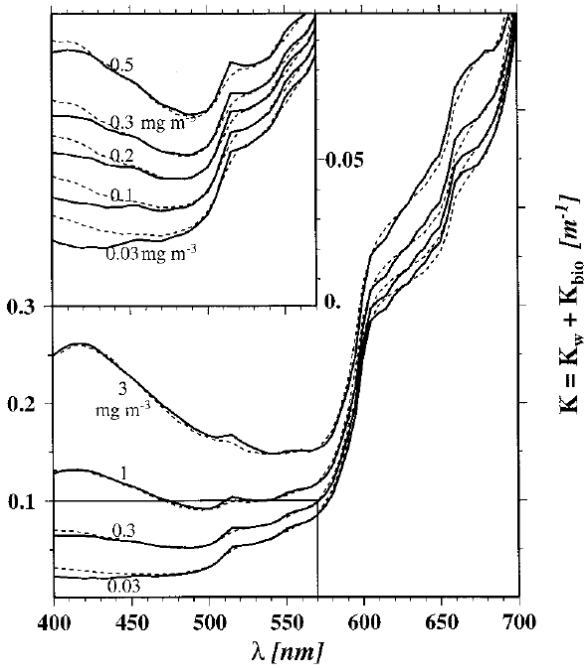

2.3.1.4 Backscattering coefficient

The b_b coefficient in Equation 2.47 consists of two terms, one term representing the backscattering coefficient of *optically pure sea water*; b_w, and the other represents the *particle backscattering*; b_{bp};

$$b_b(\lambda) = \frac{1}{2} b_w(\lambda) + b_{bp}(\lambda) \tag{2.49}$$

The first term on the right-hand side of Equation 2.49 is calculated as follows;

$$b_w = \frac{3\pi}{8}\beta(90)\frac{2-\delta}{1+\delta} \tag{2.50}$$

where δ is the *depolarization ratio*[45] and is defined as $\delta = i_2(\theta = 90)/i_1(\theta = 90)$. Here θ is the scattering angle relative to the incident light and $i_1(\theta)$ and $i_2(\theta)$ are the dimensionless functions of intensity and the two polarized components in the perpendicular (i.e. vertical) and parallel (i.e. horizontal) direction, respectively. Note that the $\theta = 90°$ indicates that light is scattered $90°$, i.e.; it is perpendicular to the direction of propagation. i_1 and i_2 are computed as follows;

$$\begin{vmatrix} i_1(\theta) \\ i_2(\theta) \end{vmatrix} = k^6 p^2 \begin{vmatrix} I \\ \cos^2\theta \end{vmatrix} \tag{2.51}$$

where k is referred to as the *wave number* and is defined as;

$$k = 2\pi/\lambda \tag{2.52}$$

[45] δ is the same quantity as ρ that is used in the calculation of the F_K that is present in Equation 2.20b, however, in order to stay consistent with literature the symbol δ is kept in Equation 2.50.

p is defined as the *polarizability* of the particle, i.e.; the particle's ability to become polarized and this is defined as follows;

$$p = \frac{n^2 - 1}{n^2 + 2} r^2 \tag{2.53}$$

r is the spherical radius of the particle (Morel, 1974). $\beta(90)$ in Equation 2.50 is referred to as the *volume scattering function at* $90°$ or *Rayleigh ratio* and is defined as;

$$\beta(90) = N \frac{I_{90}\, d^2}{I_0} = \frac{1}{2} N k^4 p^2 = N \frac{8\pi^4}{\lambda^4} p^2 \tag{2.54}$$

N in Equation 2.54 is the number of particles contained inside a unit of volume. Morel (1988) has evaluated Equation 2.50 with $\delta = 0.09$ (Morel, 1974).

Now, the second term on the right-hand side of Equation 2.49 is calculated using the following equation[46];

$$b_{bp}(\lambda) = \left(0.002 + 0.01\,(0.50 - 0.25\, log_{10}\textit{Chl-a})\left(\frac{\lambda}{550}\right)^{\nu}\right) \cdot b_p^{550} \tag{2.55}$$

where ν is is dependent on the Chl-a concentration (Morel and Maritorena, 2001);

$$\begin{cases} \nu = 0.5\,(log_{10}\textit{Chl-a} - 0.3) & 0.02 < \textit{Chl-a} < 2\, mg\, m^{-3} \\ \nu = 0 & \textit{Chl-a} > 2\, mg\, m^{-3} \end{cases} \tag{2.56}$$

b_p^{550} is derived from an empirical relation between the particle backscattering at $\lambda = 550\, nm$ and the Chl-a and is expressed as follows (Morel and Maritorena, 2001)[47];

$$b_p^{550} = 0.416\, \textit{Chl-a}^{0.766} \tag{2.57}$$

At this point a and b_b have been quantified and their relation to the reflectance has been addressed through the iterative procedure outlined in Equation 2.48. These IOPs have also been expressed as a function of Chl-a, which makes it possible to directly relate the reflectance to the Chl-a concentration present in Case-1 waters, for certain illumination conditions.

The empirical relationship that has been acquired for b_{bp} and Chl-a (see Equation 2.57) is established by Gordon and Morel (1983). b_b is a difficult parameter to model because it is poorly known. Therefore, Morel and Maritorena, 2001 have argued to include the size distribution and the composition of the particulate matter in oceanic waters by adding a term that varies depending on the amount of Chl present in the water. This is the reason for introducing ν as defined in Equation 2.56 and allows b_{bp} to be calculated using Equation 2.55, whilst taking the variations of b_{bp} as a function of Chl-a into account.

2.3.2 Chlorophyll data

In order to have accurate aerosol retrieval sites that have very stable Chl-a concentrations are chosen around the globe. This variable is critical to the RCM given that according to Barker et al. (2014) and Hagolle et al. (1999) it depends heavily on Chl-a. Hagolle et al. (1999) have selected 9 sites with a low Chl-a concentration and these are called *oligotropic waters* (see

[46] For more discussion on the derivation of this equation, please refer to Morel and Maritorena, 2001

[47] Note that this expression has been derived from a recent and large dataset specifically valid for the upper oceanic layer and is described by Loisel and Morel (1998)

Figure 2.7). Two extreme values of Chl-a have been derived from the ρ_w model developed by Morel (1988); either $17\,mg\,m^{-3}$ or $0.035\,mg\,m^{-3}$.

The following sensors are used for Chl-a measurements; HPLC, which stands for High Performance Liquid Chromatography, FL 3000 which is a fluorescence detector instrument and finally a CTD sensor which is a conductivity, temperature and depth sensor. The parameter [Chl] is defined as the sum of monovinyl and divinyl Chl-a when both pigments are present (and this is always the case in oligotrophic waters). Using the discrete pigment measurements made by the HPLC, the vertical profiles of algal fluorescence are converted into an equivalent [Chl] profile, as is illustrated by Figure 2.8. The mean [Chl] values are acquired through the integration of the [Chl] profile. See the flowchart on page 32 for the steps taken in order to compute mean Chl-a values.

FIGURE 2.7: *9 oligotrophic sites; sites that have stable Chl-a concentration values (image taken from Hagolle et al., 1999).*

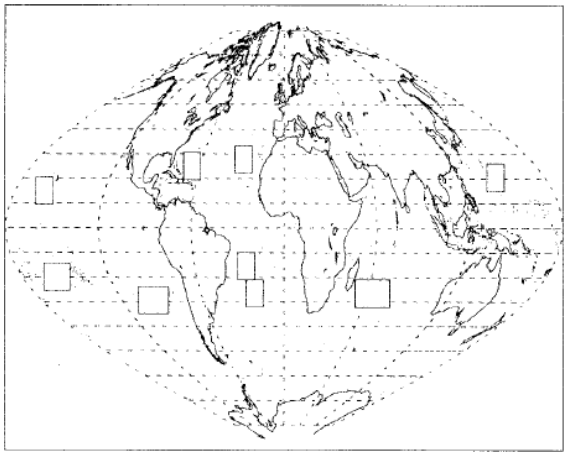

FIGURE 2.8: *Vertical Chl profiles converted from fluorescent profiles and 12 discrete HPLC data points (image taken from Morel and Maritorena (2001)).*

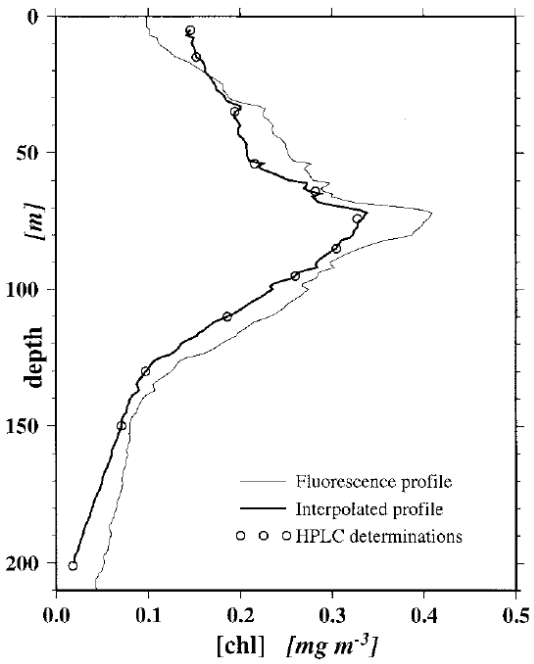

In the RCM an updated algorithm with an improved model and improved characterization of the IOPs of the oceanic constituents is implemented (Morel and Maritorena, 2001). A default value for Chl-a is $0.035\,mg\,m^{-3}$, but it is also possible to use a different Chl-a value. This value will then be extracted from a climatology database that has been developed by the European node for Global Ocean Colour (globcolour) (Bouvet, 2013). Fougnie et al. (2002) and Fougnie et al. (2010) have used SeaWiFS data, in combination with Aqua-MODIS and MERIS data, in order to generate a climatology of Chl-a over the global oceans covering a time span of 15 years (1998 - 2012). The climatology data is a merged dataset that is acquired through a match-up analysis that looked for satellite observations on a pixel level that coincide or lie sufficiently close to each other, and coalesced them into the merged dataset. Through the use of the Garver - Siegel - Maritorena (GSM) (bio-optical) *inversion model* described by Maritorena, Siegel, and Peterson (2002), which uses a non-linear fitting method to minimize the difference between the modelled and observed radiance, global Chl-a data have been retrieved.

This model uses IOPs such as b_w, a_w or a_{ph}[48] as input and they must be provided on a global scale in order to retrieve global Chl-a data. This is principally the opposite of what happens in the RCM, where these IOPs are given as input and the reflectance model simulates ρ_{obs}^{TOA}. The inverted (reflectance) model thus requires ρ_{obs}^{TOA} as input in order to retrieve Chl-a, or any other input parameter. One advantage of the merged dataset is the increase in coverage. Compared to the individual missions of SeaWiFS, Aqua-MODIS and MERIS, the improved coverage amounts to $73\% - 114\% - 225\%$, respectively.

The results that have been retrieved by the GSM inversion model, from using the merged dataset as input, have been compared with the individual sensor dataset. Maritorena et al. (2010), who performed a validation on the match-up analysis and the merged dataset, argue that the data agree well with individual satellite data retrievals.

The GSM inversion model uses a slightly different water reflectance model than implemented in the Rayleigh calibration methodology because the goal was to use the model globally. The main difference lies in how the IOPs and Apparent Optical Properties (AOPs) are mathematically defined (e.g.; b_b and K_d[49] Maritorena, Siegel, and Peterson (2002);

$$b_b(\lambda) = b_w(\lambda) + 0.252 \textit{Chl-a}^{0.635}(660/\lambda) \tag{2.58a}$$

$$K_d(\lambda) = \left(a(443)^2 + 0.256\, a(443)\, b(443)\right)^{0.5} \tag{2.58b}$$

The ρ_w implemented in DIMITRI has been compared, together with other models of its kind, with in-situ data in order to assess its quality. Brewin et al. (2013) have performed this comparison for semi-analytical and Chlorophyll models, which simulate IOPs (b_b, a and K_d) and Chl-a concentrations. This comparison proved to be inconclusive and did not identify 1 model as the *best* model. It turned out that each model had its own range in which it accurately simulated the parameters. In case of the GSM inversion model, it was shown by Morel and Maritorena (2001) and Maritorena, Siegel, and Peterson (2002) and reconfirmed by Brewin et al. (2013), that it has a high performance for determining parameters (such as a, a_{ph}, b_b and Chl-a concentration) at longer λ (i.e.; in the range of $\lambda > 560\, nm$) and low performance for the short λ (i.e.; in the range of $443 \leq \lambda \leq 489\, nm$) due to the large amount of ρ_R present at short λ.

2.3.3 Applications in DIMITRI

Now that the ρ_w model has been introduced its incorporation in the RCM can be explained. Morel and Gentili (1996) have defined $L_w(\theta, \phi)$ as follows;

$$L_w(\theta_v, \phi) = L_{u,0^-}\left(\theta'_v, \phi\right) \frac{\left[1 - \rho(\theta'_v, \theta_v)\right]}{n_w^2} \tag{2.59}$$

where $L_u(\theta'_v, \phi)$ is the *upward radiance* beneath the ocean surface at null depth[50], $\rho(\theta'_v, \theta_v)$ is the *internal Fresnel reflectance* for the directions θ_v, which is the viewing zenith angle in the air and θ'_v its corresponding refracted nadir angle in the water (see Figure 2.9). n_w is the refractive index for water. R has already been introduced (see Equation 2.46) but here a slight modification is applied, which underlines its dependence on θ_s, and this is denoted as; R_{θ_s}. $L_u(\theta'_v, \phi)$ is also a function of θ_s. In this case, a new function can be introduced that quantifies

[48] This is the absorption coefficient due to phytoplankton (Maritorena, Siegel, and Peterson, 2002).
[49] See equations 7 & 8 of Maritorena, Siegel, and Peterson (2002).
[50] Note that the symbol for null depth, 0^-, is not shown here.

FIGURE 2.9: *A schematic drawing (from Morel and Gentili (1996)) of the geometry with the Sun under a zenith angle of θ_0 (note this is symbolized by θ_s throughout this report), an observer under θ (denoted by θ_v), with its corresponding nadir angle refracted by the ocean of θ' (denoted by θ'_v). Also the relative azimuth angle is denoted by $\Delta\phi$.*

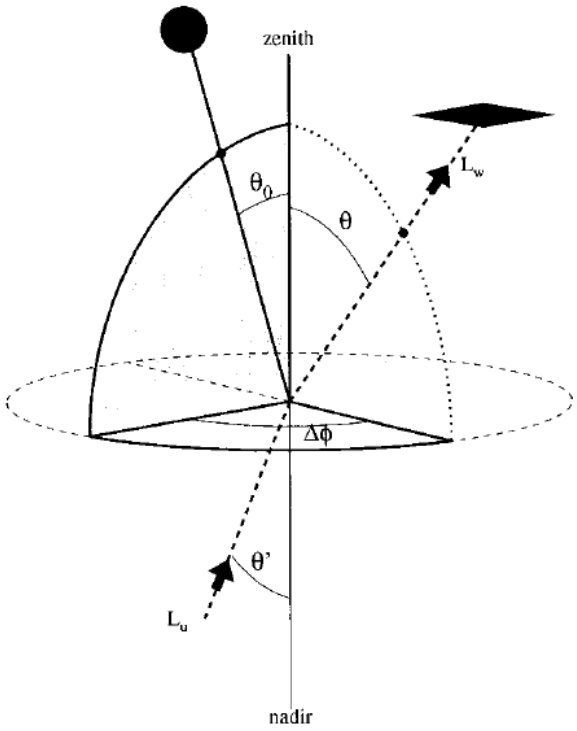

the *ratio of irradiance to any radiance* at null depth as follows;

$$Q(\lambda, \theta'_v, \theta_s, \Delta\phi) = E_{u,0^-}(\lambda) / L_{u,0^-}(\lambda, \theta'_v, \theta_s, \Delta\phi) \tag{2.60}$$

This Q function, given in units of steradians, is in fact a *bidirectional* function, for a particular angular dependence. If L_u is assumed to be isotropic then $Q = \pi$. Morel and Gentili (1996) formulate a *normalized* water-leaving radiance, $(L_w)_N$, which is the radiance that would be measured if the Earth is at the mean distance from the Sun. Consider also a case with no atmospheric extinction (i.e.; no absorption or scattering) and that the observer has a nadir-viewing instrument. Furthermore, take the Sun at the zenith, i.e.; $\theta_s = 0$, $\theta'_v = 0$, $\theta_s = 0$ and finally; $\Delta\phi = 0$. Under these assumptions, the $Q(\lambda, \theta'_v, \theta_s, \Delta\phi)$ function is reduced to $Q(\lambda, 0, 0, 0) = Q_0(\lambda)$. Similarly, since $\theta_s = 0$, R_θ reduces to R_0. The equation for $(L_w)_N$ can now be formulated as follows:

$$(L_w)_N(\lambda) = \frac{F_0 \mathcal{R}_0}{Q_0(\lambda)} R_0(\lambda) \tag{2.61}$$

$\mathcal{R}_0$ is a term[51] that merges all the reflection and refraction effects and depends on θ_v through the internal Fresnel reflectance $\rho(\theta'_v, \theta_v)$ and also depends strongly on the wind speed (Barker et al., 2014). Note that $\mathcal{F}_0$ is the *extraterrestrial solar irradiance* already defined in Equation 2.11.

[51] For a perfectly flat surface and a θ_v of 0°, Morel and Gentili (1996) have quantified $\mathcal{R}_0$ to be equal to 0.5278. Note that this term will not be derived here. For more information the reader is referred to page 4852 of Morel and Gentili (1996).

Equation 2.61 must be converted to a reflectance to take away its dependency on the varying $\mathcal{F}_0$ and this is achieved by using Equation 2.12;

1. Substitute $\mathcal{L} = (L_w)_N$ in Equation 2.12, (see Equation 2.62a).
2. Express $E = E_{d,0^+} = \mathcal{F}_0 \, \varepsilon \, t(\theta_s) \cos(\theta_s)$, where $E_{d,0^+}$ is the downwelling irradiance above the air-sea interface. ε is the ratio between the mean ($\bar{r}$) and actual (r) Earth-Sun distance, i.e.; $\varepsilon = (\bar{r}/r)^2$. $t(\theta_s)$ is the atmospheric diffuse transmittance (i.e. its effectiveness of transmitting radiant energy), (see Equation 2.62b).
3. Notice that the assumption of no atmospheric extinction results in the transmittance being 100%, i.e. $t(\theta_s) = 1$. Similarly, when the Earth is at its mean distance from the Sun; $d = \bar{d} \Rightarrow \varepsilon = (\bar{r}/\bar{r})^2 = 1$. Furthermore, given that in Equation 2.11 $r_\odot$ is expressed in AU and the Earth-Sun distance of 1 AU is the mean distance, the value of $r_\odot = 1$. In addition, when both θ_s and θ_v are equal to zero, $\cos(\theta_s) = \cos(\theta_v) = 1$, (see Equation 2.62c).
4. Cancel out the $\mathcal{F}_0$ quantity and formulate the ***marine model*** implemented by DIMITRI, (see Equation 2.62d).

$$\rho(\lambda) = \rho_w(\lambda) = \frac{\pi r_\odot^2}{E'_\odot \cos\theta} \frac{\mathcal{F}_0 \mathcal{R}_0}{Q_0(\lambda)} R_0(\lambda) \tag{2.62a}$$

$$\rho_w(\lambda) = \frac{\pi r_\odot^2}{\mathcal{F}_0 \, \varepsilon \, t(\theta_s) \, \cos\theta_s \cos\theta_v} \frac{\mathcal{F}_0 \mathcal{R}_0}{Q_0(\lambda)} R_0(\lambda) \tag{2.62b}$$

$$\rho_w(\lambda) = \frac{\pi}{\mathcal{F}_0} \frac{\mathcal{F}_0 \mathcal{R}_0}{Q_0(\lambda)} R_0(\lambda) \tag{2.62c}$$

$$\rho_w(\lambda) = \pi \frac{\mathcal{R}_0}{Q_0(\lambda)} R_0(\lambda) \tag{2.62d}$$

Morel and Gentili (1996) assume that oceans are homogeneous and the optical properties and the Chl-a are assumed to be uniformly distributed with depth in the (upper) oceanic layer. In addition, angular variations of $L_w(\lambda)$ are ignored and compensated in terms of deviations obtained in the Chl-a concentration.

The evaluation of Equation 2.62 in the RCM starts with the retrieval of a_w and b_w. a_w values are taken from Pope and Fry (1997) and are defined for a range between 380 - 700 nm, whereas b_w values are taken from Smith and Baker (1981) and are defined for a range between 200 - 800 nm. Both parameters are extracted from LUTs through linearly interpolation of λ. The LUT is simulated using refractive indices of water and ice in the 0.65 - 2.5 μm range and these originate from Kou, Labrie, and Chylek (1993). Then, for the evaluation of Equation 2.44, the regression coefficients calculated by Morel and Maritorena (2001) can be extracted by linearly interpolating the LUT for λ. The μ_d variable in Equation 2.48 is retrieved by linearly interpolating a LUT that contains simulated μ_d values as a function of λ, Chl-a and θ_s.

Now that all the necessary elements of Equation 2.1 have been explained, the calibration coefficient, C, can be calculated. It should be noted that the RCM is only valid for particular λ. Hagolle et al. (1999) underline this by stating that C is only determined for the *blue* spectral bands because at these λ the Rayleigh scattering is well characterized by radiative transfer models. In addition, because measurements in the glint are not included, Equation 2.1 reduces to the following expression;

$$\rho_{sim}^{TOA} = t_{gas} \, (\rho_{path} + t_{down} \, t_{up} \, \rho_w) \tag{2.63}$$

2.4 Conclusion

It should be reiterated that this tedious and quantitative dispensation of information serves the purpose of identifying possible sources of systematic uncertainties that can be attributed to the input variables and/or to the RCM algorithm. In addition, to depict the complexity and breadth of this objective, a spreadsheet has been drawn and can be seen on the next page. What becomes clear is that there are many steps that collectively define the RCM and that there are many assumption that have been made that eventually lead to obtaining the calibration coefficient.

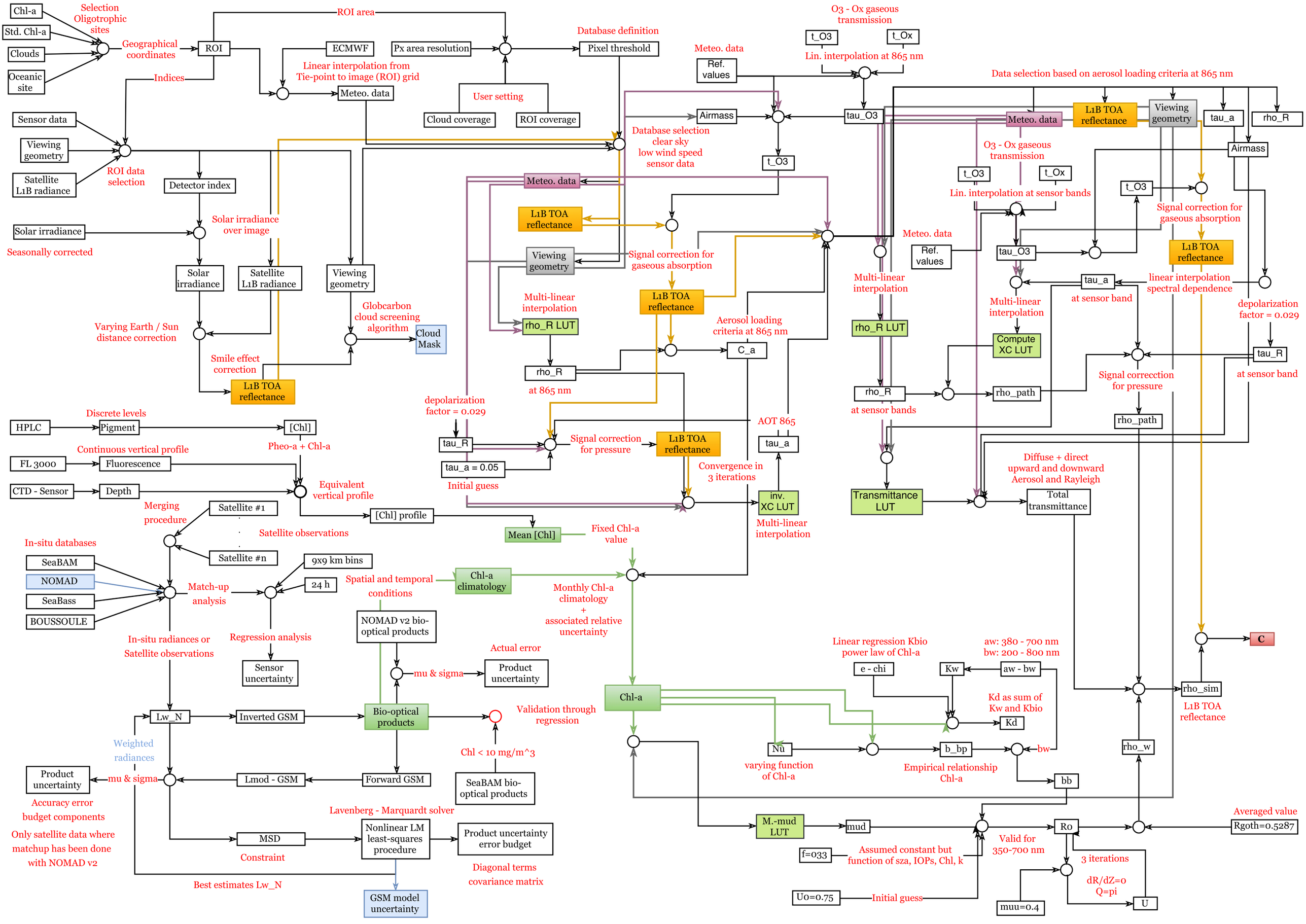
Chl-a
Std. Chl-a
Clouds
Oceanic site
Selection Oligotrophic sites
Geographical coordinates
ROI
ROI area
ECMWF
Px area resolution
Database definition
Pixel threshold
Indices
Linear interpolation from Tie-point to image (ROI) grid
Meteo. data
User setting
Cloud coverage
ROI coverage
Sensor data
Viewing geometry
Satellite L1B radiance
ROI data selection
Detector index
Solar irradiance
Seasonally corrected
Solar irradiance over image
Solar irradiance
Satellite L1B radiance
Viewing geometry
Varying Earth / Sun distance correction
Globcarbon cloud screening algorithm
Cloud Mask
Smile effect correction
L1B TOA reflectance
Meteo. data
Ref. values
Airmass
Database selection clear sky low wind speed sensor data
t_O3
t_Ox
O3 - Ox gaseous transmission
Lin. interpolation at 865 nm
tau_O3
Meteo. data
L1B TOA reflectance
Viewing geometry
Signal correction for gaseous absorption
Multi-linear interpolation
rho_R LUT
rho_R
at 865 nm
L1B TOA reflectance
Aerosol loading criteria at 865 nm
C_a
depolarization factor = 0.029
tau_R
tau_a = 0.05
Initial guess
Signal correction for pressure
L1B TOA reflectance
Convergence in 3 iterations
AOT 865
tau_a
inv. XC LUT
Multi-linear interpolation
Data selection based on aerosol loading criteria at 865 nm
Meteo. data
L1B TOA reflectance
Viewing geometry
tau_a
rho_R
Airmass
O3 - Ox gaseous transmission
t_O3
t_Ox
Lin. interpolation at sensor bands
t_O3
Signal correction for gaseous absorption
Meteo. data
Ref. values
tau_O3
L1B TOA reflectance
Multi-linear interpolation
tau_a
at sensor band
linear interpolation spectral dependence
depolarization factor = 0.029
rho_R LUT
Compute XC LUT
tau_R
at sensor band
rho_R
at sensor bands
rho_path
Signal correcction for pressure
rho_path
Transmittance LUT
Total transmittance
Diffuse + direct upward and downward Aerosol and Rayleigh
HPLC
Pigment
[Chl]
Discrete levels
Pheo-a + Chl-a
FL 3000
Fluorescence
Continuous vertical profile
CTD - Sensor
Depth
Equivalent vertical profile
[Chl] profile
Mean [Chl]
Fixed Chl-a value
Merging procedure
Satellite #1
Satellite #n
Satellite observations
In-situ databases
SeaBAM
NOMAD
SeaBass
BOUSSOULE
Match-up analysis
9x9 km bins
24 h
In-situ radiances or Satellite observations
Regression analysis
Sensor uncertainty
Spatial and temporal conditions
Chl-a climatology
Monthly Chl-a climatology + associated relative uncertainty
NOMAD v2 bio-optical products
Actual error
mu & sigma
Product uncertainty
Chl-a
Linear regression Kbio power law of Chl-a
e - chi
Kw
aw - bw
aw: 380 - 700 nm
bw: 200 - 800 nm
Kd as sum of Kw and Kbio
Kd
Nu
varying function of Chl-a
b_bp
Empirical relationship Chl-a
bw
bb
rho_w
rho_sim
L1B TOA reflectance
C
Lw_N
Inverted GSM
Bio-optical products
Validation through regression
Chl < 10 mg/m^3
SeaBAM bio-optical products
Weighted radiances
mu & sigma
Lmod - GSM
Forward GSM
Product uncertainty
Accuracy error budget components
Only satellite data where matchup has been done with NOMAD v2
Lavenberg - Marquardt solver
MSD
Constraint
Nonlinear LM least-squares procedure
Product uncertainty error budget
Diagonal terms covariance matrix
Best estimates Lw_N
GSM model uncertainty
M.-mud LUT
mud
f=033
Assumed constant but function of sza, IOPs, Chl, k
Uo=0.75
Initial guess
Ro
Valid for 350-700 nm
3 iterations
dR/dZ=0
Q=pi
muu=0.4
U
Averaged value
Rgoth=0.5287

Chapter 3

DIMITRI

Now that the reflectance model in RCM is addressed, the DIMITRI tool itself will be very briefly introduced, focusing on its general capabilities. Within this chapter, the user interface of DIMITRI is briefly described to give the reader some handles on how the RCM for a sensor such as OLCI can be initiated and executed.

In the introduction to this thesis it was already explained why DIMITRI is used. In this chapter some general introductions are given. Figure 3.1[1] shows a flowchart displaying the different parts of the DIMITRI tool.

In DIMITRI a database is used to store Level 1B (L1B) radiometric data[2], which are reflectances observed by instruments on board Earth observation satellites. The 'L1B Ingestion' option of the tool allows the user to add new data to the existing database. The data is always associated with a geographical area on the Earth. This region of interest (ROI) can be on land (e.g. desert) but also on water (e.g. the South Pacific Gyre).

The new data is loaded and processed[3] in a standardized manner by the tool before it is stored in the database, ready for an inter-comparison procedure. For each band within the optical sensor's operational spectrum, an average and standard deviation of the reflectance is computed. The data is also prepared on a pixel-by-pixel basis, containing reflectances for all pixels within the ROI. Note that 1 file that contains all pixels within a ROI is colloquially referred to as an acquisition.

There are two options available within the tool to perform an inter-comparison procedure; the *Rayleigh* and the *Glint*[4] calibration methodology. After choosing the procedure, inter-comparison settings and aerosol model to be used in the reflectance model, the procedure can be started. Note that for the execution of this step auxiliary data are required regarding the atmospheric and oceanic constituents and spectral representation of the ROI (see large gray box before the 'Intercomparison Methodology' red box).

The calibration coefficient that is calculated on a pixel-by-pixel basis is stored in a database. For each sensor band, an average of all pixels within the ROI is determined and stored in an Excel output file, in addition with associated statistical data of those calibration coefficients

[1] Flow chart has been drawn using the following website: https://www.draw.io/

[2] See Appendix C for an explanation of the processing levels.

[3] The radiometric data are given as radiances and DIMITRI converts these to reflectances. In addition, a cloud screening correction is performed for all pixels that contain clouds. Furthermore, the data are also corrected for the smile effect and seasonal variations of the solar irradiance throughout Earth's orbit around the Sun.

[4] Note that in this thesis the Glint calibration methodology is not taken into account but it is mentioned because it is based on the same reflectance model that is described by Hagolle et al. (1999). In addition to the Rayleigh and Glint calibration methodology, there exists also a third option; a desert calibration procedure. However, this methodology is based on a different reflectance model.

(standard deviation, mean and uncertainty of those coefficients). Besides these databases, DIMITRI plots the average calibration coefficients and their temporal changes over 1 year.

FIGURE 3.1: *DIMITRI's Flowchart. The **red highlighted boxes** indicate the steps that take place in DIMITRI in order to execute an inter-comparison procedure. The **gray highlighted boxes** show what input are required for the inter-comparison procedure. The **green highlighted boxes** show reflectance model settings and they can be 'tweaked' prior to the execution of the inter-comparison. The **blue highlighted box** shows the output files.*

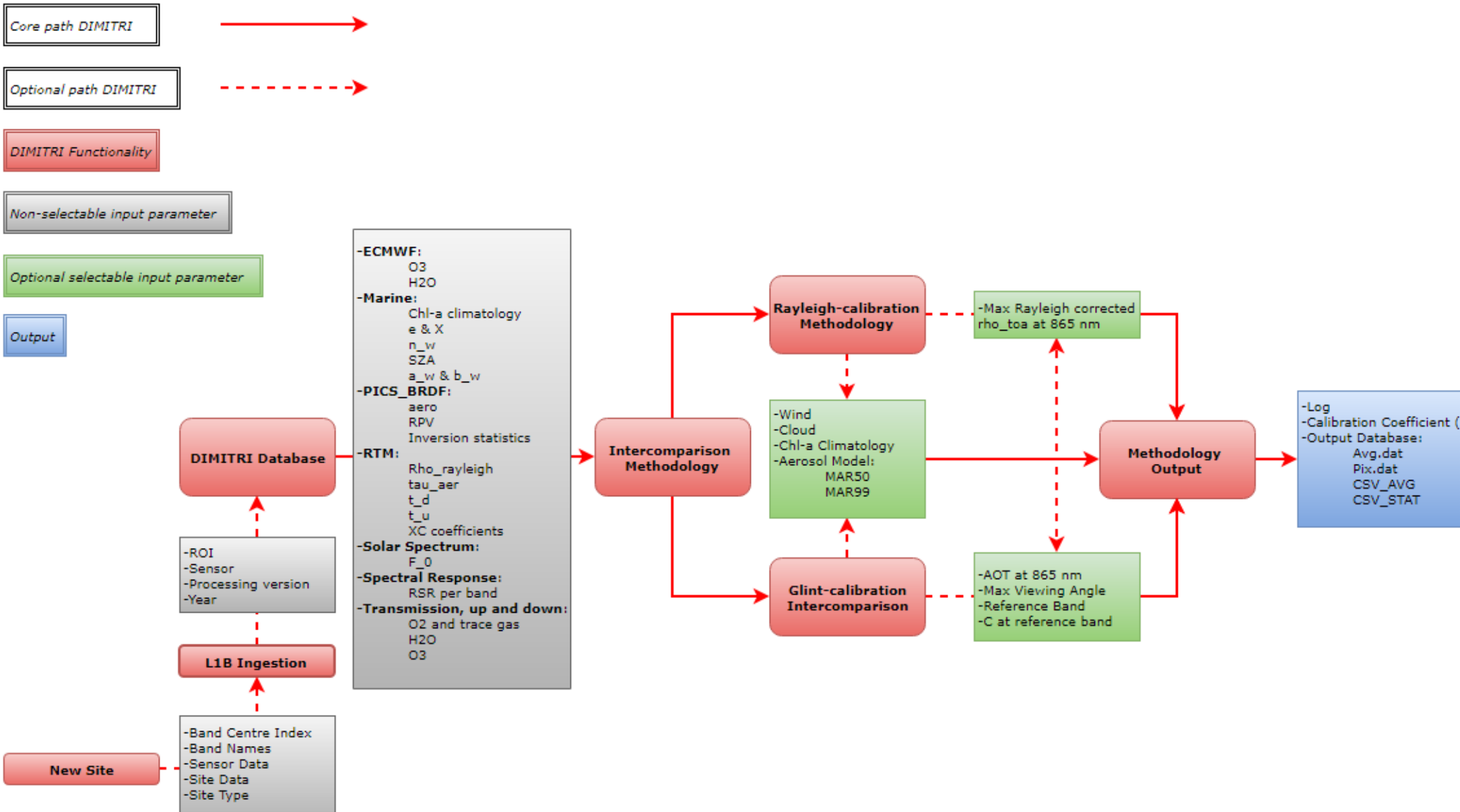

Chapter 4

Uncertainty propagation theory

In this chapter, in accordance with the recommendations outlined by the Comitè International des Poids et Mesures, in 1980 (called Recommendation INC-1) (BIPM et al., 2008), the fundamentals of uncertainty analysis and propagation are addressed section 4.1 & section 4.2. In section 4.3 the two types of uncertainties are explained and some preliminary classification is attempted.

4.1 Uncertainty propagation methodologies

In this thesis the focus lies on two different propagation methodologies; the simulation-based *Monte Carlo (MC)* method and the expansion-based *Taylor series expansion* (TS) method. The MC method is a brute force approach where through many simulations the uncertainty components are obtained. An alternative to this inefficient approach is the TS method, where through the calculation of partial derivatives an analytical expression is obtained that directly yields the uncertainty components in one evaluation.

Let $f(\mathbf{x})$ denote the function (i.e. the RCM) and $\mathbf{x}$ be the input variable. In addition, let the output of the function (i.e. the calibration coefficient) be denoted by C. Furthermore, let the mean of C be denoted by μ_C and the standard deviation of C be denoted by σ_C. Mathematically, if the ouput distribution is Gaussian, these two uncertainty components are defined as follows;

$$\mu_C = \frac{1}{n}\sum_{i=1}^{n} C_i \tag{4.1}$$

$$\sigma_C^2 = \frac{1}{n-1}\sum_{i=1}^{n} \left(C_i - \mu\left(C_i\right)\right)^2 \tag{4.2}$$

where n is the number of samples within a population. If the output distribution is uniform, the following equations hold;

$$\mu_x = \frac{C_{min} + C_{max}}{2} \tag{4.3}$$

$$\sigma_x^2 = \frac{\left(C_{max} - C_{min}\right)^2}{12} \tag{4.4}$$

4.1.1 Monte Carlo simulations

The MC method is a simulation-based method that does not require any simplification of $f(\mathbf{x})$ and the uncertainty components are simply obtained from the evaluation of the aforementioned equations with respect to the output distribution.

In order to obtain a distribution of the output, the input variables must be changed before each simulation. This *change* can be viewed as an error (denoted by ε) and can be derived from the variability of the input variables, say $\sigma_{\mathbf{x}}$. I hereby make the assumption that the

input variables are uniformly distributed random variables. Under this assumption, each variable can be written as the arithmetic mean of that variable plus an error;

$$\mathbf{x}' = \mu_{\mathbf{x}} + \varepsilon_{\mathbf{x}} \tag{4.5}$$

$\varepsilon_{\mathbf{x}}$ changes with every simulation which causes every evaluation of $f(\mathbf{x})$ to yield a different value for C. After many simulations, a distribution of C values is be obtained, from which μ_C and σ_C are determined.

It should be noted that, for a Gaussian distribution, the true μ can never be known and that Equation 4.1 will only yield an approximation of μ_C. Therefore, the mean will now be denoted by $\bar{C}$. Similarly, because the *true* σ is never known, a better term to describe the standard deviation is the *experimental standard deviation* and this is denoted by S. The uncertainty u associated with $\bar{C}$ is called the *standard deviation of the mean* and the uncertainty associated with S is called by the *standard deviation of the standard deviation*[1]. These two uncertainties are quantified as follows (Taylor, 1997)[2];

$$u(\mu_C) = \frac{\sigma_C}{\sqrt{n}} \tag{4.6}$$

$$u(\sigma_C) = \frac{\sigma_C}{\sqrt{2(n-1)}} \tag{4.7}$$

From these two equations it becomes obvious that the number of simulations n has an impact on the uncertainty. Some examples of this have been given in Table 4.1.

TABLE 4.1: *Relative uncertainties due to the finite number of simulations in percentages.*

n	2	10	50	100	1000	10000	100000
$u(\mu_C)$	70.71%	31.62%	14.14%	10.00%	3.16%	1.00%	0.32%
$u(\sigma_C)$	70.71%	23.57%	10.10%	7.11%	2.24%	0.71%	0.22%

So far it has been assumed that the input variables follow a uniform distribution. Under a linear transformation, such as the Taylor series expansion, the output will also have a Uniform distribution (Arras, 1998). With the MC method, no linearization is performed and thus the output distribution need not be Uniform and can be Gaussian. In order to assess whether this is the case, a χ^2 test can be performed on the output. In this test, the output distribution is assessed based on how well it compares with what would be an *expected* Gaussian distribution. A Gaussian distribution can be divided into 4 sections (denoted by s), each containing an expected *number* of output samples which are denoted by E_s. The expected number of samples within a section are then compared with the actual number of samples (denoted by C_s) that are obtained from the MC simulations using the following equation;

$$\chi^2 = \sum_{i}^{s} \frac{(C_s - E_s)^2}{E_s} \tag{4.8}$$

χ^2 is an indicator of the agreement between the observed and expected output distribution and if $\chi^2 \leq s$, the output distribution has an expected Gaussian distribution.

[1] Note that the expression given here is an approximation, the exact expression is $\sigma_{S_{\bar{C}}}/\sigma_{\bar{C}}$, see BIPM et al. (2008).

[2] Note that Equation 4.7 is also referred to as the Margin of Error (MoE).

4.1.2 Taylor series expansion

The Taylor series expansion about $\mathbf{x} = \bar{\mathbf{x}}$ of $f(\mathbf{x})$ is defined as;

$$C \simeq f(\bar{\mathbf{x}}) + \frac{\partial f}{\partial \mathbf{x}}|_{\mathbf{x}=\bar{\mathbf{x}}} (\mathbf{x} - \bar{\mathbf{x}}) \tag{4.9}$$

Note that $f(\mathbf{x})$ indicates that this is a multi-variate function because $\mathbf{x}$ is a vector. Arras (1998) have derived $\bar{C}$ and S_C;

$$\bar{C} \approx f(\bar{\mathbf{x}}) \tag{4.10}$$

$$S_C^2 \approx \sum_i^n \left(\frac{\partial f}{\partial x_i}\right)^2 u_{x_i}^2 + \sum_i^{n-1} \sum_j^n \left(\frac{\partial f}{\partial x_i}\right) \left(\frac{\partial f}{\partial x_j}\right) u_{x_i, x_j} \tag{4.11}$$

If correlation between the input variables is disregarded then $u_{x_i, x_j} = 0$ and a simpler term can be obtained;

$$S_C^2 \approx \sum_i^n \left(\frac{\partial f}{\partial x_i}\right)^2 u_{x_i}^2 \tag{4.12}$$

Here we have arrived at the point where similar quantities are obtained from the analytical propagation of uncertainties as previously obtained from the MC simulations. However, BIPM et al. (2008) define Equation 4.11 as '*an estimated standard deviation that characterizes the dispersion of values that could reasonably be attributed to the measurand*'. It is important to remember that these two quantities are based on the linearization of $f(\mathbf{x})$. Arras (1998) state a condition for whether the statements in Equation 4.10 and Equation 4.11 are valid and it requires $f(\mathbf{x})$ not to be too non-linear within $\pm S_C$. Only then will the TS method be a sufficient approximation of the uncertainty components obtained through the MC method. Additionally, the TS method implicitly 'hopes' that $\bar{\mathbf{x}}$, which is an *estimation* of the actual value of x, lies sufficiently close to the expectation of x such that C, lies sufficiently close to the expectation of C. Depending on these two conditions, the approximation of e.g. S_C^{MC} by S_C^{TS} can be very poor.

The extent of the nonlinearity of $f(\mathbf{x})$ remains to be determined conclusively. For the time being a more elaborate TS including higher-ordered terms will be introduced in case the strong nonlinearity of $f(\mathbf{x})$ is affirmed. In that case, S_C is calculated using the following expression;

$$S_C^2 = \sum_i^n \left(\frac{\partial f}{\partial x_i}\right)^2 u_{x_i}^2 + \sum_i^N \sum_j^N \left[\frac{1}{2}\left(\frac{\partial^2 f}{\partial x_i \partial x_j}\right)^2 + \frac{\partial f}{\partial x_i}\frac{\partial^3 f}{\partial x_i \partial x_j^2}\right] u_{x_i}^2 u_{x_j}^2 \tag{4.13}$$

The partial derivative elements of f with respect to the input quantities x_i, e.g.; $\partial f / \partial x_i$, are called *sensitivity coefficients* and describe how the behavior of the output estimate C varies with changes in x_i.

The sensitivity coefficients can also be obtained through simulations. Although the RCM is a multi-variate function it is possible to perform simulations where one of the input variables is perturbed and the others are kept constant. After many simulations, $\bar{C}$ and S_C, give an estimation of the sensitivity of the output due to changes in one of the input variables.

4.1.3 Pros and cons

The advantage of the MC method is that no assumptions/simplifications are applied to the function that is being analyzed. In the TS method, a non-linear function is *linearized* and approximated by a finite number of expansion terms. However, the major advantage of the TS method is that an analytical expression is obtained for the propagation of uncertainties, allowing more insight in the sensitivity of the function with respect to its input variable(s). The MC method simply allows for a measure of total uncertainty, say the variance. In this way, the user has no (direct) knowledge of the contribution of the individual variables to this total uncertainty, whereas with the TS method, the sensitivity components do provide that insight. The MC method has a higher accuracy because no linearization is performed, although this comes with high computational costs. Finally, the sensitivity of RCM to its input can also be analyzed if a MC is applied where 1 variable is perturbed and the others are kept constant, but this then requires many MC simulations.

4.2 Propagation methodology initialization

The TS method requires the definition of u_{x_i}. Once these are defined, they can be directly given as input to Equation 4.11. Similarly for the MC method, the term $\varepsilon_{\mathbf{x}}$ of Equation 4.5 is required.

$\varepsilon_{\mathbf{x}}$ is derived from an ECMWF meteorology prediction model, which models meteorological quantities such as pressure or the Ozone concentration. The difference between modelled and measured output is taken to be the uncertainty associated with the input variables, i.e.; $\varepsilon_{\mathbf{x}}$. For Ozone and pressure, the following uncertainty values are selected;

$$u_{O_3} = 10\,DU \tag{4.14a}$$

$$u_P = 5\,hPa \tag{4.14b}$$

The Chlorophyll-a concentration is assumed to be constant throughout an entire acquisition and thus its mean value is simply the value of itself. Its uncertainty is provided through the summation of two elements, the relative uncertainty and its standard deviation. The relative uncertainty is defined as the average of the error[3] associated with the Globcolour climatology monthly Chl-a maps;

$$u_{rel} = \frac{\sum_{y=1}^{15} \varepsilon_{Chl(m,y)}}{\sqrt{15}} \tag{4.15}$$

The standard deviation associated with the monthly climatology is computed as

$$S_{Chl} = \sqrt{\frac{\sum_{y=1}^{15} \left(Chl(m,y) - \bar{Chl}(m)\right)}{\sqrt{15}}} \tag{4.16}$$

$$\bar{Chl} = \frac{\sum_{y=1}^{15} Chl\,(m,y)}{15} \tag{4.17}$$

Recall that the denominator represents the number of years which cover the climatology data.

In this thesis, the error term will be viewed as an uncertainty, more specifically, it will be

[3] It is not clear if the monthly climatology is obtained through weighted average on pixel level or not. Beside this, it is not clear whether the relative uncertainty term comes from the averaging or from the bio-optical inversion.

viewed as the standard deviation associated with the input variables, i.e.;

$$\varepsilon_{\mathbf{x}} = u_{\mathbf{x}} = \sigma_{\mathbf{x}} \tag{4.18}$$

The randomness is guaranteed by generating a uniform distribution with values between -1 and 1, and retrieving from this distribution a value denoted by α, and to multiply this value with $\pm\sigma_x$. Following this procedure, as an update of Equation 4.5, the input parameters are perturbed as follows;

$$x = \bar{x} + \alpha\,\sigma_x \tag{4.19}$$

In the RCM, this perturbation is obtained through multiplication of the input variables with a *perturbation factor* that is defined as follows[4];

$$\begin{aligned} \mathbf{x}' &= \mathbf{x}\,F_p \\ \text{where } F_p &= 1 + \alpha\frac{\sigma_{\mathbf{x}}}{\mathbf{x}} \end{aligned} \tag{4.20}$$

4.3 Classification evaluated uncertainties

According to BIPM et al. (2008) the classification of uncertainties into random and systematic, or in Type-A and Type-B uncertainties, can be ambiguous and confusing. They indicate that a classification could be included for convenience of discussion only but that there is no difference in the nature of the uncertainties. They are both based on probability distributions and their uncertainty components are quantified by the mean and standard deviation. It is mentioned, however, that categorizing the method of uncertainty evaluation rather than the component themselves, can avoid ambiguity between the two classes of uncertainties.

4.3.1 Random & Systematic uncertainties

Random uncertainties are those uncertainties that occur due to unpredictable variations in time or space. Examples of random uncertainties can be our reaction time when a stopwatch is used to time the duration of some process or the accuracy if we read a ruler when the length of some object is measured. Generally speaking an over- or under-estimation is evenly likely in these cases (hence the term *random*) which means that after repeating the process many times, the expectation of these uncertainties, goes to zero (Taylor, 1997; BIPM et al., 2008). On the other hand, if the device that is used in the timing or measurement process has an offset in any arbitrary direction, our measurements will always have that same offset. If this offset is unknown, it is referred to as a *systematic* uncertainty. Contrary to random effects, increasing the number of measurements does not provide any insight regarding the systematic uncertainties. Figure 4.1 shows very clearly examples of how systematic and random effects can be visualized.

4.3.2 Type A & Type B uncertainties

In the scenario that the experimental standard deviation S is based on independent repeated observations on a random input quantity x_i, u_{x_i} is referred to as a ***Type A standard uncertainty***. If independent repeated observations on an input variable x_i are not possible or if the x_i is not random, u_{x_i} must be evaluated based on the following available information on the variability of x_i (BIPM et al., 2008):

[4] In DIMITRI, the mean values, i.e. $\bar{\mathbf{x}}$, are not available and thus the value itself is simply used.

FIGURE 4.1: *These four targets with different shots display random and systematic errors (Taylor, 1997). The objective is to hit the center of the target as many times as possible. The upper left and lower right are opposites. The upper right shows a case where shots are fired somewhat accurately, but they all have a constant offset. The lower left target does not display a constant offset but the scattered shots indicate large random errors.*

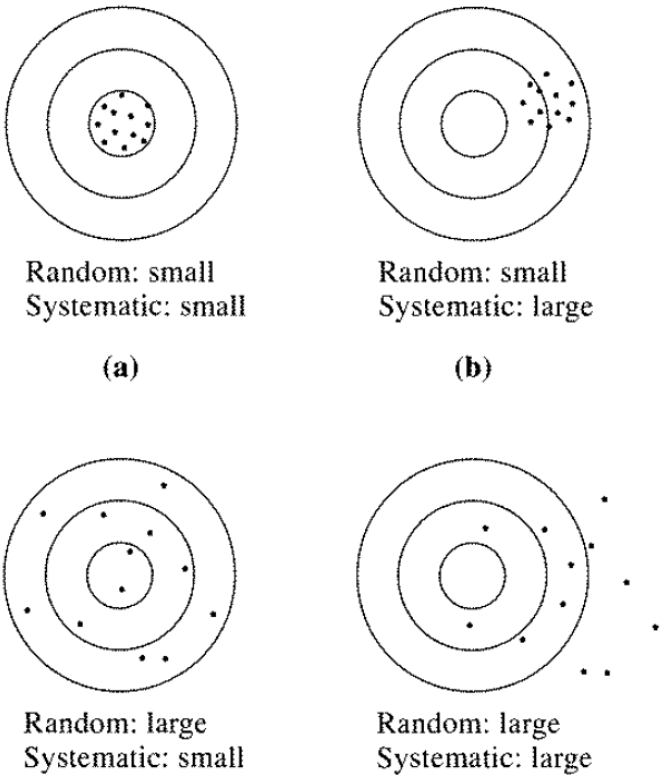

- previous measurement data;
- experience with or general knowledge of the behavior and properties of relevant materials and instruments;
- manufacturer's specifications;
- data provided in calibration and other certificates; and
- uncertainties assigned to reference data taken from handbooks.

The proper use of the available data for a Type B evaluation requires insight based on experience and general knowledge and is not necessarily less reliable as a Type A evaluation method. In the case that there are few independent repeatable observations, for example, a Type B evaluation is more reliable than a Type A one. When u_{x_i} is evaluated using any or a combination of all of the aforementioned points, it is referred to as a ***Type B standard uncertainty***.

4.3.3 Classification

It should be noted that u_{x_i} in Equation 4.11 should in fact be the standard deviation associated with the input σ_{x_i}. However, in this thesis the quantity ε_x will be viewed as the σ_{x_i} (see Equation 4.18). ε_x seems to be a Type A component as through many iterations the collective difference between modelled and measured variables ε_x are obtained. Yet the measurement

/ modelling process through which ECMWF obtains the variables and their uncertainties can also be attributed to Type B evaluation methods. The reason for this is that the instrument which measures and the model which predicts values, are both subject to biases such as instrument calibration uncertainties or model simplifications / inaccuracies. This means that it the existence of systematic uncertainties, either associated with the input value or their estimated uncertainties, is very likely.

Using the HPLC, FL3000 and CTD sensor, Morel and Maritorena (2001) determined a Chl-a profile, converted from an algal fluorescence profile using 12 discrete HPLC data points in Case-1 waters. Although the number of discrete data points measured is given, no information is provided on the measurement frequency. Furthermore, the performance of FL3000, which measures the continuous algal fluorescence profile, is not given and neither are the conversion details which result in the continuous Chl profile (see Figure 2.8). The application of the HPLC implies that the Chl-a is measured through observations, though 12 data points seems on the low side compared to the expected number of observations for the ECMWF input variables. On the other hand, the conversion from the fluorescence to the Chl-a profile seems to require some form of relation between Chl and its corresponding fluorescence, which may be established through previous measurement data. It appears that the determination of the Chl-a input quantity, as described by Morel and Maritorena (2001), includes both evaluation methods, i.e. Type A *and* Type B. The Globcolour climatology database is coalesced from satellite data and the distribution associated with it is based on a large numbers of observations, classifying it as a Type A evaluation. Yet, the use of a non-linear fitting method and the bio-optical inversion model to retrieve global Chlorophyll-a values also seems to indicate that systematic uncertainties cannot be avoided. Therefore, data that is obtained from the Globcolour database can also be attributed to the Type B evaluation method.

Recall that the inversion model also provides uncertainty estimates (see Equation 4.15 and Equation 4.16). However, the error associated with the Globcolour climatology monthly Chl-a maps $\varepsilon_{Chl}(m, y)$, is not defined in this thesis because its origins could not be established. Moreover, the least-squares minimization function that is used for the match-up analysis estimates the following uncertainties;

1. uncertainty associated with the normalized water-leaving radiance, L_{w_N}, per sensor band, denoted as σ_{sensor}.
2. uncertainty due to the bio-optical inversion model per sensor band, denoted as σ_{GSM}
3. uncertainty associated with the difference between $L_{w_{sensor}}$ and $L_{w_{GSM}}$, denoted as, $\sigma_{product}$.

Maritorena et al. (2010) emphasize that systematic uncertainties may be present that are not taken into account during the uncertainty estimation of the match-up analysis. This means that any of these listed uncertainties may influence the accuracy of the Chl-a input variable and its estimated uncertainty.

4.4 Conclusion

In this chapter uncertainty classification theory has been addressed for the purpose of distinguishing different types of uncertainties associated with the input variables that are used in the RCM. In order to avoid ambiguity and confusion, the evaluation method of the input variables was attempted to be classified. What becomes clear when reviewing the evaluation

methods, or when looking at the flowchart at page 32, is that there are many assumptions and simplifications that have been made in order to obtain the meteorological input variables, similarly for the Chl-a variable. This makes the classification of uncertainties associated with the input variables, or the classification of their evaluation methods, very difficult. It became clear that the evaluation method of the input variables could be attributed to both types of uncertainties. In fact, there is no reason why the uncertainties associated with these input variables, are any different. It is painfully apparent that at this point, it is not straight forward to conclusively classify any of the input variables or their estimated uncertainties. A retrospect will be given with respect to the evaluated uncertainties at the end of the next chapter.

At this point all necessary theories are addressed and the uncertainty analysis and propagation can begin. The approach will be to propagate the previously defined uncertainties and then to perform an analysis on the results. It will be very efficient if the TS method proves to be an appropriate propagation method because it only requires 1 run to produce the uncertainties. The MC method will be used to validate whether the uncertainties are sufficiently accurate. The criteria for this requires the TS uncertainties to deviate less than 1% compared to MC uncertainties.

It becomes obvious that a very complex expression will be obtained when all relevant terms are substituted in Equation 2.63 . For this reason it is suggested to introduce simplifications to allow for a less complex expression to be obtained. The TS method can then be applied to this simpler model. The simplifications that are introduced and the validation of its accuracy are addressed in the next chapter.

Chapter 5

Modified Model

The objective of this chapter is to introduce simplifications to the RCM reflectance model such that a TS uncertainty propagation method can be applied without too much complexity. This simplified model is called the Modified Model (MM) and is described in section 5.1. The MM configuration will be validated with the unmodified reflectance model (UM) using a data analysis in section 5.2. The criteria for this validation is that the calibration coefficients obtained with the MM configuration should deviate no more than 5% from the calibration coefficients obtained in the UM configuration. In order to better understand the RCM and its dependence on its input variables a sensitivity analysis is performed in section 5.3. Finally, an uncertainty analysis is performed in section 5.4 to assess whether the propagated uncertainties of MM approximate those obtained from the UM configuration with a deviation of less than 1%.

5.1 Model description

There are 2 modifications applied to Equation 2.63 and these regard ρ_a and ρ_w. The most significant modification applied to the UM configuration is that MM assumes an aerosol-free atmosphere which reduces Equation 2.63 to the following;

$$\rho^{TOA} = t_{gas}\ (\rho_R + t_{down}\, t_{up}\, \rho_w) \tag{5.1}$$

where ρ_{path} is replaced by only ρ_R, as is defined in Equation 2.25. If multiple scattering is ignored, no reflective surface is present and one is dealing with a *homogeneous atmosphere*, which is defined to be an atmosphere where the scattering phase matrix and single scattering albedo are independent of the optical depth, ρ_R can be obtained through the following equation (De Haan, Bosma, and Hovenier, 1987);

$$\mathbf{R}\left(\mu_d, \mu_u, \Delta\phi\right) = \frac{a}{4\left(\mu_d + \mu_u\right)}\left(1 - e^{-b/\mu_d - b/\mu_u}\right) \times \mathbf{Z}\left(-\mu_d, \mu_u, \Delta\phi\right) \tag{5.2}$$

$\mathbf{R}$, in an aerosol-free atmosphere, is ρ_R, a is the single scattering albedo, μ_d and μ_u are the cosine of the zenith angles in the downward (θ_s) and upward (θ_v) direction respectively, b is the Rayleigh optical thickness (τ_R) and finally $\mathbf{Z}$ is the scattering phase matrix. If the sensor bands coincide with an absorption band, the single scattering albedo is equal to 1. The phase matrix is taken from Hansen and Travis (1974), where only the first element of the matrix is taken because polarization is ignored;

$$\mathbf{Z} = \diamond\left\{\frac{3}{4}\left(1 + \cos^2\alpha\right)\right\} + (1 - \diamond)\left\{1\right\} \tag{5.3}$$

where $\diamond = (1 - \delta)\,/\,(1 + \delta/2)$. Recall that δ is the depolarization factor and is quantified to be 0.029 (Young, 1981). α is the *scattering angle*, which is the angle between the propagation path of light and the reflected path towards the sensor. When θ_s and θ_v are both smaller than $90°$, the scattering angle can be determined from the sum of these two. Consequentially, ρ_R is

calculated as follows;

$$\rho_R = \frac{a}{4\left(\mu_d + \mu_u\right)}\left(1 - e^{-b/\mu_d - b/\mu_u}\right) \cdot \left(\diamond\frac{3}{4}\left(1 + \cos^2\alpha\right) + (1 - \diamond)\right) \tag{5.4}$$

The pressure correction that was applied to ρ_{path} (see Equation 2.27) will in stead be applied to ρ_R, resulting in an explicit dependence on the pressure. Note that η is a function of τ_a (see Equation 2.28) but for the MM configuration it is assumed that $\tau_a \to 0$ thus;

$$\lim_{\tau_a \to 0}\ (\eta) = \lim_{\tau_a \to 0}\left(\frac{\tau_R}{\tau_R + \tau_a}\right) = 1 \tag{5.5}$$

Then the pressure correction is applied as follows;

$$\lim_{\tau_a \to 0}\ (\rho_{R,\,P}) = \lim_{\tau_a \to 0}\left(\rho_{R,\,P_s}\left(1 + \frac{P - P_s}{P_s}\eta\right)\right) = \rho_{R,\,P_s}\left(1 + \frac{P - P_s}{P_s}\right) \tag{5.6}$$

Another effect of ignoring the aerosol scattering regards the transmittance as seen in Equation 2.38. Recall that the total transmittance consists out of aerosol and Rayleigh transmittance. The latter is denoted by t_R which is defined as;

$$(t_{d,\,P}\, t_{u,\,P}) = t_{R,\,P} = e^{-\frac{1}{2}\tau_R\, M\,(1 + \Delta P/P_s)} \tag{5.7}$$

The last element that must be addressed is the simplification that is applied to the calculation of irradiance reflectance R_0. It is assumed that the iterative procedure which determines this parameter (see Equation 2.48) can be replaced by a single evaluation in the simplified model, that is, only by evaluating Equation 2.48b.

5.2 Data analysis

The previously introduced modifications applied to the UM configuration have an effect on C values that are obtained with the MM configuration (conveniently denoted C_{UM} & C_{MM}). Here a data analysis is performed and particular attention is given to assess whether C_{MM} sufficiently approximates C_{UM}. 4 physical quantities will be examined using data analysis; the ρ_R, ρ_{path}, ρ_w and also t.

However, before commencing with the data analysis, the relation between the number of simulations in the MC method versus the accuracy of obtained results will be quantified. Recall that due to (among others) the finite number of simulations, the mean of C and its associated standard deviation, $\bar{C}$ and S_C respectively, exhibit a deviation with the true mean (μ_C) and standard deviation (σ_C).

In Table 5.1 two cases of $\bar{C}_{MM}$ and $S_{C_{MM}}$ are shown to illustrate that by increasing the number of simulations the approximation of these central moments improves[1]. The two cases correspond with a MoE of 10% (equivalent to 100 iterations) and 1% (equivalent to 10000 iterations). From $\varepsilon_{\bar{C}}$ and ε_{S_C} values it becomes obvious that by choosing 100 iterations results in a loss of accuracy of only 0.056% for $\bar{C}_{MM}$ and 0.074% for S_C. From these results it can

[1]Note that input perturbations are taken into account as defined in Equation 4.14. For Chl-a the value for the total uncertainty is 0.0154 $mg\,m^{-3}$, which is obtained from the Chl-a climatology of the South Indian Ocean at January.

TABLE 5.1: *The mean and standard deviation of the calibration coefficient ($\bar{C}$, S_C) computed with the MM configuration, for 100 (MoE:10%) and 10000 (MoE:1%) iterations respectively. ε gives the loss when 100 iterations are performed in stead of 10000.*

λ	412	443	490	510	560	620	665
$\bar{C}_{MoE:10\%}$	1.10480	1.11532	1.09425	1.07452	1.05879	1.05553	1.06597
$\bar{C}_{MoE:1\%}$	1.10541	1.11588	1.09447	1.07458	1.05877	1.05556	1.06602
$\varepsilon_{\bar{C}}$	-0.0555%	-0.0507%	-0.0207%	-0.0048%	0.0017%	-0.0035%	-0.0052%
$S_{C_{MoE:10\%}}$	1.3968%	1.2762%	0.4867%	0.2641%	0.3809%	0.3259%	0.3042%
$S_{C_{MoE:1\%}}$	1.3232%	1.2067%	0.4434%	0.2681%	0.3965%	0.3322%	0.3087%
ε_{S_C}	0.0736%	0.0695%	0.0433%	-0.0040%	-0.0156%	-0.0063%	-0.0045%

be concluded that a MC simulation with only 100 iterations is sufficient and thus the general setting for the data analysis of C_{UM} and C_{MM} will be performed with a MoE of 10%.

5.2.1 Rayleigh reflectance

The data analysis is started by looking at ρ_R obtained from the UM and MM configurations. The comparison between UM and MM is made by comparing the *relative* deviation (in percentages) of MM values compared with UM values. The results (obtained for a Chl-a value of $0.035\,mg\,m^{-3}$) are presented in Table 5.2 for the first and last optical sensor band, i.e.; at 412 and 665 nm. Let us review why ρ_R is significantly under-represented in the MM configuration at short λ and slightly over-represented at long λ and consequentially, how this deviation distorts other parameters.

TABLE 5.2: *Validation of the MM configuration versus the UM configuration - ρ_R parameter.*

		$\boldsymbol{\rho_R}$	$\boldsymbol{\rho_{path_p}}$	$\boldsymbol{\rho_{sim}^{TOA}}$	$\boldsymbol{C}$
412	UM	0.14027	0.14206	0.17770	1.05496
	MM	0.10194	0.10224	0.13031	1.43864
	ε[%]	-27.32375	-28.03420	-26.66994	**36.36915**
665	UM	0.02008	0.02146	0.02178	1.04640
	MM	0.02033	0.02039	0.02076	1.09775
	ε[%]	1.27435	-4.99829	-4.67747	**4.90730**

Scattering, and thus also multiple scattering, occurs more frequently at shorter λ, rather than at longer λ (see Equation 2.22), which is also the case for ρ_R. The deviation in ρ_R between UM and MM comes from the application of Equation 5.2, as it attempts to estimate the *single* scattering ρ_R at short λ, whereas single scattering occurs more frequently at long λ. By excluding multiple scattering for the estimation of ρ_R, which is effectively done by approximating the ρ_R through Equation 5.2, much less reflectance is taken into account and thus the under-representation of ρ_R with MM can be explained. Equation 5.2 would be better suited to approximate the single scattering ρ_R at long λ because single scattering occurs more frequently. This explains why the deviation drops significantly to 1.3% at 665 nm.

One further assumption is that there is no reflective surface, which means that only reflectance by the atmosphere is taken into account. In other words, all light that hits the surface is absorbed.This assumption directly contradicts the theoretical premise on which the reflectance model incorporated in RCM is based, where e.g. ρ_w are used to determine ρ_{sim}^{TOA}.

The deviations in ρ_R propagate to ρ_{path_p}, ρ_{sim}^{TOA} and C_{MM}. Without addressing any of the other parameters, it is evident from the maximum deviation for C_{MM} at 412 nm, that further improvements are needed to the MM configuration in order to sufficiently (i.e., within 5%) approximate C_{UM}. Noticing that at long λ a more accurate approximation of ρ_R can be obtained, as is seen from the approximation at 665 nm, it is proposed to use Equation 5.2 to compute ρ_R at 865 nm and to propagate this value to lower sensor bands using the following *scaling factor*:

$$\rho_R = \rho_R^{865} \left(\frac{865}{\lambda} \right)^4 \tag{5.8}$$

The results of applying this scaling factor to the MM configuration are shown in Table 5.3.

TABLE 5.3: *Validation of the MM configuration versus the UM configuration - with revised ρ_R values using Equation 5.8.*

		$\boldsymbol{\rho_R}$	$\boldsymbol{\rho_{path_p}}$	$\boldsymbol{\rho_{sim}^{TOA}}$	$\boldsymbol{C}$
412	UM	0.14027	0.14206	0.17770	1.05496
	MM	0.14210	0.14252	0.17059	1.09893
	ε[%]	1.31019	0.31983	-4.00165	**4.16793**
665	UM	0.02008	0.02146	0.02178	1.04640
	MM	0.02094	0.02100	0.02137	1.06658
	ε[%]	4.28734	-2.17192	-1.89214	**1.92852**

Due to improvements in ρ_R all other parameters are also improved. What is noticeable is that the deviations between MM and UM *increase* with increasing λ. The improvement in ρ_{path_p} due to improvements in ρ_R result in a significant improvement of C_{MM}, some 32% at short λ and 4% at long λ. This provides support for the conclusion that due to the application of a scaling factor to ρ_R, C_{MM} approximates C_{UM} with sufficient accuracy.

5.2.2 Atmospheric path reflectance

The second parameter that is analyzed is ρ_{path}, starting with the UM configuration[2]. The results are seen in Table 5.4. All parameters required to calculate ρ_{path_p} have also been included.

TABLE 5.4: *Generated results acquired with the UM configuration where the perturbed input parameters are taken into account.*

λ	412	443	490	510	560	620	665
τ_R	0.316853	0.234807	0.155151	0.131711	0.089911	0.059433	0.044729
τ_a	0.025305	0.024293	0.022740	0.022187	0.020941	0.019656	0.018819
ρ_R	0.140267	0.106241	0.070477	0.059960	0.040822	0.026752	0.020076
XC	1.010157	1.013845	1.021398	1.024140	1.035001	1.051487	1.067347
ρ_{path}	0.141692	0.107712	0.071986	0.061407	0.042251	0.028129	0.021428
ρ_{path_p}	0.141866	0.107842	0.072069	0.061477	0.042296	0.028157	0.021448

It can be noticed that ρ_{path_p} decreases for increasing λ. Note that ρ_{path_p} consists of ρ_R and ρ_a. Molecular scattering decreases significantly with increasing λ, the reason for this can

[2]The same configuration is used for the input variables and their uncertainties as in the previous section.

be explained through the quantification of the scattering cross section (see Equation 2.20a), which states that the scattering cross section is inversely related to λ^4. τ_a reduces as well, however, much less rapidly than ρ_R. The combination of these two causes ρ_{path_p} to reduce almost as rapid as ρ_R reduces, which seems to indicate that reductions in ρ_R drive the reduction in ρ_{path_p}.

In the MM configuration the atmosphere is assumed to be free of aerosols, which makes it is interesting to analyze the effect of setting τ_a to zero and investigate how that influences ρ_{path_p}. The results of this step have been shown in Table 5.5. The reverse case, where τ_a is selected to have the maximum value is also interesting and these results are shown in Table 5.6[3].

TABLE 5.5: ρ_{path_p} *obtained from the UM configuration where* ***minimum*** τ_a *values are selected.*

λ	412	443	490	510	560	620	665
τ_R	0.316853	0.234807	0.155151	0.131711	0.089911	0.059433	0.044729
τ_a	**0**	**0**	**0**	**0**	**0**	**0**	**0**
ρ_R	0.140267	0.106241	0.070477	0.059960	0.040822	0.026752	0.020076
XC	1.000000	1.000000	1.000000	1.000000	1.000000	1.000000	1.000000
ρ_{path}	0.140267	0.106241	0.070477	0.059960	0.040822	0.026752	0.020076
ρ_{path_p}	0.140454	0.106382	0.070571	0.060040	0.040876	0.026788	0.020103

TABLE 5.6: ρ_{path_p} *obtained from the UM configuration where* ***maximum*** τ_a *values are selected.*

λ	412	443	490	510	560	620	665
τ_R	0.316853	0.234807	0.155151	0.131711	0.089911	0.059433	0.044729
τ_a	**0.870104**	**0.860359**	**0.845263**	**0.839872**	**0.827839**	**0.816024**	**0.808833**
ρ_R	0.140267	0.106241	0.070477	0.059960	0.040822	0.026752	0.020076
XC	1.345841	1.478144	1.750450	1.899188	2.332921	3.089391	3.791675
ρ_{path}	0.188778	0.157040	0.123367	0.113875	0.095234	0.082647	0.076122
ρ_{path_p}	0.188845	0.157084	0.123393	0.113896	0.095247	0.082655	0.076127

Comparing the results from these two tables with results in Table 5.4 indicates that ρ_{path_p} are lower when $\tau_a = 0$ and higher when the maximum τ_a values are chosen. Antoine and Morel (1998) have performed an analysis on the dependence of ρ_{path} on τ_a. They have shown that ρ_{path} increases approximately linearly with τ_a, where at long λ the rate of increase with τ_a is slightly lower than at short λ (because ρ_a is larger at short λ). This analysis was performed under viewing conditions where $\theta_s = 40°$, $\theta_v = 30°$, $\Delta\phi = 90°$. Even though the UM configuration utilizes different viewing conditions, Antoine and Morel explain that due to the weak anisotropy of the Rayleigh scattering phase function, the ρ_R and $\rho_{R,a}$ multiple scattering are not strongly dependent on varying θ_s and θ_v. What can be concluded is that the results generated by the UM configurations are consistent with the theory and expectations.

[3] I want to briefly address how the value for τ_a is adjusted to the minimum or maximum value. Recall that the NIR band at 865 nm is used to extract information regarding τ_a (basis for the two-band method). In atmospheric physics, τ_a at 550 nm is used as a reference. In MYSTIC, 7 reference values for τ_a^{550} are defined (see Table 2.4) and these are propagated to other sensor bands, yielding 7 values for τ_a^{412} and other bands. In RCM, τ_a^{865} (which is obtained from Equation 2.26) is propagated to shorter bands using weighted linear interpolation between any of the two reference values within which τ_a^{865} is contained, for a particular λ. For minimum τ_a^{λ} values, the interpolation is simply avoided by assuming that τ_a^{λ} is equal zero. Reversely, for maximum τ_a^{λ} values, the propagated τ_a^{550} for its max reference value is selected.

For the MM configuration we observe that ρ_{path_p} in Table 5.7 yields higher values than those in Table 5.4. Note that this should not be the case because in the MM configuration an aerosol-free atmosphere is assumed, and as previously established, this would yield lower ρ_{path_p} results. This phenomena can be explained due to the approximations of ρ_R using Equation 5.8 which over-estimates ρ_R. In order to assess how well MM approximates UM, ρ_R values in MM have been replaced with ρ_R values of UM, and the results of the new ρ_{path_p} values are tabulated in Table 5.8.

TABLE 5.7: ρ_{path_p} *values obtained with the MM configuration with scaled* ρ_R *values.*

λ	412	443	490	510	560	620	665
τ_{ray}	0.316853	0.234807	0.155151	0.131711	0.089911	0.059433	0.044729
τ_{aer}	-	-	-	-	-	-	-
ρ_{ray}	0.142105	0.106312	0.071025	0.060522	0.041634	0.027710	0.020937
XC	-	-	-	-	-	-	-
ρ_{path}	-	-	-	-	-	-	-
ρ_{path_p}	0.142293	0.106453	0.071120	0.060603	0.041689	0.027746	0.020965

TABLE 5.8: ρ_{path_p} *values obtained with the MM configuratio, where* ρ_R *values of the UM configuration are used instead of using those acquired through Equation 5.8.*

λ	412	443	490	510	560	620	665
τ_{ray}	0.316853	0.234807	0.155151	0.131711	0.089911	0.059433	0.044729
τ_{aer}	-	-	-	-	-	-	-
ρ_{ray}	0.140267	0.106241	0.070477	0.059960	0.040822	0.026752	0.020076
XC	-	-	-	-	-	-	-
ρ_{path}	-	-	-	-	-	-	-
ρ_{path_p}	0.140454	0.106382	0.070571	0.060040	0.040876	0.026788	0.020103

The revised ρ_{path_p} values with the MM configuration are identical to those obtained from the UM configuration where τ_a is zero (see Table 5.5). This result is what you would expect, given the aerosol-free atmosphere assumption is made for the MM configuration. In conclusion, the higher values for ρ_{path_p} in MM are due to an over-estimation of ρ_R through the scaling factor approximation.

5.2.3 Water-leaving reflectance

Now the ρ_w parameter can be analyzed and its values as a function of λ are found in Table 5.9. What becomes visible is that ρ_w reduces with increasing λ. Let us decompose why this is the case by reviewing every element that ρ_w depends on. For convenience, they have been listed in Table 5.10 as a function of λ.

TABLE 5.9: ρ_w *results acquired with the UM configuration.*

λ	412	443	490	510	560	620	665
ρ_w	0.040691	0.030824	0.018235	0.009278	0.003988	0.000702	0.000376

ρ_w depends on 4 elements (see Equation 2.48) out of which 1 is constant (i.e. f).

Starting with the total backscattering b_b, which reduces with increasing λ because the backscattering for optically pure water, b_w, and the particulate backscattering coefficient, b_{bp}, reduce with increasing λ. The diffuse attenuation for downwelling irradiance, k_d, increases with increasing λ because the attenuation coefficient for pure water, k_w, increases for increasing λ. The attenuation coefficient for biogenic components, k_{bio}, is highest for short λ and decreases with increasing λ, and increases again at long λ. However, the contribution of k_{bio} is smaller than the contribution of k_w, which is why k_d increases with λ somewhat similarly as how k_w increases. Because the absorption coefficient for optically pure water, a_w, as opposed to b_w, increases with increasing λ. Therefore, eventually, the reason why k_d increases is due to the increase in a_w and the reduction in b_b.

Finally, the last element that ρ_w depends on is the element U, which on its own depends on the reflectance R_0, and some constants. R_0 (see Equation 2.48b) depends on the ratio of b_b to the product of k_d and U. So, it was established that the numerator decreases and the denominator, as a consequence of the product of k_d and U, increases. This results in a rapid decrease of R_0 and consequentially, a rapid decrease of ρ_w.

TABLE 5.10: *Dependent variables of ρ_w as a function of λ.*

λ	412	443	490	510	560	620	665
b_{bp}	0.000533	0.000508	0.000475	0.000463	0.000436	0.000409	0.000392
b_w	0.006650	0.004872	0.003165	0.002667	0.001789	0.001160	0.000861
b_b	0.003858	0.002944	0.002058	0.001797	0.001331	0.000989	0.000822
k_w	0.007876	0.009505	0.016582	0.033834	0.062795	0.276080	0.429430
k_{bio}	0.017820	0.014654	0.009436	0.007833	0.005883	0.005773	0.006433
k_d	0.025696	0.024160	0.026019	0.041667	0.068678	0.281853	0.435863
a_w	0.004551	0.007069	0.015000	0.032500	0.061900	0.275500	0.429000
χ	0.122858	0.107212	0.072420	0.059430	0.039000	0.038500	0.049000
e	0.653270	0.673358	0.689550	0.685670	0.640000	0.642000	0.687000
μ_d	0.800418	0.818162	0.840598	0.856633	0.868410	0.876208	0.877833
U_1	0.75	0.75	0.75	0.75	0.75	0.75	0.75
U_2	0.660268	0.697774	0.756058	0.807561	0.845353	0.871906	0.875509
U_3	0.643708	0.689713	0.756690	0.810932	0.847912	0.872506	0.875842
R_{o_1}	0.066057	0.053616	0.034798	0.018975	0.008528	0.001544	0.000830
R_{o_2}	0.075034	0.057629	0.034519	0.017623	0.007566	0.001328	0.000711
R_{o_3}	0.076965	0.058302	0.034490	0.017550	0.007543	0.001327	0.000711

It should be noted that, in the UM configuration, R_0 and U are iteratively evaluated and obtain convergent results after three iterations. Furthermore, it should be noted that the successive values of R_0 are higher than their predecessors for s $\lambda \leq 443\,nm$ but lower than their predecessors for $\lambda > 443\,nm$. For U the opposition holds, its value decreases with each iteration for $\lambda < 490\,nm$ and increases for $\lambda > 443\,nm$. U also increases with λ.

Now, in the MM configuration, it is assumed that ρ_w can be evaluated with the first iteration of R_0 and U only. This causes an under-estimation of ρ_w at short λ and an over-estimation at long λ (see Table 5.11), precisely following the R_{0_1} values compared to R_{0_3} values.

The smaller the chlorophyll-a concentration, the more significant the difference between the UM and MM configuration at $\lambda \leq 443\,nm$. At longer λ there is no significant variability of the deviation between the UM and MM configuration as a function of λ. This effect has been

TABLE 5.11: ρ_w *results acquired with the MM configuration.*

λ	412	443	490	510	560	620	665
ρ_w	0.034924	0.028347	0.018398	0.010032	0.004509	0.000816	0.000439

illustrated in Figure 5.1 and here the under-estimation at short λ and the over-estimation at long λ is clearly visible.

FIGURE 5.1: *The relative difference of ρ_w as obtained from the UM and MM configurations for various Chl-a concentrations, as a function of λ.*

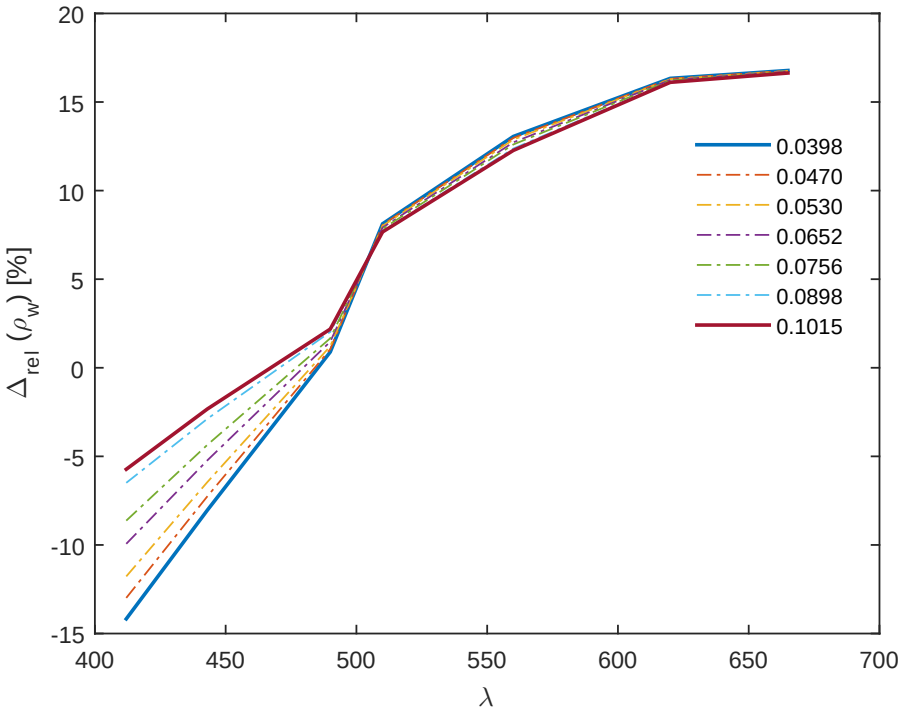

5.2.4 Transmittance

Here the last parameter is analyzed, namely the total transmittance, t_t and its values as a function of λ in the UM configuration are preseted in Table 5.12. What is immediately noticeable is that t_t increases as λ increases. This is because as λ increases, τ_a decreases. Note that t_t is the ratio of outgoing intensity to incoming intensity. The more aerosols present in the atmosphere, the higher the likelihood that intensity becomes extinct, either due to absorption or scattering, and thus reducing the outgoing intensity. This explains the reduction of t_t as a function of increasing τ_a and thus also (by default) with decreasing λ.

In DIMITRI, another LUT is available that stores the downward and upward transmittance values corresponding with the 7 reference values associated with τ_{aer}^{550}. Additionally, these values are simulated for different values of the viewing zenith angle θ_v. t_t is dependent on the angle of light that is observed because of the relation between the propagation path and θ_v. The longer the propagation path, the more likely it is that extinction occurs. So, t_t under an angle close to zero yields the highest values and as θ_v grows towards $90°$, t_t will reduce to its minimum value, which can be less than half its value under $\theta_v = 0$ (see Table 5.13).

TABLE 5.12: *Generated results acquired with the UM configuration.*

λ	412	443	490	510	560	620	665
τ_{aer}	0.025305	0.024293	0.022740	0.022187	0.020941	0.019656	0.018819
t_t	0.724915	0.782516	0.846640	0.866819	0.904414	0.933647	0.948156
t_{t_p}	0.724569	0.782239	0.846441	0.866647	0.904291	0.933563	0.948092

TABLE 5.13: *The dependence of downward transmittance on θ_v, for values at 412 nm.*

θ_v	0	10.2229	21.348	32.479	43.6114	54.7444	65.8776	77.011	85
t_t	0.871934	0.870237	0.863174	0.850211	0.828651	0.792048	0.728573	0.604227	0.447029

So, in a similar way to the ρ_{path_p}, t_t is analyzed under minimum and maximum τ_a^{550} values. There are two ways available to to analyze this; 1) simply choose the minimum and maximum τ_a value as was done with ρ_{path_p} or 2) choose simulated t_t (obtained through MYSTIC) values that correspond with the minimum and maximum τ_a value. Both cases should yield the same results, and they have been shown in Table 5.14 and Table 5.15.

TABLE 5.14: *t_t values obtained with the UM configurations - τ_a is set to its minimum and maximum value.*

λ	412	443	490	510	560	620	665
τ_a	**0**	**0**	**0**	**0**	**0**	**0**	**0**
t_t	0.732005	0.789649	0.853747	0.873802	0.911438	0.940159	0.954579
t_{t_p}	0.731655	0.789370	0.853547	0.873628	0.911314	0.940075	0.954514
τ_a	**0.870104**	**0.860359**	**0.845263**	**0.839872**	**0.827839**	**0.816024**	**0.808833**
t_t	0.639535	0.691319	0.749569	0.769579	0.803843	0.830580	0.842721
t_{t_p}	0.639229	0.691074	0.749394	0.769426	0.803734	0.830506	0.842665

TABLE 5.15: *t_t values obtained with the UM configuration - τ_a is not modified but in stead t_t values are extracted from the LUT that correspond with the minimum and maximum τ_a values.*

λ	412	443	490	510	560	620	665
τ_a	0.025305	0.024293	0.022740	0.022187	0.020941	0.019656	0.018819
t_t ($\tau_a = 0$)	0.732005	0.789649	0.853747	0.873802	0.911438	0.940159	0.954579
t_{t_p} ($\tau_a = 0$)	0.731655	0.789370	0.853547	0.873628	0.911314	0.940075	0.954514
t_t (τ_a =max)	0.639535	0.691319	0.749569	0.769579	0.803843	0.830580	0.842721
t_{t_p} (τ_a =max)	0.639229	0.691074	0.749394	0.769426	0.803734	0.830506	0.842665

The results from these two tables are indeed identical for the scenario when $\tau_a = 0$ and when τ_a =max. In addition, from the results where a minimum τ_a is selected, t_t values are higher than for the nominal case, which is exactly as expected (compared with values in Table 5.12). Reversely, for maximum τ_a, t_t values are lower than the nominal values. In conclusion, it has been established that t_t in the UM configuration generates results consistent with the theory for high τ_a low t_t values are obtained and vice versa. The dependence of t_t on θ_v has also been explained

Moving on with t_t values acquired in the MM configuration (see Table 5.16), it can be reported that the values are lower compared to those in Table 5.12.

TABLE 5.16: t_t values obtained with the MM configuration.

λ	412	443	490	510	560	620	665
τ_a	-	-	-	-	-	-	-
t_t	0.697620	0.765795	0.838351	0.860984	0.902870	0.934690	0.950439
t_{t_p}	0.697287	0.765524	0.838155	0.860813	0.902747	0.934606	0.950375

This indicates that the approximation of t_t in the UM configuration yields in an under-representation. It would be expected to have higher t_t values in an aerosol-free atmosphere. Let's review why this is not the case for the MM configuration.

Interestingly, for the scenario where in the UM configuration t_t values associated with a minimum τ_a value (which is zero) are extracted, those t_t values are equal to the Rayleigh transmittance, t_R. This means that t_R acquired from the UM configuration can be compared with t_R acquired with the MM configuration. If this comparison is made, we find that the under-representation of t_R acquired from the MM configuration amounts to approximately 5% at short λ and a tenth of this at long λ. The reason for this is that in the UM configuration, t_R values account for both diffuse and direct transmittance, the MM configuration, where t_R is computed using Equation 5.7, only accounts for direct transmittance. Of course, neglecting diffuse transmittance is the cause for this under-representation. Also, the reason why at long λ the approximation is much better is because the approximation of single scattering is much better at long λ, given that multiple scattering decreases with $\sim \lambda^{-4}$. It is also interesting to note that the under-representation of t_t in the MM configuration is almost as low as the under-representation of t_R.

What has been established is that the Rayleigh contribution to t_t, quantified by Equation 5.7, yields an under-representation of t_R when it is acquired through MYSTIC simulations because it does not account for diffuse transmittance. Now that the entire data analysis has been performed, it can be concluded that the MM configuration 'armed' with the scaling factor approximation of ρ_R provides C_{MM} values that sufficiently approximate C_{UM}.

5.3 Sensitivity analysis

The sensitivity of the RCM on the input variables using the MC method, in the MM configuration, has been illustrated in Figure 5.2. The legend in the figure shows which variable or variables are perturbed. Let us review the relative deviations from the case where no perturbations are applied to the input values.

There are two categories, one where the input variables are individually observed and one where they are observed in combination with another input variable. From Figure 5.2 it becomes clear that once input perturbations are introduced deviations occur between C_{MM} and $\bar{C}_{MM}$. Even more obvious is that these deviations can largely be attributed to Chl-a, individually or in combination with the other two parameters. Perturbations in O_3 seem to almost have no effect, except for a very slight increase at medium-long λ. The purple dashed line reaches a maximum (though negative) deviation at 620 nm and then reduces again. Perturbations in P result in a somewhat constant deviation with λ. The Chl-a perturbations are most active at short wavelengths ($\lambda < 510\,nm$) and levels off at a slightly positive deviation. This is not surprising as from Figure 5.1 we deduce that Chl-a is mostly active at short wavelengths.

It can be concluded that at short λ, the RCM is most sensitive to changes in the Chl-a input. It should be reiterated that the perturbation in Chl-a is approximately 39% while for O_3 and P it is only 3.3% and 0.5% respectively.

FIGURE 5.2: *Relative deviation of the Rayleigh calibration coefficients when input perturbations are applied in comparison with the 'no-error' case. The legend indicates which variable(s) is perturbed in the MC configuration.*

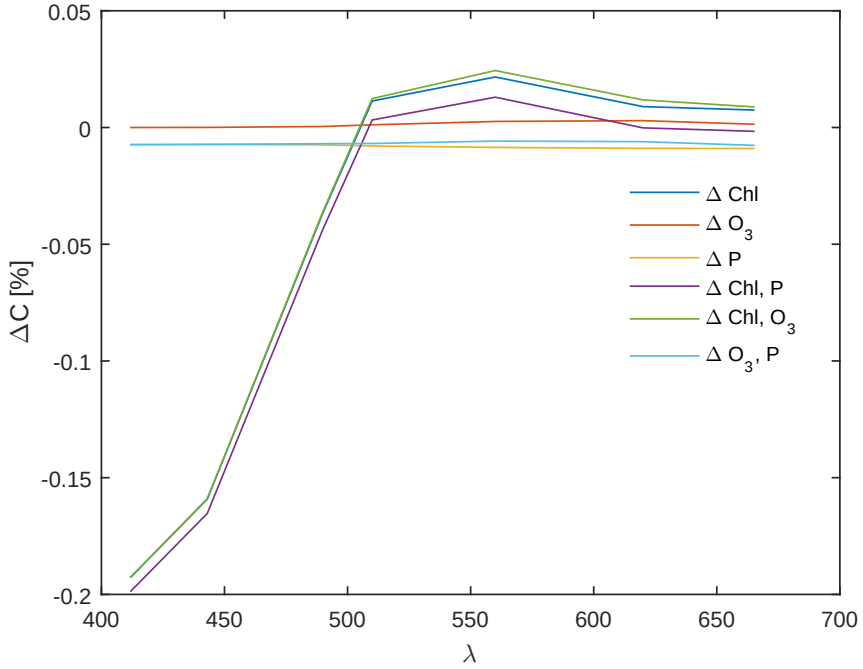

5.4 Uncertainty analysis

Before moving on with the uncertainty propagation and analysis, it should be noted that the input variable v_w, which is used in the calculation of the ρ_R, ρ_{path_p} and t_t, will not be a part of the equations for the analytical uncertainty propagation. In the MM configuration no LUTs are used and in combination with the previous assumptions, the dependency on v_w drops out and thus is no longer a part of the analysis.

In this section the MC method is first addressed in subsection 5.4.1 and then the analytical uncertainty propagation section is discussed in subsection 5.4.2.

5.4.1 MC procedure output

The results of the MC propagation method can best be described through statistical characteristics of the output values. The distribution of the output is described by the mean ($\bar{C}$) and the standard deviation (S_C).

For each configuration, RCM is run once where perturbed input parameters are not taken into account and this run yields C_{UM} and C_{MM}. The RCM is also run where input variables are perturbed and these yield $\bar{C}_{UM}$ and $\bar{C}_{MM}$. The results are displayed in Table 5.17. In the uncertainty analysis C_{UM} and C_{MM} values are viewed as the *true* values which will be compared with $\bar{C}_{UM}$ and $\bar{C}_{MM}$, respectively. A deviation from this true value, then, can be viewed as an error, which is denoted by β_C.

The approximation of the UM configuration by the MM configuration, is quantified by ΔC and $\Delta \bar{C}$. What can be seen is that the relative difference between C and $\bar{C}$ values is within 5%, which we had previously defined as the benchmark for a sufficient approximation. Recall that for the uncertainty corresponding with $\bar{C}$ values, which is quantified by S_C, the requirement was to approximate it within 1%, which as can be seen in Table 5.17, has been accomplished.

TABLE 5.17: *C_{UM} and C_{MM} coefficients generated by the RCM for the UM and MM configuration.*

λ	C_{UM}	$\bar{C}_{UM}$	$\beta_{C_{UM}}$	$S_{C_{UM}}$
412	1.067582	1.063937	-0.341%	0.023532
443	1.079962	1.077431	-0.234%	0.018436
490	1.082345	1.081841	-0.047%	0.005412
510	1.070526	1.070582	0.005%	0.002267
560	1.055458	1.055623	0.016%	0.003365
620	1.044814	1.044863	0.005%	0.002342
665	1.045898	1.045927	0.003%	0.001748
λ	C_{MM}	$\bar{C}_{MM}$	$\beta_{C_{MM}}$	$S_{C_{MM}}$
412	1.106995	1.104797	-0.199%	0.015432
443	1.117163	1.115317	-0.165%	0.014233
490	1.094717	1.094246	-0.043%	0.005325
510	1.074479	1.074525	0.004%	0.002838
560	1.058622	1.058788	0.016%	0.004033
620	1.055496	1.055525	0.003%	0.003440
665	1.065971	1.065968	0.000%	0.003243
λ	ΔC	$\Delta \bar{C}$	$\Delta \beta_C$	ΔS_C
412	3.692%	3.840%	0.143%	0.008100
443	3.445%	3.516%	0.069%	0.004203
490	1.143%	1.147%	0.004%	0.000086
510	0.369%	0.368%	0.001%	0.000570
560	0.300%	0.300%	0.000%	0.000667
620	1.022%	1.020%	0.002%	0.001098
665	1.919%	1.916%	0.003%	0.001495

5.4.2 Analytical uncertainty propagation

The analytical uncertainty propagation method is based on the Taylor-series (TS) expansion[4] about the mean of the variable whose uncertainty is being propagated, i.e. C. Without deriving the equation, the formulation of the analytical uncertainty propagation has been given in subsection 4.1.2. Using the same input as for the MC method, Equation 4.12 is evaluated for each λ and the results are presented in Table 5.18. Recall that the uncertainty components obtained from this analytical propagation are assumed to be an approximation to the $S_{C_{MM}}$ values in Table 5.17.

What can be seen from the data is that these uncertainty components are lower than $S_{C_{MM}}$ values. Using the MM configuration with the MC propagation method, an uncertainty of approximately 1.54% was found for the first sensor band. Using the analytical propagation, the uncertainty that is computed is about 0.37 - 0.48%, depending on the expansion order. This

[4]See Appendix A for the equations of the TS expansion.

TABLE 5.18: *Analytical uncertainty components determined with the 1st-order up to 4th order Taylor series expansion.*

λ	412	443	490	510	560	620	665
uc^1	0.37463	0.26388	0.06504	0.03135	0.02986	0.01561	0.01110
uc^2	0.45954	0.31715	0.07218	0.03304	0.03163	0.01604	0.01138
uc^3	0.48181	0.32995	0.07345	0.03335	0.03203	0.01625	0.01143
uc^4	0.48808	0.33330	0.07373	0.03342	0.03209	0.01627	0.01143

difference is larger than 1% and thus an analysis is performed to identify the origin of this difference.

The analytical propagation is initially based on the first-order of the TS expansion. Arras (1998) states that the validity of Equation 4.10 and Equation 4.11 depends entirely on whether or not the first-order TS is a good approximation of the evaluated function (i.e. the RCM algorithm). In Figure 5.3 this approximation has been plotted.

FIGURE 5.3: *ρ_{sim}^{TOA} and the error ϵ between ρ_{sim}^{TOA} and the first-order Taylor-series approximation.*

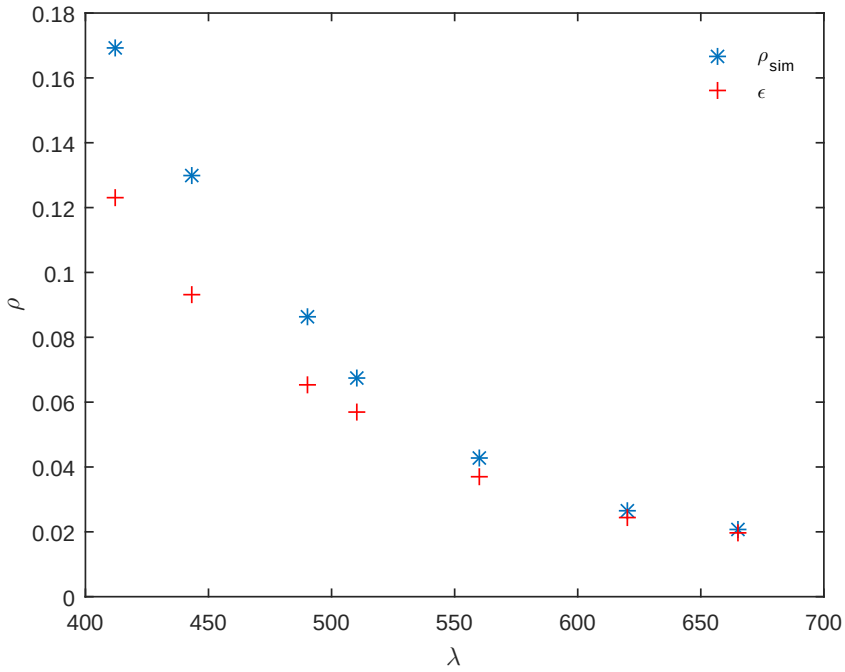

What can be noticed is that the error, which is the difference between ρ_{sim}^{TOA} and the first-order Taylor-series approximation, is very large, almost as large as the value of ρ_{sim}^{TOA} itself! This fact clearly refutes the use of the TS method as an approximation to the MC method.

According to Arras (1998), if the function is *"not too far from linear within the region that is within 1 (or 2) standard deviation of the mean"*, the TS method obtains reasonable approximations. Throughout this analysis it was noticed that C_{MM}^{MC} values behave, through visual inspection, quite linearly with the input variables. For example, in Figure 5.4 C_{MM} as a function of Chl-a perturbations (for 100 iterations) is plotted for different λ, and it can be seen that the lines approximate straight lines. This would mean that the condition is fulfilled where Equation 4.10 and Equation 4.11 are valid. Input perturbations result in an output distribution

FIGURE 5.4: C_{MM} values for different values of λ, as a function for Chl-a input variations, for 100 MC iterations.

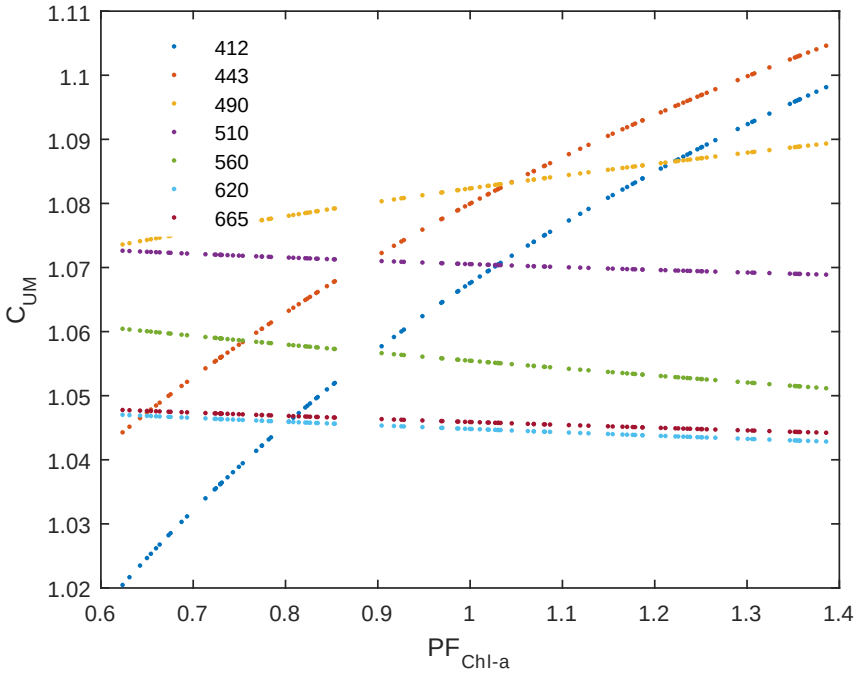

that displays a linear dependence on the input in the neighborhood close to C at a particular λ. It should be reiterated that the MM configuration is not linear as clearly shown through Equation A.1, but close to the values of C it displays a linear dependence on input variables. Despite the linearity close to C induced by input perturbations, the TS approximation of C is very poor and the applicability of the TS method is questionable.

Remembering that the input has a uniform distribution, let us assess how the output distribution can be classified. Using Equation 4.8 a test has been performed and the result suggests that the output has indeed a normal distribution. It is also possible to attempt to visually classify the output distribution through its cumulative distribution function (CDF). In Figure 5.5 the CDF of C_{MM}^{412} has been plotted, along side a CDF corresponding with a normal distribution and also a CDF of C_{MM}^{412} if it would be perfectly uniformly distributed[5]. It can be noted that the blue line neither coincides entirely with the Normal CDF or the uniform one.

What if at this point it is simply assumed to view the output as if it is linearly distributed, which would correspond with the assumption of viewing the MM configuration as if it is a linear algorithm. Then, the uncertainty propagation can be significantly simplified. In order to propagate uncertainties through a linear function, the following steps are performed;

$$y_1 = f(\mathbf{x} + \Delta\mathbf{x}) \tag{5.9}$$

$$y_2 = f(\mathbf{x} - \Delta\mathbf{x}) \tag{5.10}$$

where the uncertainty in y is then quantified as

$$\Delta y = |y_1 - y_2| \tag{5.11}$$

[5]Here the minimum number of the set of C_{MM} values is taken, and the difference with the maximum is added cumulatively and linearly with each step, to represent an actual linear function.

FIGURE 5.5: *The CDF of C_{MM}^{412} compared with a CDF associated with a uniform and normally distributed data set.*

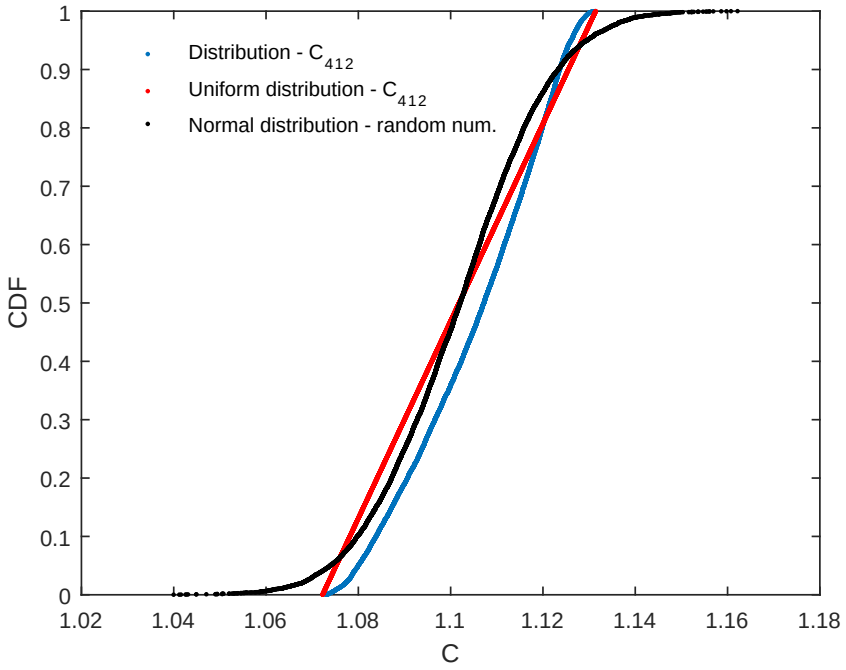

Note that $\Delta\mathbf{x}$ is the uncertainty associated with the input variables $\mathbf{x}$ (see Equation 4.14). Practically, the evaluation of y_1 and y_2 means that the RCM must be run twice and the difference between the two runs constitutes the propagated uncertainty in y due to uncertainties in $\mathbf{x}$. The result of this run has been shown in Table 5.19.

TABLE 5.19: *Propagation of total uncertainty when the MM configuration of the RCM is viewed as if it is linear and the output distribution is uniform.*

λ	C	$\bar{C}(\mathbf{x}-\Delta\mathbf{x})$	$\bar{C}(\mathbf{x}+\Delta\mathbf{x})$	$\Delta\bar{C}$	S_C		σ_C	
412	1.10698	1.08017	1.12257	0.0424	0.01224	1.106%	0.01543	1.394%
443	1.11714	1.09343	1.1317	0.03827	0.01105	0.989%	0.01423	1.274%
490	1.09468	1.09031	1.09716	0.00685	0.00198	0.181%	0.00533	0.486%
510	1.07442	1.08031	1.06915	-0.01116	0.00322	0.300%	0.00284	0.264%
590	1.05849	1.06677	1.05127	-0.0155	0.00447	0.423%	0.00403	0.381%
620	1.05536	1.06084	1.05031	-0.01053	0.00304	0.288%	0.00344	0.326%
665	1.06589	1.07234	1.05982	-0.01252	0.00361	0.339%	0.00324	0.304%

S_C is the standard deviation of the uniform output distribution and is evaluated with Equation 4.4. Here C_{min} corresponds with $(\mathbf{x}-\Delta\mathbf{x})$ and C_{max} corresponds with $(\mathbf{x}+\Delta\mathbf{x})$. Now, when comparing S_C and σ_C, the results are more than sufficiently accurate. Note that here all input parameters are perturbed. It is also possible to assess the effect of perturbing input variables individually and to combine their respective uncertainties to yield the total uncertainty value. The combined total uncertainty is given in Table 5.21. From these results it can be seen that by propagating the uncertainties individually, the combined uncertainty approximates σ_C even more accurately, but it comes with a price of 7 iterations rather than 3.

TABLE 5.20: *Propagation of individual uncertainty values when the MM configuration of the RCM is viewed as if it is linear and the output distribution is uniform.*

	λ	$\bar{C}(\mathbf{x}-\Delta\mathbf{x})$	$\bar{C}(\mathbf{x}+\Delta\mathbf{x})$	$\Delta\bar{C}$	S_C		σ_C	
Chl-a	412	1.12703	1.07616	-0.05087	0.01468	1.327%	0.01479	1.336%
	443	1.13604	1.08946	-0.04658	0.01345	1.204%	0.01358	1.216%
	490	1.10103	1.08653	-0.0145	0.00419	0.382%	0.00426	0.389%
	510	1.07281	1.07659	0.00378	0.00109	0.102%	0.00111	0.103%
	590	1.05377	1.06417	0.0104	0.00300	0.284%	0.00306	0.289%
	620	1.05303	1.05804	0.00501	0.00145	0.137%	0.00147	0.140%
	665	1.06386	1.06823	0.00437	0.00126	0.118%	0.00129	0.121%
O_3	412	1.10698	1.10698	0	0.00000	0.000%	0.00000	0.000%
	443	1.1172	1.11708	-0.00012	0.00003	0.003%	0.00003	0.003%
	490	1.09509	1.09427	-0.00082	0.00024	0.022%	0.00024	0.022%
	510	1.07528	1.07356	-0.00172	0.00050	0.046%	0.00049	0.046%
	590	1.06068	1.0563	-0.00438	0.00126	0.119%	0.00126	0.119%
	620	1.05767	1.05305	-0.00462	0.00133	0.126%	0.00133	0.126%
	665	1.06698	1.0648	-0.00218	0.00063	0.059%	0.00063	0.059%
P	412	1.10271	1.11128	0.00857	0.00247	0.223%	0.00260	0.235%
	443	1.1129	1.12141	0.00851	0.00246	0.220%	0.00258	0.231%
	490	1.09045	1.09894	0.00849	0.00245	0.224%	0.00258	0.236%
	510	1.06989	1.07898	0.00909	0.00262	0.244%	0.00276	0.257%
	590	1.05378	1.06324	0.00946	0.00273	0.258%	0.00287	0.272%
	620	1.05031	1.06045	0.01014	0.00293	0.277%	0.00308	0.292%
	665	1.06076	1.07108	0.01032	0.00298	0.279%	0.00314	0.294%

TABLE 5.21: *Combined total uncertainty value from the individual uncertainty values obtained in Table 5.20.*

λ	S_{C_T}		σ_{C_T}	
412	0.01489	1.345%	0.01502	1.357%
443	0.01367	1.224%	0.01383	1.238%
490	0.00486	0.444%	0.00498	0.455%
510	0.00288	0.269%	0.00302	0.281%
590	0.00425	0.402%	0.00438	0.414%
620	0.00353	0.334%	0.00366	0.347%
665	0.00330	0.309%	0.00345	0.324%

5.4.3 Conclusion

So far, two aspects have been reviewed of the MM configuration; 1) the approximation of C_{MM} values within 5% of C_{UM} values and 2) the approximation of $S_{C_{MM}}$ within 1% of $\sigma_{C_{UM}}$. It has been established that the MM configuration is able to obtain desirable output values if the Rayleigh scattering is estimated from the NIR band at 865 nm, and then a scaling factor is used to propagate this value to shorter λ.

With respect to uncertainty propagation, it was initially established that the MM configurations exhibits nonlinearities but on the other hand, by assuming the algorithm as linear, the propagated uncertainties yield satisfying results.

Due to nonlinearities the possible advantage of adding higher-order terms has been addressed in Table 5.18. However, the relative gain as more higher-order terms are added becomes less with each added term. By noting that $S_{C_{UM}}$ in Table 5.17 has a maximum uncertainty of 2.2%[6], it becomes clear that much more terms must be added before a desirable accuracy is obtained and this is very impractical. Additionally, it was shown that the TS approximation exhibits large deviations, which refutes the use of the TS method. On the other hand, it was also shown that the input perturbations result in a distribution of C_{MM} that is somewhat linear in the neighborhood close to C. However, the reason for this lies in noticing that $\Delta\bar{C}$ in Table 5.19 has a maximum deviation of 3.8% whereas the deviation by the TS approximation varies between $71.8 - 95.6\%$ (see Figure 5.3). This means that the approximation of C is much more accurate by treating the RCM as linear and then propagate uncertainties than by using Equation 5.11. Therefore, regardless of the fact that within 1 or 2 σ the output of the RCM is nearly linear, the TS method is rejected on the basis that it does not approximate the RCM output sufficiently[7].

[6] Note that the percentage is obtained by dividing $S_{C_{UM}}$ by $\bar{C}_{UM}$.

[7] Another aspect of using the TS expansion is that the variability of the data influences the validity of using the Taylor-series approximation. This means that the perturbed input values that were assumed may introduce a variability that is larger than the region within which the analytical uncertainty propagation method can produce accurate results, due to nonlinearities. Physically, this implies that the uncertainty associated with the input variables must be reduced before the analytical uncertainty components sufficiently approximate the MC components.

Conclusion

In this thesis the main objective was to shed light on the uncertainties that influence the accuracy with which the calibration coefficient (C) is simulated using DIMITRI's Rayleigh calibration methodology (RCM), and, to attempt to classify the individual uncertainty components that collectively form the total uncertainty.

A data and sensitivity analysis has been performed to assess how C depends on variations in the input. Before beginning with the uncertainty propagation analysis, it was argued to simplify the reflectance model to avoid complex equations required for the analytical propagation (TS) model. This would have benefits compared to the Monte Carlo (MC) method because the TS method requires 1 iteration. The MC model has still been used to validate the TS model and it proved that the uncertainty components evaluated with the TS model, could not approximate uncertainty components obtained with the MC model within the 1% benchmark, even when the fourth order TS was implemented. Increasing the order further is possible with programmes such as Maple, but given the lower yield with each added term makes me question the practicality and effectiveness of adding a large number of such terms. The reason for rejecting the TS method is because the TS approximation of ρ_{sim}^{TOA} is very poor with deviations larger than 70%. The level of approximation is a condition for the validity of using the TS method and this is not met for the RCM algorithm.

An alternative approach has been reviewed where use is made of the nearly linear relationship between C and the input variables, especially for $\lambda > 443\,nm$. It was established that if the output distribution is approximately uniform S_C^{MM} approximates S_C^{UM} to within sufficient levels. Recall that the output distribution also passed the χ^2 test, indicating that the output distribution can also be viewed as Gaussian. I have not been successful to give an explanation for the fact that it seems to have both a Gaussian and uniform distribution at the same time. Nonetheless, satisfying results in the uncertainty propagation are obtained by viewing the RCM as linear.

The second objective was to attempt a classification of the individual uncertainty components that contribute to the total uncertainty into random and systematic uncertainties. To this end, an attempt has been made in this thesis to fully map all assumptions and simplifications related to the measurement and modelling of the input variables and, also of the RCM (see flowchart on page 45). It has been argued that both types of uncertainties can be attributed to O_3, P, Chl-a and C. Throughout this thesis it became clear that a classification is not only complicated but also somewhat ambiguous, as confirmed by BIPM et al. (2008). Furthermore, it was argued to merely classify the uncertainty evaluation method to avoid ambiguity. Therefore, this thesis focused on clearly explaining the modelling and measuring procedures required to evaluate the input variables and also, the calibration coefficient. However, given the breadth of the RCM, this research was only able to outline the measurement and modelling procedure and was not able to assess uncertainty values related to those procedures, or to quantify or assign uncertainties to these processes.

Future works

For this thesis it was desired to classify the individual uncertainty components that contribute to the total uncertainty into random and systematic uncertainties. Because systematic uncertainties cannot be identified through any iterative procedure, a lot of attention was given to describing the entire measurement/modelling process of all input variables and to completely explain how the reflectance model in the RCM is designed. This explains the in-depth 'literature study' that is performed in chapter 2.

In my opinion the error associated with the Globcolour climatology monthly Chl-a maps, ε_{Chl} should be decomposed and its origin established. In this way it may be possible to classify this variable to some degree. More importantly, up to this point, the relative uncertainty and the standard deviation associated with the monthly climatology data, have been added to yield the total uncertainty. In addition, more information is required regarding the prediction model that ECMWF uses where the uncertainties associated with O_3 and P are obtained from. Similarly, by having an understanding of this prediction model and all that it entails, it may be possible to classify the uncertainties associated with these input variables.

It may be possible to analyze the effects of 'systematic' uncertainties on the RCM, even in the absence of identified sources. Up until this point, the input variables have been modified randomly but I propose to augment the procedure to include a constant deviation, to mimic a scenario where a constant systematic uncertainty is present. Even though the actual value assigned to this systematic uncertainty may be inaccurate but by performing this analysis it becomes possible to see how RCM behaves under such input perturbations. The results of this analysis can be compared with those obtained in this thesis and a distinction may indicate the sensitivity of RCM due to the presence of such a systematic uncertainty. This procedure could be performed for each input variable individually, allowing to obtain (partially) distinctive values for the propagated random and systematic uncertainty components. It should be underlined that it is not *a priori* clear whether a systematic uncertainty is constant. Only if it is concluded that for some portion of the algorithm it can be viewed constant, the proposed analysis could be meaningful.

To finalize, I believe the focus of a subsequential uncertainty analysis should not really be on how to classify uncertainties as random or systematic. The objective of such a classification is to obtain more information regarding the type of the uncertainty and to understand how sensitive it is with respect to changes in the input or the RCM algorithm. The objective can still be obtained by explaining as much as possible regarding the origin (performed in this thesis), magnitude and sensitivity of the uncertainty. Then, the uncertainties that have been defined for each step can be combined to yield a total uncertainty as an alternative to the 4% that Hagolle et al. (1999) have defined.

Appendix A

Equations for uncertainty propagation

When Equation 5.1 is substituted with all relevant expression, the total equation for ρ_{sim}^{TOA} can be expressed as follows:

$$\rho_{TOA} = e^{-\tau_{O_3} M O_3/O_{3_{ref}}} \left(\frac{f\mathcal{R}\left(0.5\, b_w + \left(0.002 + 0.01\,(0.50 - 0.25\, log_{10}\textit{Chl-a})\left(\frac{\lambda}{550}\right)^{0.5\left(log_{10}\textit{Chl-a}-0.3\right)}\right) 0.416\,\textit{Chl-a}^{0.766}\right) t_R e^{-0.5\tau_R M\,(P-P_s)/P_s}}{U\left(a_w + 0.5 b_w + \chi Chl^{echi}\right)} + \rho_R^{865}\left(\frac{\lambda^{865}}{\lambda}\right)^4 \left(1 + \frac{P-P_s}{P_s}\right) \right) \tag{A.1}$$

Here below the equations for analytical uncertainty propagation are given. Equation A.2 up to Equation A.5 are the Taylor series expansion terms from the first up to the fourth order that have been used for the values that can be found in Table 5.18. The symbol D notifies the derivative of the function and the number that is associated with it, e.g. D_{1223}, means that the first input variable must be derived once, the second input variable must be derived twice and the last input variable must be derived once. Using this method, all these D derivatives have been computed in Maple[1].

$$T_1 = f\,(0,0,0) + D_1\,(f)\,(0,0,0)\,x + D_2\,(f)\,(0,0,0)\,y + D_3\,(f)\,(0,0,0)\,z \tag{A.2}$$

$$\begin{aligned} T_2 =& 1/2\ (D_{1,1})\,(f)\,(0,0,0)\,x^2 + (D_{1,2})\,(f)\,(0,0,0)\,xy + (D_{1,3})\,(f)\,(0,0,0)\,xz + \\ & 1/2\ (D_{2,2})\,(f)\,(0,0,0)\,y^2 + (D_{2,3})\,(f)\,(0,0,0)\,yz + 1/2\ (D_{3,3})\,(f)\,(0,0,0)\,z^2 \end{aligned} \tag{A.3}$$

[1] Because the derivatives are very large expressions, I thought it best to simply give the equation with which they will be evaluated. There is no particular knowledge required with the evaluation of these derivatives since after giving the function to maple you are able to simply indicate which derivative you want it to compute. This will save valuable number of pages.

$$T_3 = 1/6\ (D_{1,1,1})(f)(0,0,0)\,x^3 + 1/2\ (D_{1,1,2})(f)(0,0,0)\,x^2y + 1/2\ (D_{1,1,3})(f)(0,0,0)\,x^2z + 1/2\ (D_{1,2,2})(f)(0,0,0)\,xy^2 + (D_{1,2,3})(f)(0,0,0)\,xyz + 1/2\ (D_{1,3,3})(f)(0,0,0)\,xz^2 + 1/6\ (D_{2,2,2})(f)(0,0,0)\,y^3 + 1/2\ (D_{2,2,3})(f)(0,0,0)\,y^2z + 1/2\ (D_{2,3,3})(f)(0,0,0)\,yz^2 + 1/6\ (D_{3,3,3})(f)(0,0,0)\,z^3 \tag{A.4}$$

$$\begin{aligned} T_4 = {} & 1/24\ (D_{1,1,1,1})(f)(0,0,0)\,x^4 + 1/6\ (D_{1,1,1,2})(f)(0,0,0)\,x^3y + 1/6\ (D_{1,1,1,3})(f)(0,0,0)\,x^3z + 1/4\ (D_{1,1,2,2})(f)(0,0,0)\,x^2y^2 + \\ & 1/2\ (D_{1,1,2,3})(f)(0,0,0)\,x^2yz + 1/4\ (D_{1,1,3,3})(f)(0,0,0)\,x^2z^2 + 1/6\ (D_{1,2,2,2})(f)(0,0,0)\,xy^3 + 1/2\ (D_{1,2,2,3})(f)(0,0,0)\,xy^2z + \\ & 1/2\ (D_{1,2,3,3})(f)(0,0,0)\,xyz^2 + 1/6\ (D_{1,3,3,3})(f)(0,0,0)\,xz^3 + 1/24\ (D_{2,2,2,2})(f)(0,0,0)\,y^4 + 1/6\ (D_{2,2,2,3})(f)(0,0,0)\,y^3z + \\ & 1/4\ (D_{2,2,3,3})(f)(0,0,0)\,y^2z^2 + 1/6\ (D_{2,3,3,3})(f)(0,0,0)\,yz^3 + 1/24\ (D_{3,3,3,3})(f)(0,0,0)\,z^4 \end{aligned} \tag{A.5}$$

Appendix B

BRDF

(Wynn, 2000; Slater, 1985) Light that is incident on the space-borne instrument has been reflected by the atmosphere or off the Earth's surface. When light is reflected by the surface, it may be reflected in various directions, with different intensities, depending on the surface characteristics and the wavelength of the light. There are two important parameters that describe the orientation of reflected light; the zenith and the azimuth angle (θ, ϕ), both for incoming and outgoing waves. In addition, light is reflected differently depending on its location on Earth's surface, given that Earth's surface is not constant and changes with geographic position (x, y).

The ratio of *reflected* radiance, L_r, with a particular orientation to *incident* radiance, L_i, with a particular orientation, given a particular geographic position and for a particular wavelength, is defined as the *Bidirectional Reflectance Distribution Function* (BRDF):

$$BRDF\left(\lambda, \theta_i, \phi_i, \theta_r, \phi_r, x, y\right) = \frac{L_r}{L_i}\left[sr^{-1}\right] \tag{B.1}$$

The quantification of the incident light can be realized by the following. Consider light traveling from the Sun and passing through the hemisphere to the Earth's surface. The hemisphere can be divided into small surface areas through which light propagates and that area is referred to as the *differential solid angle* (dw_i), which is a function of (θ_i, ϕ_i). Assuming that the differential angle is small, it can be approximated by a flat line, thus the amount of light passing through it is proportional to $L_0 \cdot dw_i$, where L_0 is the radiance of the Sun emitted on the hemisphere. The light passing through the hemisphere is 'projected' on Earth's surface, and that projection can be acquired as follows;

$$L_i = L_0 \cdot dw_i \cdot cos(\theta_i) \tag{B.2}$$

The reason why BRDF is so useful is because it can be used to predict the radiance or reflectance that is expected to be reflected by a particular surface. The incorporation of BRDF functions in atmospheric models, then, can provide estimates on L^{TOA}. Naturally, an important factor in the accuracy of the predicted L^{TOA} is the accuracy with which the BRDF is determined. There are two ways to derive the BRDF for a given surface area;

- Mathematical approximation of BRDF; using analytical/numerical models which try to fit the actual measured reflected radiances of a surface for a given incident radiance (which are the input to the analytical model).
- Direct measurement of the BRDF; through the use of a goniometer (or gonioreflectometer) the BRDF of a surface can be calculated. This instrument measures where the reflected signal originates from.

There are two important conditions implicated while using BRDF;

- There exists conservation of energy; reflected radiances can never exceed incidence radiance, i.e.; $L_r = \sum \text{BRDF} L_i \cos(\theta_i) \leq 1$ (Note that the reflected radiance can be written in terms of the incident radiance and the BRDF. In addition, in stead of a continuous space, a discrete space is assumed, hence the summation in stead of the integration sign.).
- The property of reciprocity holds; meaning that if the direction of incident and reflected light is swapped, the BRDF remains the same, i.e.; $\text{BRDF}(i, r) = \text{BRDF}(r, i)$.

BRDFs can be classified into those with *isotropic* or *anisotropic* surfaces. These classes deal with the rotational reflectance variability of the incident/reflected radiance relative to the surface normal vector. This concludes the theoretical foundation of BRDF[1].

[1] Maignan, Breon, and Lacaze, 2004 make an interesting comparison of the properties for BRDF in the VIS and NIR domain. Even though the signal to noise ratio is higher in the NIR, the RMSE in the VIS is lower, resulting in better BRDF models. It is interesting to see that sand has a higher BRDF than grass (dry more so than green) and that in the NIR the BRDF is higher than for in the VIS. Increasing the reflected zenith angle slightly increases the BRDF function value and increasing the azimuth angle reduces the BRDF value. There are two types of models; Numerical and analytical. The former uses ray tracing and Monte Carlo simulations to approximate surface characteristics/geometry. The latter model can be built in two ways; theoretical and empirical models. Theoretical models use physics to approximate the BRDF phenomenon, through the use of geometrical optics for geometrical models or radiative transfer theory for RT models or a combination of both, a hybrid model. Empirical models develop the BRDF on a vectorial base and semi empirical models combine a theoretical model with empiric parameters.

Appendix C

Processing levels input data

The radiometric data that DIMITRI operates with is the L1B data. The processing of data occurs in sequential steps starting with the L0 processing and goes up to L2. A short description of what these steps entail is included here below (*Sentinel-3 User Handbook*)[1]. It should be noted that here the processing levels and algorithms of the OLCI instrument are specifically mentioned but they are fundamentally the same type of processing required for the SLSTR instrument.

Level-0

The L0 data processing algorithm generates *L0 products* in two steps by first converting the raw data, acquired from the instrument source packet (ISP), from instrument engineering units to international system of units (SI) and secondly correcting the acquisition date and the time according to the satellite's position and its corresponding measurement location[2].

The algorithm receives the ISP and extracts therefrom the necessary raw data and performs quality checks (e.g.; information regarding nominal processing, satellite maneuvering, contingency processing and degraded processing), sorts them according to time and adds annotations (e.g.; leap second management). Communication headers that are included in the ISP are removed, as well as duplicated and invalid data[3].

An example of a L0 product output for OLCI, in its Earth Observation (EO) mode, is a package that accumulates data every $44\,ms$ for all 21 spectral bands. This information is provided in two types of processing times (Near Real-Time and Non Time Critical) with an accompanying spatial resolution of $300\,m$ (Full Resolution (FR) mode) at the Sub Satellite Point[4].

Level-1

The L1 data processing algorithm generates *L1B products* in three steps, starting with EO processing by conducting;

- data extraction and quality checks of the ISP products (e.g.; transmission, format or sequence errors)[5];

[1] https://sentinel.esa.int/documents/247904/685236/Sentinel-3_User_Handbook

[2] https://earth.esa.int/web/sentinel/technical-guides/sentinel-3-olci/level-0/processing

[3] https://sentinel.esa.int/web/sentinel/technical-guides/sentinel-3-olci/level-0/processing

[4] https://sentinel.esa.int/web/sentinel/technical-guides/sentinel-3-olci/level-0/earth-observation-mode

[5] https://sentinel.esa.int/web/sentinel/technical-guides/sentinel-3-olci/level-1/data-extraction-and-quality-checks

- *radiometric scaling*[6] which includes initialization, correction (non-linearity, dark signal and smear), absolute gain calibration and cosmetic pixel filing;
- stray light correction[7];
- geo-referencing[8] by assigning geo-coordinates for every pixel, with the Earth modeled by the World Geodetic System 1984 (WGS84) Reference Ellipsoid[9] completed by a Digital Elevation Model[10], using ocean bathymetry and land topography;
- pixel classification,[11] enabling characterization of types of terrain and includes further information regarding possible contamination by clouds and sunglint;
- spatial re-sampling,[12] whereby the FR and Reduced Resolution (RR) grids are 'filled' with the radiometric data; and finally
- product formatting where the final products (i.e.; acquisitions) of the sensor are produced.

The next step, the so-called *radiometric calibration* processing, aims to generate a set of calibration LUTs using the same input as the EO processing by following these steps;

- acquiring the geometry;
- determining the radiance at the entrance of the instrument using the acquired geometry, sun flux and diffuser bidirectional reflectance;
- computing the stray light; and
- computing the radiometric data and storing these in a LUT.

The third step determines the central wavelengths of specific rows of the detector arrays, which is a contribution to the accuracy and reliability of the instrument spectral model used in the EO and radiometric calibration[13]. All the aforementioned steps describe the data processing with which top-of-atmosphere radiances are acquired[14].

[6] https://sentinel.esa.int/web/sentinel/technical-guides/sentinel-3-olci/level-1/radiometric-scaling

[7] https://sentinel.esa.int/web/sentinel/technical-guides/sentinel-3-olci/level-1/stray-light-correction

[8] https://sentinel.esa.int/web/sentinel/technical-guides/sentinel-3-olci/level-1/georeferencing

[9] This is an Earth-centered, Earth-fixed terrestrial reference system used for the Global Positioning System (GPS). It describes the Earth's size, shape, gravity and geomagnatic fields. http://www.unoosa.org/pdf/icg/2012/template/WGS_84.pdf.

[10] This is a model of terrain elevation and the WGS84 is referenced to it, in this case.

[11] https://sentinel.esa.int/web/sentinel/technical-guides/sentinel-3-olci/level-1/pixel-classification-functions

[12] https://sentinel.esa.int/web/sentinel/technical-guides/sentinel-3-olci/level-1/spatial-re-sampling

[13] https://sentinel.esa.int/web/sentinel/technical-guides/sentinel-3-olci/level-1/radiometric-calibration-mode

[14] https://sentinel.esa.int/web/sentinel/technical-guides/sentinel-3-olci/level-1/fr-or-rr-toa-radiances

Level-2

The L2 data processing algorithm generates *L2 land and ocean products* in six steps that are applicable to both the land and ocean products. These are;

- conversion from L to ρ;
- pixel classification based on four criteria; cloud, land, water and invalid pixels;
- correction for gaseous absorption due to O_2, H_2O and O_3;
- estimation of ρ_g;
- smile correction of ρ_{obs}^{TOA} due to small scale variations in non-constant central wavelength of a band across the field of view[15]; and
- retrieval of atmospheric water vapor from cloud free pixels (i.e.; clear sky pixels).

Tie-point grid

It is worth mentioning that the product grid of the instruments is defined by the spatial resolution of the instrument. This grid coincides with the reference ellipsoid of the Earth and is evenly spaced in the across and quasi evenly in the along track direction of the satellite. There are two modes in which data can be collected, a FR mode and a RR mode. On top of this *product* grid containing radiometric data, lies another grid that is more sparse that contains auxiliary data such as meteorological data, a so-called *tie-point* grid. In the FR mode, auxiliary data must be interpolated to provide the required information for the RCM in DIMITRI. In the RR mode the product grid and tie-point grid coincide and there is no interpolation required.

For the OLCI instrument, the FR grid is defined by 16 pixels (corresponding with $300\,m$) in the across-track direction and the RR grid is 4 times sparser, i.e.; 64 pixels (corresponding with $1200\,m$) across (*Sentinel-3 User Handbook*).

[15] https://sentinel.esa.int/web/sentinel/user-guides/sentinel-3-olci/processing-levels/level-2

Bibliography

Antoine, D et al. (2011). "Reference model for third MERIS level 2 reprocessing: Ocean branch". In: *ESA, Ithaca, NY, Tech. Rep. PO-TN-MELGS-0026*.

Antoine, David and André Morel (1998). "Relative importance of multiple scattering by air molecules and aerosols in forming the atmospheric path radiance in the visible and near-infrared parts of the spectrum". In: *Applied Optics* 37.12, pp. 2245–2259.

Antoine, David and Andre Morel (1999). "A multiple scattering algorithm for atmospheric correction of remotely sensed ocean colour (MERIS instrument): principle and implementation for atmospheres carrying various aerosols including absorbing ones". In: *International Journal of Remote Sensing* 20.9, pp. 1875–1916.

Arras, Kai Oliver (1998). *An introduction to error propagation: Derivation, meaning and examples of cy= fx cx fx*. Tech. rep.

Baker, k, D Bourg, and L Brockmann (2011). "Reference model for MERIS level 2 processing. Third MERIS reprocessing: ocean branch." Technical Report PO-TN-MEL-GS-0026 (Version 5.2).

Barale, Vittorio and Peter M Schlittenhardt (2012). *Ocean colour: theory and applications in a decade of CZCS experience*. Vol. 3. Springer Science & Business Media.

Barker, K et al. (2014). "Rayleigh Scattering Methodology for Vicarious Calibration".

BIPM, IEC et al. (2008). "Evaluation of measurement data—guide for the expression of uncertainty in measurement. JCGM 100: 2008".

Bodhaine, Barry A et al. (1999). "On Rayleigh optical depth calculations". In: *Journal of Atmospheric and Oceanic Technology* 16.11, pp. 1854–1861.

Bouvet, M (2013). "Selection of optimum oceanic sites for applying the rayleigh scattering methodology to optical space sensors". ESA Unclassified document. Document type: TN.

Brewin, Robert JW et al. (2013). "The Ocean Colour Climate Change Initiative: III. A round-robin comparison on in-water bio-optical algorithms". In: *Remote Sensing of Environment*.

Bruno, Thomas J and Paris DN Svoronos (2005). *CRC handbook of fundamental spectroscopic correlation charts*. CRC Press.

Cox, Charles and Walter Munk (1954). "Measurement of the roughness of the sea surface from photographs of the sun's glitter". In: *JOSA* 44.11, pp. 838–850.

De Haan, JF, PB Bosma, and JW Hovenier (1987). "The adding method for multiple scattering calculations of polarized light". In: *Astronomy and Astrophysics* 183, pp. 371–391.

Emelyanov, EM (2001). "Biogenic components and elements in sediments of the Central Baltic and their redistribution". In: *Marine Geology* 172.1, pp. 23–41.

Fleming, David J (2006). "Effect of relative spectral response on multi-spectral measurements and NDVI from different remote sensing systems". PhD thesis.

Fougnie, Bertrand et al. (2002). "Identification and characterization of stable homogeneous oceanic zones: climatology and impact on in-flight calibration of space sensor over Rayleigh scattering". In: *Ocean Optics XVI, Santa Fe, NM*, pp. 18–22.

Fougnie, Bertrand et al. (2010). "Climatology of oceanic zones suitable for in-flight calibration of space sensors". In: *SPIE Optical Engineering+ Applications*. International Society for Optics and Photonics, 78070S–78070S.

Gordon, Howard R (1989). "Dependence of the diffuse reflectance of natural waters on the sun angle". In: *Limnol. Oceanogr* 34.8, pp. 1484–1489.

Gordon, Howard R and WR McCluney (1975). "Estimation of the depth of sunlight penetration in the sea for remote sensing". In: *Applied optics* 14.2, pp. 413–416.

Gordon, Howard R et al. (1988). "A semianalytic radiance model of ocean color". In: *Journal of Geophysical Research: Atmospheres* 93.D9, pp. 10909–10924.

Gordon, HR and AY Morel (1983). *Remote assessment of ocean color for interpretation of satellite visible imagery: A Review*.

Hagolle, Olivier et al. (1999). "Results of POLDER in-flight calibration". In: *Geoscience and Remote Sensing, IEEE Transactions on* 37.3, pp. 1550–1566.

Hansen, James E and Larry D Travis (1974). "Light scattering in planetary atmospheres". In: *Space Science Reviews* 16.4, pp. 527–610.

Hedley, J and C Mazeran (2013). "Atmospheric correction for ocean colour in a spherical shell atmosphere."

Herring, David (1999). "What are Phytoplankton". In: *NASA Earth Observatory. http://earthobservatory.nasa. gov/Features/Phytoplankton/(accessed 5 August 2012)*.

Hess, M, P Koepke, and I Schult (1998). "Optical properties of aerosols and clouds: The software package OPAC". In: *Bulletin of the American meteorological society* 79.5, pp. 831–844.

Kamp, A (2007). *Space Instrumentation Engineering - AE4880*. Delft University of Technology - University Lecture Notes.

Kirk, John TO (2011). *Light and photosynthesis in aquatic ecosystems*. Cambridge university press.

Kirk, JTO (1984). "Dependence of relationship between inherent and apparent optical properties of water on solar altitude". In: *Limnology and Oceanography* 29.2, pp. 350–356.

Koepke, P et al. (1997). "Global aerosol data set". In: *MPI Meteorologie Hamburg Rep* 243, p. 44.

Kou, Linhong, Daniel Labrie, and Petr Chylek (1993). "Refractive indices of water and ice in the 0.65-to 2.5-μm spectral range". In: *Applied optics* 32.19, pp. 3531–3540.

Lissauer, Jack J and Imke De Pater (2013). *Fundamental planetary science: physics, chemistry and habitability*. Cambridge University Press.

Loisel, Hubert and Andre Morel (1998). "Light scattering and chlorophyll concentration in case 1 waters: A reexamination". In: *Limnology and Oceanography* 43.5, pp. 847–858.

M, Douma (2008). *Colors from Vibrations - Causes of Color*. URL: http://www.webexhibits.org/causesofcolor/5B.html.

Maignan, F, F-M Breon, and R Lacaze (2004). "Bidirectional reflectance of Earth targets: Evaluation of analytical models using a large set of spaceborne measurements with emphasis on the Hot Spot". In: *Remote Sensing of Environment* 90.2, pp. 210–220.

MajorDifferences.com (2013). *Difference between Chlorophyll a and Chlorophyll b*. URL: http://www.majordifferences.com/2013/05/difference-between-chlorophyll-and.html#.VhP6Svmqqkp.

Maritorena, Stephane, David A Siegel, and Alan R Peterson (2002). "Optimization of a semianalytical ocean color model for global-scale applications". In: *Applied Optics* 41.15, pp. 2705–2714.

Maritorena, Stéphane et al. (2010). "Merged satellite ocean color data products using a bio-optical model: Characteristics, benefits and issues". In: *Remote Sensing of Environment* 114.8, pp. 1791–1804.

Mayer, B, and A Kylling (2005). "Technical note: The libRadtran software package for radiative transfer calculations-description and examples of use". In: *Atmospheric Chemistry and Physics* 5.7, pp. 1855–1877.

McLinden, Christopher Anthony (1998). "Observations of atmospheric composition from NASA ER-2 spectroradiometer measurements". In:

Morel, Anclré and Louis Prieur (1977). "Analysis of variations in ocean color". In: *Limnology and oceanography* 22.4, pp. 709–722.

Morel, Andre (1974). "Optical properties of pure water and pure sea water". In: *Optical aspects of oceanography* 1, pp. 1–24.

Morel, André (1988). "Optical modeling of the upper ocean in relation to its biogenous matter content (case I waters)". In: *Journal of Geophysical Research: Oceans (1978–2012)* 93.C9, pp. 10749–10768.

Morel, André and Bernard Gentili (1991). "Diffuse reflectance of oceanic waters: its dependence on Sun angle as influenced by the molecular scattering contribution". In: *Applied optics* 30.30, pp. 4427–4438.

Morel, Andre and Bernard Gentili (1996). "Diffuse reflectance of oceanic waters. III. Implication of bidirectionality for the remote-sensing problem". In: *Applied Optics* 35.24, pp. 4850–4862.

Morel, André and Stéphane Maritorena (2001). "Bio-optical properties of oceanic waters: A reappraisal". In: *Journal of Geophysical Research: Oceans (1978–2012)* 106.C4, pp. 7163–7180.

Pope, Robin M and Edward S Fry (1997). "Absorption spectrum (380–700 nm) of pure water. II. Integrating cavity measurements". In: *Applied optics* 36.33, pp. 8710–8723.

Prieur, Louis (1976). *Transfert radiatif dans les eaux de mer: application à la détermination de paramètres optiques caractérisant leur teneur en substances dissoutes et leur contenu en particules*. Université Pierre et Marie Curie.

Rayleigh, Lord (1899). "XXXIV. On the transmission of light through an atmosphere containing small particles in suspension, and on the origin of the blue of the sky". In: *The London, Edinburgh, and Dublin Philosophical Magazine and Journal of Science* 47.287, pp. 375–384.

S. Patel (2016). *Thesis Template - Latex*. http://www.sunilpatel.co.uk/thesis-template/.

Shettle, Eric P and Robert W Fenn (1979). *Models for the aerosols of the lower atmosphere and the effects of humidity variations on their optical properties*. Tech. rep. DTIC Document.

Slater, Philip N (1985). "Radiometric considerations in remote sensing". In: *IEEE Proceedings*. Vol. 73, pp. 997–1011.

Smith, Raymond C and Karen S Baker (1981). "Optical properties of the clearest natural waters (200–800 nm)". In: *Applied optics* 20.2, pp. 177–184.

Spada, F, MC Krol, and P Stammes (2006). "McSCIA: application of the Equivalence Theorem in a Monte Carlo radiative transfer model for spherical shell atmospheres". In: *Atmospheric Chemistry and Physics* 6.12, pp. 4823–4842.

Taylor, John R (1997). *An Introduction to Error Analysis 2nd edn (Sausalito, CA*.

Team, Sentinel-3. *Sentinel-3 User Handbook*. User Handbook. ESA/ESTEC.

VERMOTE, ERIC et al. (1992). "In-flight calibration of large field of view sensors at short wavelengths using Rayleigh scattering". In: *International Journal of Remote Sensing* 13.18, pp. 3409–3429.

whyistheskyblue (2013). *Why is the sky blue?* http://www.whyistheskyblue.co/.

Wynn, Chris (2000). "An introduction to BRDF-based lighting". In: *Nvidia Corporation*.

Young, AT (1981). "On the Rayleigh-scattering optical depth of the atmosphere". In: *Journal of Applied Meteorology* 20.3, pp. 328–330.